CHARACTERIZATION OF MICROTOPOGRAPHY AND ITS IMPACT ON CARBON DYNAMICS IN COASTAL WETLANDS USING CLOSE-RANGE REMOTE SENSING

by

Tarini Shukla

A dissertation submitted to the faculty of
The University of North Carolina at Charlotte
in partial fulfillment of the requirements
for the degree of Doctor of Philosophy in
Infrastructure and Environmental Systems

Charlotte

2023

Approved by:

_____
Dr. Craig Allan

_____
Dr. Wenwu Tang

_____
Dr. Shenen Chen

_____
Dr. Gang Chen

_____
Dr. Carl Trettin

_____
Dr. Lyndon Abrams

ABSTRACT

TARINI SHUKLA. Characterization of microtopography and its impact on carbon dynamics in coastal wetlands using close-range remote sensing. (Under the direction of DR. CRAIG ALLAN)

The spatial heterogeneity of microtopography where variation in elevation is less than a meter plays a significant role in ecological, hydrological, and biogeochemical processes. The microtopography can be categorized into microtopographic features as in the case of forested wetlands in hummocks (local high points), and hollows (local low points).To quantify and assess these microtopographic features, close-range remote sensing technologies can be used in combination with field surveys. This research provides a systematic framework for microtopographic studies using these technologies such as sUAS, aerial LiDAR, and terrestrial LiDAR. We highlight the importance of using high-resolution DEM of less than $1m^2$ spatial resolution to delineate microtopography. In a low-relief topography, especially in coastal forested wetlands where hollows and hummocks are differentiated by a few centimeters, we demonstrated a method by combining water level data and terrestrial LiDAR-based DEM to characterize microtopography over a large aerial extent utilizing coarser resolution aerial LiDAR data. This research also investigated the influence of microtopography on carbon dynamics in tidal and non-tidal coastal forested wetlands and found overestimation of ground elevation can not only misclassify the microtopographic features but also leads to an underestimation of CH_4 flux (upto 74%) and overestimation of the CO_2 flux (upto 44%). Our results show that the combination of on-site water level data and RTK GPS ground-truthed terrestrial LiDAR-based elevation data can be used to successfully adjust the base elevation and classification of microtopographic features in aerial LiDAR data. The substitution of the more variable and drier non-tidal water table regime in the process-based model resulted in a significant impact on C gas emissions with annual CH_4 emissions decreasing by an average of approximately

53% and CO_2 emissions increasing twofold over the four-year study period. The C gas flux extrapolation based on these LiDAR-based DEM over larger areas possibly at the watershed scale may open new avenues for research and can provide insight as to how wetland microtopography interacts with precipitation/ET and tidally influenced hydrologic regimes and how these may change under rising sea levels to impact GHG emissions and carbon cycling in bottomland hardwood forests.

DEDICATION

To my first teacher and mother Mrs Indumati Shukla.

ACKNOWLEDGEMENTS

I would like to thank my committee members for their guidance, especially Dr. Craig Allan for his advice, support, and mentoring throughout my research, Dr. Wenwu Tang, and Dr. Carl Trettin for providing their expert advice and financial support through research assistantships and logistic support for field data collection. Dr. Gang Chen and Dr. Shen-En Chen for sharing their expertise on close-range remote sensing. India Allan, Tianyang Chen, Navanit Sri Shanmugam, Julie Arnold, and Dick Fowler helped me with field data collection. Many thanks to Dr. Zhaohua Dai for helping me to work with the spatially explicit TFW-DNDC process-based model.

This accomplishment would not have been possible without the moral support of my family. My first and forever teacher and mother, Indumati Shukla always pushed me to shoot for the stars. She worked harder than me to make sure I succeed in life (*Agyan timirandhasya gyananjan shalakaya chakshurunmilitam yen tasmai Sri Gurve Namah*). My father, Dr. Vijay Shanker Shukla always celebrates me whatsoever. Words are not enough to express my gratitude to you Papa! (*Wah re hum log!*) I know my late grandfather *Nana Ji*, Pandit Ramanand Tripathi would have been so proud of my achievement. He always stood behind me like a rock and believed in me even when I doubted myself. My brother, Anand Shankar Shukla is my biggest cheerleader and understands me so well without saying a word. The love of my life, Anant Kumar Mishra witnessed me falling multiple times and helped me to rise again with more strength. This journey would not have been possible without his unconditional love and support. My beautiful daughter, Isha Mishra kept me grounded during challenging times and gave me the motivation and strength to go for more challenges. It is not possible to take the names of everyone who contributed to this journey but I am thankful to all of them.

I also want to acknowledge my circle of friends and colleagues who helped me transition to student life. My fabulous girlfriends Sol Park and Xiaoyu Bai for making

this journey beautiful. My friends Tianyang Chen, Vidya Chavan, Zachery Slocum, and Yu Lan helped me grow while conducting my research.

Last, but not least, I acknowledge the support of the Infrastructure and Environmental System (INES) Program for supporting me all these years in terms of assistantships, and travel grants. Thank you to Dr. Jy Wu and Dr. John Diemer of INES for their continuous support. I acknowledge the support of the graduate assistant support plan (GASP) funding for five years and I am also grateful to the Center for Applied GIS (CAGIS) for supporting me in the summers of 2019-2021. Throughout these years CAGIS supported me through travel grants to attend conferences and conduct my field works. Thank you CAGIS! I am thankful for Graduate School Summer Fellowship for the year 2022 and acknowledge the support of the Department of Geography and Earth Sciences for giving me the Geology scholar award (2019), "Mining for Gold" Winner Award (2021), and the Will and Cara Harman Scholarship (2023). I acknowledge the support of USDA US Forest Service at Santee Experimental Forest in South Carolina for providing me with logistics and technical support to conduct my field experiments. Thank you all!

TABLE OF CONTENTS

LIST OF TABLES xi

LIST OF FIGURES xii

LIST OF ABBREVIATIONS xvi

PREFACE 1

CHAPTER 1: Quantification of Microtopography in Natural Ecosystems Using Close-Range Remote Sensing 5

1.1. Introduction 5

1.1.1. Defining Microtopography 6

1.1.2. Microtopography influences ecosystem processes 7

1.1.3. Microtopography with close-range remote sensing 8

1.1.4. Research question 8

1.2. Terrain attributes for representation of microtopography 10

1.3. Spatial scale of microtopography 19

1.4. Data Acquisition 22

1.4.1. Microtopography determinations with Field-level surveys 26

1.4.2. Microtopography obtained with photogrammetry 27

1.4.3. Microtopography acquisition with aerial LiDAR 30

1.4.4. Microtopography acquisition with terrestrial LiDAR 31

1.5. Assessing microtopography 35

1.5.1. Delineation of microtopographic features 35

1.5.2. Evaluation of microtopographic features 40

1.5.3. Accuracy Assessment 43

1.6. Discussion 45

1.6.1. Microtopography with Data Fusion 47

1.6.2. Utilizing advanced techniques 49

1.6.3. Microtopography with bathymetry 50

1.6.4. Acceleration of Microtopographic Data Analytics 51

1.7. Conclusion 52

1.8. References 55

CHAPTER 2: Microtopography of low-relief coastal forested wetlands using LiDAR 74

2.1. Introduction 74

2.2. Study Area 77

2.3. Method 80

2.3.1. Terrestrial LiDAR Acquisition 83

2.3.2. Model Development 84

2.3.3. Water Level Measurements 86

2.3.4. Microtopography Classification 88

2.4. Experimental Results 90

2.4.1. Elevation Variation 90

2.4.2. Hollow Delineation 91

2.5. Discussion 96

2.6. Conclusion 97

2.7. References 98

CHAPTER 3: Quantifying the impact of LiDAR-based microtopography and tidal variations on greenhouse gas dynamics in freshwater coastal forested wetlands 103

3.1. Introduction 103

3.2. Materials and Methods 109

3.2.1. Study Site 109

3.2.2. Microtopography Classification 110

3.2.3. Greenhouse Gas Modeling 113

3.3. Results 116

3.3.1. Microtopography Classification 116

3.3.2. TFW-DNDC GHG Emission Model Results 117

3.3.3. Influence of the tidally influenced water table regime 123

3.4. Conclusion and Discussion 127

3.5. References 129

CHAPTER 4: Overall Conclusion 133

LIST OF TABLES

TABLE 1.1: List of microtopography-based studies with associated terrain attributes and DEM resolution. (RMSE: root mean square error; unit: meters) 11

TABLE 1.2: Advantages and limitations of close-range remote sensing methods for microtopography data acquisition 24

TABLE 1.3: Landscape metrics (mean values) calculated for a tidal bottomland forest (Figure 1.8) (114). 43

TABLE 2.1: Microtopography study area considered by different studies using terrestrial LiDAR. 81

TABLE 3.1: Microtopographic classification 112

TABLE 3.2: Average monthly water levels (cm) in relation to the ground surface for hollows, fringe, and hummocks using terrestrial LiDAR-based 0.25 m resolution. 115

TABLE 3.3: Terrestrial and aerial LiDAR data based annual CH_4 (kg C/ha/yr) emissions in Huger Creek study site. 118

TABLE 3.4: Terrestrial and aerial LiDAR data based annual soil CO_2 (Mg C/ha/yr) emissions in Huger Creek study site. 118

TABLE 3.5: Modeled microtopography-weighted C gas emissions for the study site using TFW-DNDC utilizing the terrestrial and aerial LiDAR-based DEMs. 121

TABLE 3.6: Carbon emissions with respect to previous studies of Dai et al (26), Renaud (30) and Allan unpublished data 122

TABLE 3.7: Tidal and non-tidal based annual CH_4 emissions (kg C/ha/yr) in Huger Creek study site. 124

TABLE 3.8: Tidal and non-tidal based annual CO_2 emissions (Mg C/ha/yr) in Huger Creek study site. 124

TABLE 3.9: Modeled microtopographically weighted carbon emissions under a tidal and non-tidal water table regieme for the study area. 126

LIST OF FIGURES

FIGURE 1.1: Framework to answer microtopography-based questions using close range remote sensing techniques 9

FIGURE 1.2: Stochastic depression analysis showing the probability of depressions in the Huger Creek forested wetland study site in Santee Experimental Forest, S.C. using A) ALS data and B) TLS data. 21

FIGURE 1.3: Suggested framework for the generation of microtopographic models using close-range remote sensing techniques. 23

FIGURE 1.4: The high-resolution DTM of a low-relief coastal forest (2-cm spatial resolution) orthomosaic developed from SfM photogrammetry method using 570 images. 29

FIGURE 1.5: Side- and top-view of the TLS point cloud data obtained in a bottomland forested wetland site. [A] Raw TLS data is filtered and exported, [B] Point cloud clipped to 1 m, [C] 1 cm Surface Model. 34

FIGURE 1.6: Depression delineation using priority-flood algorithm and level-set method based on aerial LiDAR-derived DEM of $1m^2$ resolution in a low relief tidal wetland at Huger Creek area in Santee Experimental Forest South Carolina. The depressions are delineated based on the size of a minimum $1m^2$ area and depth of 0.50 m. 38

FIGURE 1.7: The graph shows the morphometric data of the delineated hollows shown in Figure 1.6 - volume in cubic meters and depth in meters for each of the delineated hollows. 41

FIGURE 1.8: Landscape categorization based on elevation threshold: microtopographic features - hollows ($<$ 0.65 m), hollows fringe (0.65 to 0.80 m) and hummocks ($>$ 0.80 m) based on terrestrial LiDAR DEM with grid cell size 0.25 m X 0.25m in a low relief tidal wetland at Huger Creek area in Santee Experimental Forest, South Carolina. 43

FIGURE 2.1: Tidal freshwater forested low-relief wetland located at Huger Creek in Santee Experimental Forest, SC USA. 78

FIGURE 2.2: Shaded relief of the study site located at tidal freshwater Huger Creek 79

FIGURE 2.3: Scan configuration of forested wetlands using terrestrial LiDAR. The distance between each scan is 10m to ensure overlapping scans. 84

FIGURE 2.4: Ground points extracted from terrestrial LiDAR data using cloth simulation filters in CloudCompare. 85

FIGURE 2.5: Georeferencing the resultant point cloud using 0.61 m X 0.61 m GCP (visible in inset) measured using RTK GPS 85

FIGURE 2.6: Maximum water level fluctuations from 2019-2022 in hollow, fringe, and hummock. The line at 0.00 indicates the ground surface level based on terrestrial LiDAR data while the dashed line is the ground surface level based on aerial LiDAR data. 87

FIGURE 2.7: A) Terrestrial LiDAR-based DEM with a 0.25 m resolution B) Aerial LiDAR-based DEM with a 1 m resolution. 90

FIGURE 2.8: Depression delineation A) terrestrial LiDAR data of 0.25 m resolution and B) aerial LiDAR data of 1m resolution. The depressions are shown above the shaded relief. 92

FIGURE 2.9: Depression delineation using the priority flood algorithm based on aerial LiDAR data with a minimum sink size of 1 m^2 and minimum sink depth of 0.5 m. The blue line shows the boundary of the study site. 93

FIGURE 2.10: Elevation distribution of LiDAR-based DEM where the vertical line shows the threshold elevation. A) Elevation distribution of terrestrial LiDAR-based DEM of 0.25 m resolution. Vertical lines show the threshold of 0.68 m, which is selected based on the maximum mean water level. B) Elevation distribution of aerial LiDAR-based DEM of 1.00 m resolution. Vertical lines show the threshold of 0.87 m, the 29th percentile of the elevation values. 94

FIGURE 2.11: Microtopography classification based on the mean daily water level and elevation threshold. A) Microtopography classification in terrestrial LiDAR-based DEM with hollow, fringe, and hummock covering an area of 28.7%, 21.7%, and 49.6% respectively. B) Microtopography classification in aerial LiDAR-based DEM with hollow, fringe, and hummock covering an area of 30.6%, 18.4%, and 51.0% respectively. 94

FIGURE 2.12: Microtopography delineation over a larger scale using an elevation threshold. Hollows are delineated at the 29th percentile of the elevation distribution covering 39% of the total area. 95

FIGURE 3.1: Structure of the TFW-DNDC Model 107

FIGURE 3.2: Study site at Francis Marion National Forest located at Huger Creek in Santee Experimental Forest SC USA. 109

FIGURE 3.3: Terrestrial LiDAR-based ground point cloud of the study site. The ground points are extracted using the cloth simulation filter. A total of 108 overlapping scans were taken for the study site. The scan position is visible as black circles. 111

FIGURE 3.4: Elevation density distribution of terrestrial LiDAR-based DEM of 0.25m resolution and aerial LiDAR-based DEM of 1m resolution. A) Vertical lines show the threshold of 0.68 m which is selected based on the maximum mean water level. B) The vertical line shows the threshold of 0.87 m which is the 29th percentile of the elevation values. 112

FIGURE 3.5: Hydrological regime of A) hollows, B) fringe, and C) hummocks at the tidal Huger Creek site from 2019 to 2022 using terrestrial LiDAR-based elevation. The figure shows the daily maximum water levels at each microtopographic feature. Here 0.00 represents the ground surface; positive values indicate the water level above the ground elevation while negative values denote the water level below the ground surface. The dashed line shows the ground surface in respect of aerial LiDAR data. 114

FIGURE 3.6: A) Shaded relief of terrestrial LiDAR-based DEM, B) shaded relief of aerial LiDAR-based DEM, C) terrestrial LiDAR-based DEM of 0.25 m resolution, and D) aerial LiDAR-based DEM of 1.00 m resolution. 116

FIGURE 3.7: Microtopography classification based on the mean daily water level. A) Terrestrial LiDAR-based classification of microtopography B) Aerial LiDAR-based classification of microtopography in hollows, fringe, and hummocks 117

FIGURE 3.8: A) Simulated CH_4 emissions using terrestrial LiDAR-based data. B) Simulated CH_4 emissions using aerial LiDAR-based data 118

FIGURE 3.9: A) Simulated CO_2 emissions using terrestrial LiDAR-based data. B) Simulated CO_2 emissions using aerial LiDAR-based data 119

FIGURE 3.10: Precipitation/evapotranspiration and tidally driven water table regimes for the 2019-2022 study period. The solid black line indicates the ground level. A) Non-tidal water level at the hollows, B) Tidal water level at the hollows, C) Non-tidal water level at the fringe, D) Tidal water level at the fringe, E) Non-tidal water level at the hummocks, F) Tidal water level at the hummocks. 123

FIGURE 3.11: A) Simulated CH_4 emissions for tidal water levels. B) Simulated CH_4 emissions non-tidal water levels. 125

FIGURE 3.12: A) Simulated CO_2 emissions for tidal water levels. B) Simulated CO_2 emissions non-tidal water levels. 125

LIST OF ABBREVIATIONS

C Carbon

CH_4 Methane

CO_2 Carbon dioxide

CSF Cloth Simulation Filter

CZMIL Coastal Zone Mapping Imaging LiDAR

DEM Digital Elevation Model

DFDB Dual Frequency Dual Baseline

DSM Digital Surface Model

DTM Digital Terrain Model

FAA Federal Aviation Administration

GCP Ground Control Points

GHG Greenhouse Gas

GNSS Global Navigation Satellite System

GSD Ground Sample Distance

HPC High Performance Computing

InSAR Interferometry Synthetic Aperture Radar

LiDAR Light Detection and Ranging

N Nitrogen

NDVI Normalized Difference Vegetation Index

NIR Near Infrared

PPK Post Processed Kinematic

RGB Red Green Blue

RTK GPS Real Time Kinematics Global Positioning Systems

SAR Synthetic Aperture Radar

SfM Structure from Motion

SIFT Scale Invariant Feature Transform

sUAS small Unmanned Aerial Systems

TIN Triangulated Irregular Network

TLS Terrestrial Laser Scanners

VLOS Visual Line of Sight

PREFACE

Microtopography plays an important role in various ecological, hydrologic, and biogeochemical processes. However, quantifying the characteristics of microtopography represents a data-intensive challenge. Over the last decade, high-resolution or close-range remote sensing data and techniques have become a powerful tool for microtopography quantifying. The availability of wide-area aerial LiDAR data and cost-effective small unmanned aerial systems (sUAS) or drone-based technologies and terrestrial LiDAR has helped further research in examining microtopography in various environments. Traditional field surveys were mainly limited to transects or small plots, using limited sets of observations. Still, with the decrease in the cost of close-range remote sensing technologies and increased computing performance, the microtopography, even in forested environments, can be assessed.

The first chapter provides a systematic framework for microtopographic studies using close-range remote sensing technologies. This is achieved by reviewing the application of close-range remote sensing to capture microtopography and develop microtopographic models in natural ecosystems. Specifically, to achieve the main objectives, we address the following questions: 1) What terrain attributes represent microtopography in natural ecosystems? 2) What spatial resolution of terrain attributes is needed to represent the microtopography? 3) What methodologies have been adopted to collect data at selected resolutions? and 4) How to assess microtopography? Current research, challenges, and applicability of close-range remote sensing techniques in different terrains are analyzed with an eye to enhancing the use of these new technologies.

We highlight the importance of using a high-resolution DEM (less than $1m^2$ spa-

tial resolution) to delineate microtopography. Such high-resolution DEM can be generated using close-range remote sensing techniques. We also illustrate the need to move beyond elevation and include terrain attributes such as slope, aspect, terrain wetness index, ruggedness, flow accumulation, and flow path and assess their role in influencing biogeochemical processes such as greenhouse gas emissions and species distribution and biodiversity. To assess microtopography in terms of physical characteristics, several methods can be adopted such as threshold-based classification or mechanistically-based delineation, and machine learning-based delineation of microtopography. The microtopographic features can be analyzed based on physical characteristics such as area, volume, depth, and perimeter or by using landscape metrics to compare the classified microtopographic features. When used with field experiments/data, remote sensing techniques provide new avenues for researchers to understand ecological functions such as biodiversity and species distribution, hydrological processes, greenhouse gas emissions, and the environmental factors that influence those parameters. This article provides a comprehensive and detailed review of microtopography data acquisition and quantification for natural ecosystem studies.

In the second chapter, we assessed the high-resolution fine-scale microtopographic features of a coastal forested wetland (CFW) with terrestrial LiDAR and aerial LiDAR to test a method appropriate to quantify microtopography in low-relief forested wetlands. Our method uses a combination of water level data and elevation thresholding to delineate hollows in terrestrial and aerial LiDAR data. Close-range remote sensing technologies such as LiDAR can be used for microtopography in forested regions. However, aerial and terrestrial LiDAR technologies have yet to be used to analyze or compare microtopographic studies in CFW systems. Therefore, the objective of this chapter was to 1) characterize and assess the microtopography of low-relief tidal forested wetlands and 2) identify optimal elevation thresholds for widely available aerial LiDAR data to characterize microtopography. Our results suggest that a com-

bination of water level and percentile elevation thresholding can correctly characterize the microtopography in this area of low-relief topography.

The microtopography of wetlands has been found to significantly influence the spatial distribution of methane (CH_4) emissions, with significantly higher emissions occurring from hollows than hummocks. However, there is very scarce information available on the influence of microtopography on carbon gas (CO_2, CH_4) fluxes in tidal freshwater forested wetlands (TFFW). The third chapter investigated the influence of wetland microtopography derived from both terrestrial (0.25 m spatial resolution) and coarser scale aerial LiDAR (1m spatial resolution) coverages on C gas emissions in a TFFW wetland in coastal South Carolina. We used the spatially distributed processed-based TFW-DNDC model to simulate CH_4 and CO_2 fluxes from three microtopographic features-hollows, fringe, and hummocks, representing 29%, 21%, and 50% of the 4250 m^2 study area for the calendar years 2019-2022. Each microtopographic feature had a unique combination of vegetation, hydrology, and soil characteristics. Tidally influenced ground and surface water levels were recorded on site. The daily maximum and minimum water levels were used as a model input along with site-specific vegetation and soil parameters.

We also explored the influence of the tidally driven hydrologic regime on C gas emissions by substituting the water levels from a nearby non-tidal forested wetland with similar soils and vegetation cover over the same time period in the model. As could be expected wetland hollows were hotspots for CH_4 emissions (218.4 to 284.3 kgC/ha/yr) as compared to hummocks (-10.1 to -9.7 kgC/ha/yr). Carbon dioxide emissions were significantly greater for hummocks (3.4 to 4.0 MgC/ha/yr) than hollows (0.1 to 0.6 MgC/ha/yr). Our results show that the coarser aerial LiDAR-based DEM underestimated CH4 emissions by 10% to 74% and overestimated CO_2 emissions flux by 26% to 44% for the study years. By substituting the precipitation/evapotranspiration-driven water table regime instead of the tidal water level regime into TFW-DNDC

we found that CO_2 flux increased by two to three times while CH_4 was reduced by 78% over the study period. Our results quantify the TFW-DNDC model sensitivity to the spatial resolution of the base DEM and indicate the importance of using a high-resolution DEM (less than $1m^2$ spatial resolution) to delineate microtopography in low-relief coastal wetland environments. This research also highlights the interaction between wetland microtopography and tidal hydrology in determining C gas emissions in freshwater coastal wetlands. The microtopography characterization method described here may be used and built upon for future use.

CHAPTER 1: Quantification of Microtopography in Natural Ecosystems Using Close-Range Remote Sensing

1.1 Introduction

[1]The spatial heterogeneity of microtopography where elevation differences are often less than a meter plays a significant role in various ecological, hydrologic, and biogeochemical processes including carbon (C) and nitrogen (N) dynamics (2; 3; 4; 5). The biogeochemical importance of microtopography lies in its impact on carbon sequestration (6; 7), greenhouse gas (GHG) emissions, and other biogeochemical processes (8; 9; 10), and hydrological function (11; 12). These processes or functions are influenced by surface microtopography (13; 14; 15; 16). For example, in an estuarine environment, the tidal riparian zone is affected by the interaction of microtopography and daily tidal fluctuations, resulting in a complex pattern of soil gas emissions (17). The biogeochemical activity, soil characteristics, and spatial interactions between vegetation, nutrients, hydrology, microbial communities, and soil organic carbon are all in part influenced by microtopographic features (18; 19; 20). Microtopography also explains vegetation composition in wetlands and forests due in part to vertical variations in soil water which impacts the availability of nutrients such as phosphate and ammonium (13). In addition, the spatial and temporal distributions of hydrologic connectivity in forested wetland landscapes can be substantially influenced by microtopography. The microtopography can be categorized into microtopographic features as in the case of forested wetlands which are characterized by hummocks or mounds (local high points), hollows or depressions (local low points), and lawns (intermediate elevation points). Hummocks are higher elevation patches in a wetland consisting

[1]This chapter is published as an article authored by Shukla et al.(1).

of dense mats of soil, moss, and roots from herbaceous vegetation while hollows are found at a comparatively lower elevation where the soil is saturated.

1.1.1 Defining Microtopography

To understand the ecological, hydrologic, and biogeochemical processes from a micro to macro (or local to global) scale, it is important to quantify microtopography and identify the scale of a high-resolution model which can appropriately represent the spatial heterogeneity of the study site. It is vital to first define microtopography and microtopographic features in order to quantify and classify spatially heterogeneous topography in natural ecosystems. Hunneke and Sharitz (21) defined microtopography as spatial heterogeneity at the scale of plants and individual seeds. Along a similar vein, Titus (22), Bledsoe and Shear (23) stated microtopography is the elevation or topographic heterogeneity of substrates at the scale of individual plants where the elevation ranges from 1 cm to 1 m. Subsequently, Moser et al. (24) described microtopography as the combination of relief and roughness where relief is vertical variation and roughness represents topographical variability. Diamond et al. (25) and Stovall et al. (26) referred to microtopography as the vertical variation in the ground surface occurring at centimeters to meter scales. Although elevation is the most common terrain attribute which is associated with microtopography, other terrain attributes such as slope, aspect, flow path, ruggedness index, wetness index, and curvature can also be significant in microtopography-based studies (27).

Microtopography which influences ecological, hydrological, and/or biogeochemical processes can be defined and classified irrespective of the spatial extent of a study area, which means it can range from individual soil cores, and field plots to the scale of a watershed. Also, microtopographic features are not limited to hummocks and hollows (common microtopographic features in wetlands) or pits and mounds (microtopographic features in forests). Instead, microtopographic features are the landscape characteristics that are classified and/or delineated based on their spatial and tem-

poral extent to estimate the impact of microtopography on ecosystem functions. In summary, microtopography represents the variation in terrain elevation observed at a small (e.g., submeter) spatial scale over a study site, and the microtopographic features are the landscape characteristics that can be delineated based on terrain attributes over a given spatial and temporal extent.

1.1.2 Microtopography influences ecosystem processes

Small-scale variations in microtopographic features when studied over a large extent may exert significant impacts on hydrologic, biogeochemical, and biologic processes. In natural ecosystems, microtopography influences the hydroperiodicity in hollows and hummocks and soil moisture which in turn impacts element cycling. The surface flow path is greatly influenced by the spatial arrangement of hollows and hummocks where hummocks can reduce the water storage by up to 30% (28). Assuming homogeneous surface without considering microtopography can alter the surface water flow in modeling exercise and in turn the associated results. Based on soil saturation the hollows become the local control point for methane emissions and over a large extent can be considered as ecosystem control points. In contrast, hummocks are often the control points for high primary productivity. Multiple studies (29; 5; 30) have shown that there is spatial variation in wetlands CO_2 and CH_4 emissions; hollows with reduced redox state (low oxygen availability) are the source of greater methane emissions. Due to extended exposure to open air and availability of nutrients, hummocks are the source of carbon dioxide emissions.

Microtopography also influences exogenous processes such as landslides, erosion, and nutrient transportation. Exogenous processes are the result of the interaction of geological, hydrological, meteorological factors with microtopography. Processes such as soil erosion and runoff have a significant role in sediment/nutrient transportation. Studies (27; 31; 32) conducted at a fine spatial scale showed the importance of microtopography in studying exogenous processes.

1.1.3 Microtopography with close-range remote sensing

Recent studies have reported the use of close-range remote sensing technologies to map fine-scale microtopography by using dense and highly accurate elevation data over reasonably large areas (33; 34; 35; 36; 26). However, this is a recent development, and researchers examining fine-scale processes or distributions have traditionally relied on labor-intensive manual field surveys. It is our view that a more complete understanding of the state-of-the-art remote sensing techniques and their limitations will facilitate their incorporation into future experimental designs and modeling applications examining such topics as carbon cycling, hydrologic processes, and vegetation pattern and composition at fine spatial scales. The aim of this article is to provide a systematic framework for microtopographic studies using close-range remote sensing technologies. This is achieved by reviewing the application of close-range remote sensing to capture microtopography and develop microtopographic models in natural ecosystems. Close-range remote sensing techniques such as small Unmanned Aerial Systems (sUAS) and LiDAR technologies have enabled researchers to employ these technologies repeatedly during different seasons to identify the impact of microtopography on the seasonal distribution of vegetation, hydrological connectivity, and GHG fluxes. Small but critical features that are often missed in satellite imagery can be revealed by aerial and terrestrial LiDAR or in sUAS-based photogrammetry in low or sparsely vegetated wetlands.

1.1.4 Research question

The main objective of this article is to provide a systematic framework for microtopographic studies using close-range remote sensing technologies. In the past, the characterization of microtopography over large areas was difficult due to limitations in the ability to collect the density of data necessary to represent microtopographic features. The most common methods of measuring microtopography involve exten-

sive manual surveys or transect-based manual surveys and utilizing remote sensing techniques such as aerial surveys and LiDAR-based techniques. To characterize microtopography in a study site, a researcher should focus on answering the following questions: 1) What terrain attributes can represent the microtopography? 2) What spatial resolution of terrain attributes are needed to represent the microtopography? 3) What methodology to adopt to collect data at the selected resolution? and 4) How to quantify microtopography? Thus, in this article, to achieve the main objective, we focus our discussion on addressing these four aforementioned questions, to assist researchers in optimizing the use of these new technologies in support of microtopography-based ecosystem studies (see Figure 1.1)

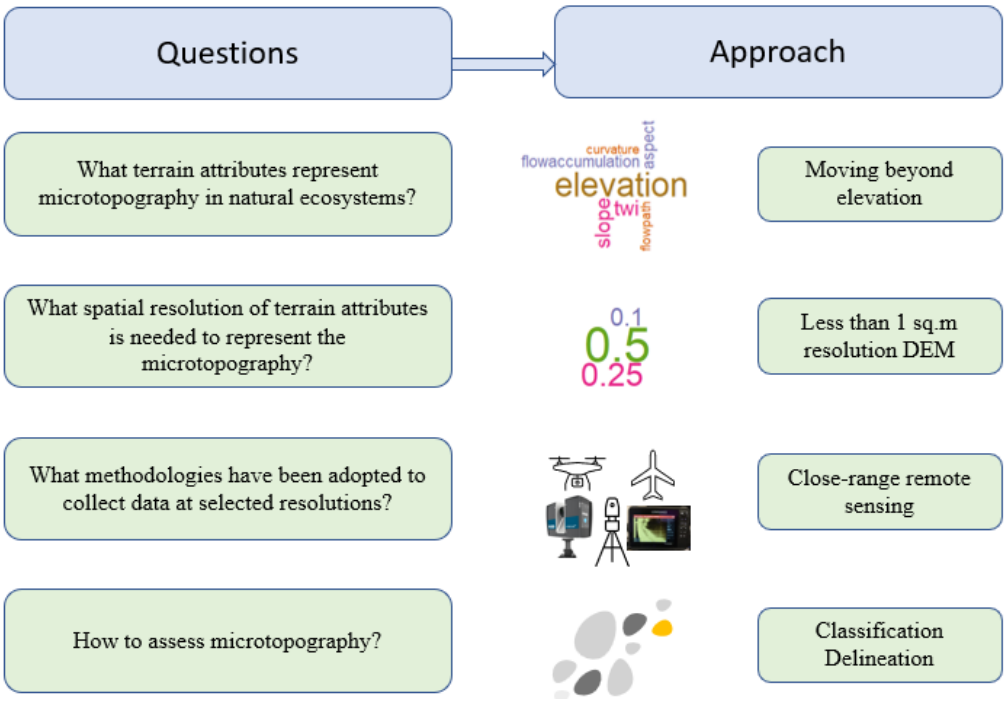

Figure 1.1: Framework to answer microtopography-based questions using close range remote sensing techniques

1.2 Terrain attributes for representation of microtopography

Microtopography studies often require the use of quantitative measures to represent microtopographic characteristics. These quantitative measures mainly include terrain attributes (quantified as a continuous spatial variable based on elevation) and landscape metrics (quantified as a categorical spatial variable). Terrain attributes are the quantities that express the position and orientation of ground points (37). Terrain attributes can be determined using DEMs, which is based on elevation as a continuous spatial variable. Terrain attributes include, but are not limited to, elevation, aspect, slope, flow path. flow accumulation, and topographic index. Elevation is the primary attribute for assessing microtopography but other terrain attributes such as roughness, slope, and terrain indices can also be critical in characterizing microtopography. Table 1.1 summarizes a variety of ecosystem features impacted by microtopography with corresponding terrain attributes and spatial resolution.

Table 1.1: List of microtopography-based studies with associated terrain attributes and DEM resolution. (RMSE: root mean square error; unit: meters)

Study Area	Study Objective	Terrain Attribute	Resolution (m)	DEM RMSE	Characteristics of study area	References
Pennsylvania, USA	Microtopography	Elevation Slope Curvature	1.00	0.18 to 0.37	Ridge	(38)
South Carolina, USA	Microtopography	Elevation	0.25	0.04	Tidal forested wetland	This Study
Minnesota, USA	Microtopography	Elevation Slope Roughness TRI	0.01 to 2.00	0.024 to 0.058	Forested wetland	(26)
Minnesota, USA	Microtopography	Elevation Slope Concavity	0.10	0.04	Forest	(3)
Banff National Park, Canada	Microtopography	Elevation	0.05 to 2.00	0.052 to 0.082	Open shrub wetland	(39)

Queensland, Australia	Mosquito management	Elevation	1.00	0.042	Mangrove	(40)
Tabernas Desert, Spain	Erosion	Elevation Roughness	0.01	-	Hillslope system	(41)
South Carolina,USA	Erosion	Elevation Flow accumulation Curvature TWI Slope	1.00	0.04	Hillslope system	(42)
East Siberia, Russia	Carbon storage	Elevation	2.00	-	Tundra	(43)
Northern England	Roughness	Elevation Slope Ruggedness	0.005	-	Blanket Paetland	(44)
Alaska, USA	GHG Emissions	Elevation	2.00	-	Tundra	(45)
Minnesota, USA	GHG Emissions	Elevation	0.10	0.04	Forest	(34)

Alaska, USA	Hydrological Processes	Elevation	0.25	-	Tundra	(46)
Alaska, USA	Hydrological Processes	Elevation	0.20	0.05	Tundra	(47)
Alaska, USA	Hydrological Processes	Elevation	0.50	0.023	Tundra	(48)
Colorado, USA	Species richness	Elevation Slope Curvature TPI TWI Flow-accumulation	0.50	0.15	Hillslope system	(49)
Minnesota, USA	Species composition	Elevation	0.01	0.024	Forested wetland	(33)
Mexico	Species composition	Elevation	0.10	<1.00	Tidal wetland	(50)

Hungary	Vegetation Pattern	Elevation Slope Curvature TPI TWI Aspect	0.25	-	Grassland	(51)
Sumatra, Indonesia	Vegetation Pattern	Elevation	1.00	-	Forest	(52)
North Wales, UK	Vegetation Pattern	Elevation TPI TWI Ruggedness	0.20	<0.75	Blanket peatland	(53)

Colorado, USA	Vegetation Pattern	Elevation Slope Curvature TPI TWI Aspect	0.50	-	Hillslope system	(54)
Singapore	Vegetation Pattern	Elevation	1.00	-	Mangrove	(55)
Alaska, USA	NEE	Elevation	0.50	<0.068	Tundra	(56)
Hawai'i, USA	Species recovery	Elevation	1.00	-	Arid	(57)
New York, USA	Soil Characteristics	Elevation Slope Aspect TWI Flow-accumulation	5.00	<6.00	Mountainous landscape	(37)

Texas, USA	Soil Characteristics	Elevation TWI Flow-accumulation	10.00	<10.00	Plains	(58)
Alptal, Switzerland	Soil Characteristics	Elevation Slope Curvature Ruggedness TWI Aspect Flow-accumulation Flowpath	0.50	0.12 to 0.45	Mountainous landscape	(27)
Suhua Highway, Taiwan	Landslide	Elevation Slope	1.00	0.04	Coastal Highway	(59)

Isfahan, Iran	Landslide	Elevation Slope Curvature Aspect	-	-	Hillslope system	(60)
Roznow Lake,Poland	Landslide	Elevation Slope Aspect flow-direction	1.00	-	Lakeside	(61)

- data not available

Another terrain attribute which has not been widely explored for microtopographic studies of natural landscapes is surface or soil texture (62). Surface texture can be related to the microforms such as hummocks or hollows and can be related to surface roughness. The roughness values are calculated based on a prescribed window size and estimated for each window to capture the complexity of the terrain. In addition, once microtopography is classified and delineated as hummocks or hollows, these hummocks or hollows are landscape patches that are categorical spatial variables in nature. Thus, landscape metrics (63), originating from the domain of landscape ecology, can be used to analyze the spatial characteristics of these microtopography patches with respect to their composition and configuration. More details on landscape metrics will be discussed in Section 1.5.

1.3 Spatial scale of microtopography

The scale of the microtopographic features of interest is an important consideration. Small variations in elevation matter when it comes to representing microtopography and its associated physical, biogeochemical, and ecological processes. In other words, the study of microtopography often operates at small spatial scales, which often requires high spatial resolutions to capture microtopographic features at smaller spatial scales. Spatial resolution refers to the actual ground size that a pixel represents or the smallest possible geospatial feature that can be detected. Spatial resolution needs to be fine enough in order to capture the information of a geospatial feature. Specifically, spatial resolution needs to be finer than the scale that a geospatial phenomenon operates on i.e., operational scale; see (64; 65). Therefore, a high resolution DEM is needed to detect small elevation changes (often at submeter level) in the microtopography, which operates at a small spatial scale. This fine spatial resolution need is reflected in the literature (see Table 1.1; microtopographic features ranging from 0.005 meter to 10 meter; most of them are under 1m).

It is necessary to identify what spatial resolution of terrain attributes can adequately represent the microtopography at a specific location. With LiDAR data it is possible to obtain sub-centimeter resolution DEM data, but an important question is what is the right resolution to capture the landscape microtopography? In Baltensweiler et al. (66) modeling of soil pH distribution, the most appropriate spatial resolution was found to be 0.5m with a cross-validated R^2 value of 0.62. While Stovall et al. (26) found that a DEM resolution of 0.01 to 1m was necessary to represent hummocks in a Black Ash wetland system and determined the most accurate classification of 78.7% was obtained with a 0.25m resolution of DEM. The most appropriate resolution depends on what ecological functions one is trying to model and the complexity of the study site itself. Table 1.1 shows the spatial resolution of DEM used by different studies. High spatial resolution studies can result in microtopographic fea-

ture classifications with improved accuracy, which can differ from those obtained from coarser spatial resolutions in the same region. This may lead to different results in the estimation of parameters for models of GHG emissions, hydrologic connectivity, and biogeochemical processes that are associated with microtopography in natural ecosystems. However, the use of high spatial resolutions often leads to data and computational challenges.

The horizontal resolution and vertical accuracy of elevation are significant aspects of microtopographic studies. The DEM resolution can be selected based on the study site and the purpose of the study. Several researchers have examined the effects of DEM resolution in their study sites. Habtezion et al. (67) in their study of the North American prairie Pothole region found that a coarser resolution DEM (>10m) tended to overestimate ponded areas and underestimate runoff discharge. DEM resolution becomes even more important for low-relief topography where microtopographic features are differentiated by a few centimeters. We used a stochastic depression analysis tool in Whitebox geospatial analysis tools (GAT) (68) to derive depressions from a 1 m^2 resolution airborne LiDAR scan (ALS) and a 0.25 m^2 resolution terrestrial LiDAR scan (TLS) DEM for a tidal bottomland forest area as shown in Figure 1.2. The high-resolution TLS successfully identified the series of hollows at the south end of the study site. In addition, it also provides information on connected and standalone depressions. This means a TLS-based collection methodology more accurately represents this low-relief forested terrain as compared to a coarser 1 m^2 resolution ALS DEM which underestimated the aerial extent of depressions/hollows in this environment.

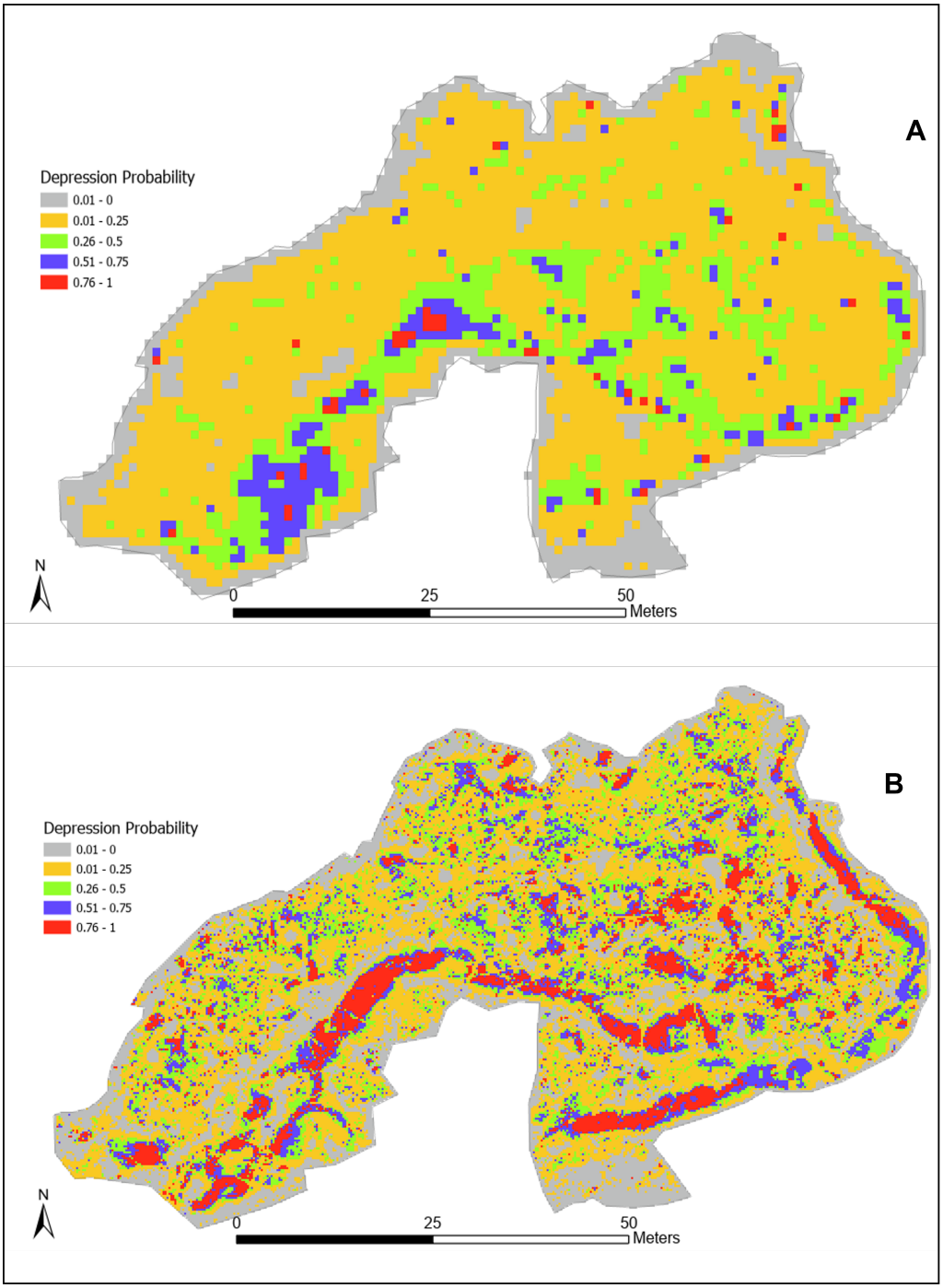

Figure 1.2: Stochastic depression analysis showing the probability of depressions in the Huger Creek forested wetland study site in Santee Experimental Forest, S.C. using A) ALS data and B) TLS data.

1.4 Data Acquisition

Here we focus on providing guidance as to what remote sensing methodology to adopt to collect data at selected spatial resolutions. Microtopography at high resolutions can only be measured in two ways. First by extensive manual surveys and second by utilizing high-resolution remote sensing techniques. A manual survey requires labor, access to surveying equipment, and the transportation of that equipment to the study site. Most of these studies have used the transects method using surveying equipment such as total stations, digital levels, or more recently real-time kinematics global positioning systems (RTK GPS) and they have relied on the categorical analysis of predefined hummocks and hollows (16; 69; 70; 71). Transects are often limited in their site representativeness and are relatively ineffective to represent the entire region of interest. In contrast, remote sensing techniques can be used for the purpose of microtopographic mapping of larger areas at a high resolution and affordable cost. For instance, readily available aerial LiDAR data where point spacing is 1m or less can provide useful information on microtopography at the field-to-watershed scale.

To decide on the acquisition methodology, researchers need to know the extent of the study area and how much time and relevant resources are available. Based on time and available resources, microtopography can be measured manually or by using remote sensing techniques. Here we will focus on close-range remote sensing techniques. These methods include aerial surveys with Structure from Motion (SfM) photogrammetry, ALS, and TLS. Combining these measurements with elevations and coordinates obtained with RTK GPS or a total station survey can help georeference the data and validate the remotely collected data. Topographic data collected using more recently developed remote sensing techniques greatly expands the topographic information available as compared to field-level survey approaches employed in earlier studies. Currently, researchers develop a microtopographic model based on the objective of the study and the availability of terrain data. There is no consistent con-

ceptual or analytical framework that provides a guideline to develop microtopographic mapping. Here we attempt to develop a basic framework involved in estimating the microtopographic features (Figure 1.3). Here we discuss each of these methods in terms of the limitations and advantages of these methods (Table 1.2).

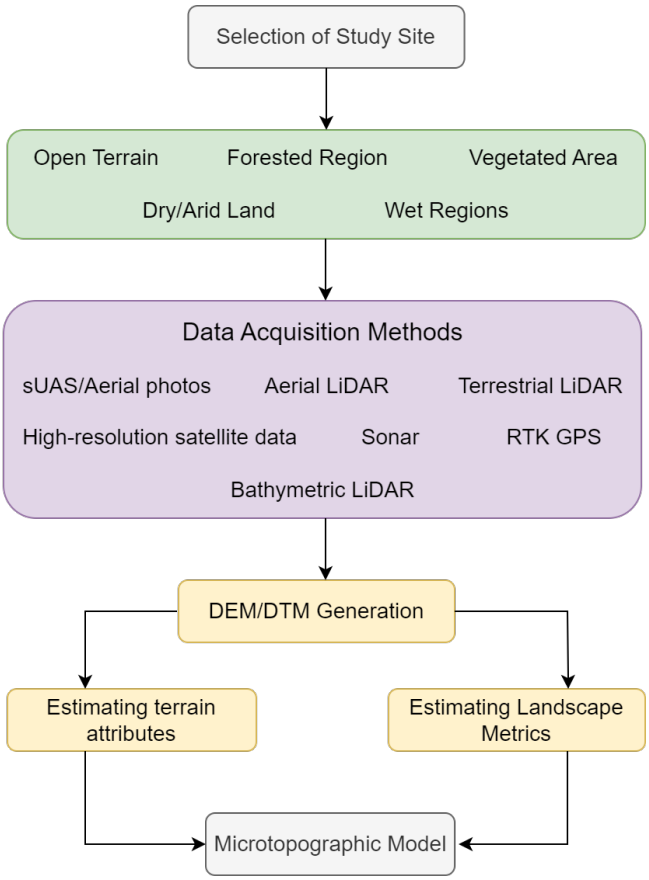

Figure 1.3: Suggested framework for the generation of microtopographic models using close-range remote sensing techniques.

The figure shows the data collection method in different terrains namely open terrain such as sparsely vegetated terrain, forested areas such as mangroves, vegetated and dry region such as shrubs and grasslands, vegetated and wet regions such as marsh, open and wet terrain such as lakes and shorelines.

Table 1.2: Advantages and limitations of close-range remote sensing methods for microtopography data acquisition

Data Acquisition Method	Advantages	Limitations (m)	References
Field Surveys	Data can be used for validation and georeferencing of remote surveys Minimal post-processing of data	Carrying stores and equipment to site Labor intensive Transect-based studies (5m to 1,550m transects) Inherent assumption that relatively few observations can represent the whole study site (20-125 observation points)	(26)
Aerial photos/sUAS	Cover larger areas compared to field surveys Thermal sensor can detect soil moisture RGB images provide more realistic visualization with high spatial resolution of 0.01 m to 0.05 m. Multiple flight plans can be executed	May require prior permission before flying Post-processing requires technical expertise Flying altitude and velocity impacts data quality Flight duration is restricted by battery life (20 min to 45 min for sUAS)	(72; 73)

Aerial Lidar	Higher density of laser pulses leads to a higher spatial resolution of $1m^2$ or less	Overestimation of ground points in dense forest Horizontal error is in the order of 1/1,000 of aircraft flight altitude Post-processing requires technical expertise	(74; 75)
Terrestrial LiDAR	Can be moved easily to target locations high point cloud density of 20-40 million points per scan Small scan footprint	Low oblique angle data acquisition Post-processing requires technical expertise	(26; 73)

1.4.1 Microtopography determinations with Field-level surveys

Field-based microtopographic studies generally rely on the use of transects or the study site is divided into multiple sections. The location of transects or subsections is selected based on either topography or species type. Several surveying instruments are used for such surveys including a clinometer, hypsometer, height sticks, level string, dumpy level, and laser range finder. These studies were more common when remote sensing technologies such as LiDAR and UAS were not available. Here we provide a few examples to show how such surveys were carried out as well as the time and effort that went into those microtopographic studies.

Almquist et al. (76) used a clinometer and two rods at 20 m distances along a transect of 480-1540 m to assess the treefall gaps based on microtopography in a bottomland hardwood forest collecting 24-77 observations. In order to study the diversity of trees and forest structure in tropical freshwater swamp forests in relation to microtopography and water level, Koponen et al. (77) used a hypsometer at 15 m intervals of 10m x 50 m sample plots and height sticks to measure the water surface level. The authors considered nine plots to design a transect 530 m long taking 36 observations on the transect. Courtwright and Findlay (13) studied tidal swamps on the Hudson River and found significant porewater and vegetative differences between hummocks and hollows although the elevation difference was only 19 cm relative to a 1m tidal range. The authors used a level string that is 20cm long along a transect to obtain relative elevation. The study considered five transects each 5m long with 25 observations on each transect. In another study (78) wooden poles at a certain distance along the transect were used to obtain the elevation and study forest structure in a coastal Mexico lagoon.

All these studies attempted to collect elevation data which now can be easily collected with LiDAR and UAS-based technologies. Along with close-range remote sensing technologies total stations and RTK GPS is the most widely used field surveying

instruments that are being used to validate and georeference remotely collected data.

1.4.2 Microtopography obtained with photogrammetry

sUAS-based SfM photogrammetry is best suited for wetlands where trees are absent or have a low tree or shrub cover (3). The sUAS-based SfM photogrammetry has been used in various wetland terrains including mapping moss in Antarctica (79), mapping alpine peatlands in Canada (39), quantifying roughness for different peat surfaces (44), and evaluating the impact of seismic lines on peatland CH_4 emissions (80). A sUAS represents a low-cost sensor platform that can cover a wide area as compared to a tripod or even vehicle-mounted terrestrial LiDAR with several flight missions possible within a few hours. Although the RGB-based camera on sUAS can provide high-resolution images, in the case of forested wetlands the data under a forest canopy cannot be captured and therefore currently their use is not suitable for microtopographic studies in forested environments. The sUAS with thermal sensors can effectively detect variable soil moisture conditions that can be associated with hummocks/hollows complexes (81). Near-infrared (NIR) and multispectral cameras can be used to characterize vegetation and analyze the impact of microtopography on vegetation types. The flying altitude and velocity of sUAS also play an important role in the quality of data collection.

1.4.2.1 SfM based Photogrammetry

In the SfM photogrammetric technique, a mosaic of images is created and then georeferenced using ground control points (GCPs). This technique creates a very high-resolution 3D point cloud which is utilized to create a high-resolution DEM or digital surface model (DSM) as per user requirements. The process has been explained by a number of researchers (e.g. (39; 82). In general, the SfM analysis provides 3D information from stereoscopic 2D images. The process involves the identification of common points called key points. The commonly used algorithm for feature detection

is Scale Invariant Feature Transform (SIFT, (83)), which identifies key points in the image. The key points are the unique characteristics of an image. These key points are invariant of image rotation and scale and remain robust with changes in illumination and the addition of noise. An initial sparse point cloud is created following bundle block adjustment and a high-resolution 3D model is created based on stereoscopic images. The GCPs assist in improving the accuracy of the bundle adjustment and a 3D georeferenced model is generated from a 3D point cloud.

In the case of open topography, RGB camera-based sUAS can assess microtopography effectively. The sUAS-derived SfM photogrammetry can create DSM of sub-centimeter resolution with marked GCPs. Figure 1.4 shows the DSM of a relatively open topography of a low-relief clear-cut forest in coastal South Carolina USA. The orthomosaic was developed from the SfM technique using 570 images with 80% side and front overlaps, covering an area of 180,000 sq. meters (using Pix4DMapper software). A total of 6 GCPs were established using RTK GPS and the images were georeferenced using these GCPs, with a mean root mean square error (rmse)of 0.006m.

1.4.2.2 Topographic models for microtopography

To quantify microtopography with aerial photos, is inherently related to the purpose of a study. Harris and Baird (53) used a fine-scale topographic model to evaluate the drivers affecting vegetation patterning. Their study found mean elevation as the most influential variable in blanket peatland vegetation patterns due to the high correlation of vegetation with topography and soil moisture. Martinez Prentice et al. (62) used a high-resolution microtopographic model of six wetlands in Estonia using sUAS to analyze the distribution of plant communities. The elevation difference of these wetlands varied between 0 to 3 m and both object- and pattern-based classifications were performed to analyze the distribution of grasslands.

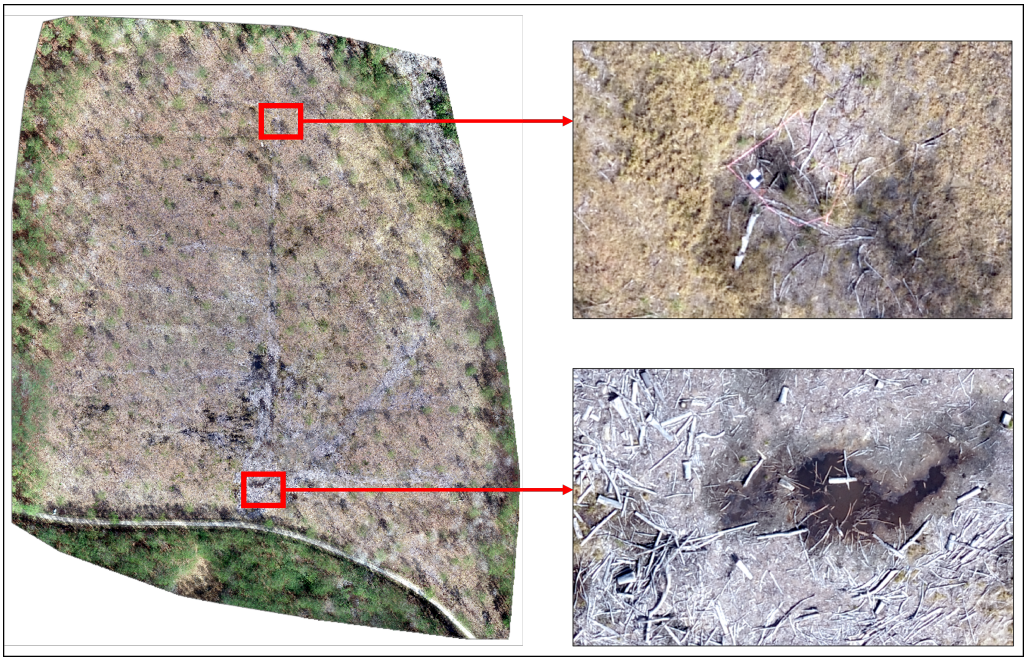

Figure 1.4: The high-resolution DTM of a low-relief coastal forest (2-cm spatial resolution) orthomosaic developed from SfM photogrammetry method using 570 images.

Although sUAS-based photogrammetry techniques can provide high-resolution low-cost 3D topography this technique has limited applications in dense forest environments. In the case of forested wetlands, sUAS are generally used for the estimation of aboveground biomass density, leaf area index, and vegetation pattern for delineating a wetland boundary. A few studies have also utilized sUAS-based photogrammetry for the estimation of GHG fluxes. Becker et al. (84) utilized a dirigible type sUAS for image acquisition and concluded that the spatial resolution of a DEM impacts the detection of biogeochemical hot spots with respect to CH_4 and CO_2. Lehmann et al. (85) used infrared images captured by sUAS to estimate uncertainty in CH_4 flux in a South Patagonian peatland related to site microtopography. They considered the distribution of vegetation and microform to estimate the CH_4 emission at an ecosystem scale.

sUAS-based measurements of microtopography can cover reasonably large spatial extent of up to few square kilometers, which is a major advantage over conventional

transect-based analysis or manual field survey approaches. It provides an affordable solution to quantify the microtopography at a fine spatial scale. The ease of operation enables researchers to collect data multiple times and conduct the analysis of spatial variations over time. These operations must be carefully planned based on considerations of available battery life. Adverse weather conditions need to be avoided to ensure the safety of equipment, and the quality of data, as well as to comply with legal requirements. Quantifying wetland microtopography in forested wetlands and upland forests is more problematic due to the presence of an often dense upperstory and understory. In these environments, large errors in measurement can lead to unreliable or low accuracy of the resultant microtopography mapping. In contrast, open topography such as bogs, boreal wetlands and peatlands with sparse vegetation can be assessed for microtopography at high spatial resolutions. Currently, the two most popular photogrammetric software used by researchers are Agisoft Metashape and Pix4DMapper (86). Both are proprietary software, which can provide cloud-based processing and utilize a large collection of images without the need for system upgrades on the user side. Alternative options include open-source software such as OpenDroneMap, openMVG, VisualSFM, and MicMac, which are also available but require technical expertise from users.

1.4.3 Microtopography acquisition with aerial LiDAR

Aerial LiDAR has been used to assess forest canopy structure, underlying terrain, and sub-canopy vegetative structure. In aerial LiDAR scanning, the laser pulses are emitted from the airborne platform and then the backscattered signal from the sensor to the earth's surface is measured, which provides the range estimation between the LiDAR device and the earth's surface. This process is explained in detail in (87). Chasmer et al. (88) called the frequency distribution of the returns from LiDAR scans a "digital fingerprint" for the natural environment with an assumption that different parts of wetlands and forests have different vegetation structures and morphological

characteristics. Aerial LiDAR housed on fixed-wing and sUAS platforms has also been used extensively for estimating surface roughness (38) and mapping forested wetlands (89). The LiDAR-based sUAS are comparatively more costly than camera-based sUAS but they can effectively capture spatial variations or hummocks/hollows complexes in a vegetated study site depending on the bare ground point density.

The high pulse density and/or small scan footprint associated with LiDAR systems are an asset in mapping microtopography. The LiDAR echoes are processed to create a digital terrain model (DTM). In aerial LiDAR, the higher the pulse propagation frequency the greater the pulse return density per unit area is. A higher density of pulses leads to a higher spatial resolution that can be utilized to construct a high-resolution DTM. To create the representation of a site's microtopography researchers use ground returns with pulse density of 2 pts/square meter or higher and create a DEM of 1m or higher spatial resolution (grid cell size of 1m or less). The cells that do not contain a return are filled with interpolation techniques such as the nearest neighbor, spline methods, inverse distance weighted (IDW), Kriging, and triangulated irregular network (TIN) interpolations (90).

1.4.4 Microtopography acquisition with terrestrial LiDAR

In measuring landscape microtopography the scanner in a terrestrial LiDAR system is mounted on a tripod and can be moved easily to target locations. The laser intensity is inversely proportional to the square of the distance/range while in ALS atmospheric condition also plays a significant role. In contrast to ALS, the incidence angle impacts the data quality of TLS. The number of scans varies as per study site, terrain, and research question. Terrestrial LiDAR data collection is prone to shadowing effects and occlusion. This can be overcome by scanning the study plot from multiple angles and overlapping scan locations. The registration of multiple scans requires tie points, which are common points used to align and register the point cloud. Artificial objects such as cylindrical reflectors, spherical targets, or checkered markers are placed in each

location to be scanned and later used as the tie-points. More scans are required for fine-scale terrain modeling to capture the impact of microtopography on, for example, ecosystem functions. As the point density decreases linearly with distance, the LiDAR data acquisition should therefore be planned beforehand to consider the terrain.

The terrestrial scanners generate higher point cloud density compared to the aerial LiDAR. However, aerial LiDAR covers a larger area as it acquires data at near nadir view angles while TLS due to its low oblique angle of transmitting signals, covers substantially smaller areas. The dense vegetation in forests creates occlusion and shadowing as the signals get interrupted or reflected on their way to the scanner. As the scan distance increases the probability of returned signal originating from a non-ground object also increases. This leads to an overestimation of ground elevation. This is the reason why there is an overestimation of ground elevation exhibited by both terrestrial and aerial LiDAR in dense forests. For complex study sites, TLS data is more favorable as compared to aerial LiDAR (66). The main limitation of TLS-based surveys is that they are required to move to multiple scan positions to ensure overlapping scans and to cover the study site. The point cloud density is higher around the scanner and inversely proportional to the square of the distance to the TLS position (91). Also, due to the shadowing effect in forests, it becomes more difficult to separate ground surface and non-ground points (92). To overcome this limitation a larger number of scans with different viewsheds is required.

The use of terrestrial LiDAR for capturing bare ground in a vegetated region is more challenging. Data acquisition should be planned during the dormant season when leaves are off, and grass and bushes are largely senesced. This will help in addressing the issue of occlusion due to a dense understory. The original point cloud data collected from LiDAR cover both ground and surface returns such as trees and shrubs, which requires cleaning through the use of stray/noise filters to remove spurious or noisy scan points and above-surface scan points. This process may require a number

of iterations until most statistical outliers are removed. The resultant filtered point cloud can then be used for further analysis or delineation of hummocks and hollows. The registered and filtered point cloud collected from terrestrial LiDAR is used for subsequent analysis. To analyze the microtopography the point clouds associated with the ground are retained, which means that point clouds above the ground are required to be removed.

The ground points can be extracted from the dense point cloud generated by terrestrial LiDAR to create a high-resolution DEM. Several researchers (93; 28; 33; 3; 94; 26) used open source CloudCompare software to extract ground points. The extraction of ground points requires a point cloud library (PCL, see (95)) to remove noise and outlier points. PCL assumes a normal distribution of points where outliers can be removed based on a defined threshold value of standard deviation. The resultant point cloud can be rasterized for subsequent analysis. Another useful tool that can be used to extract ground points is the use of a cloth simulation filter (CSF) (96). This method imagines a piece of cloth over the point cloud which is turned upside down. In other words, an imaginary cloth is assumed over an inverted surface which can classify points as ground and non-ground points as shown in Figure 1.5.

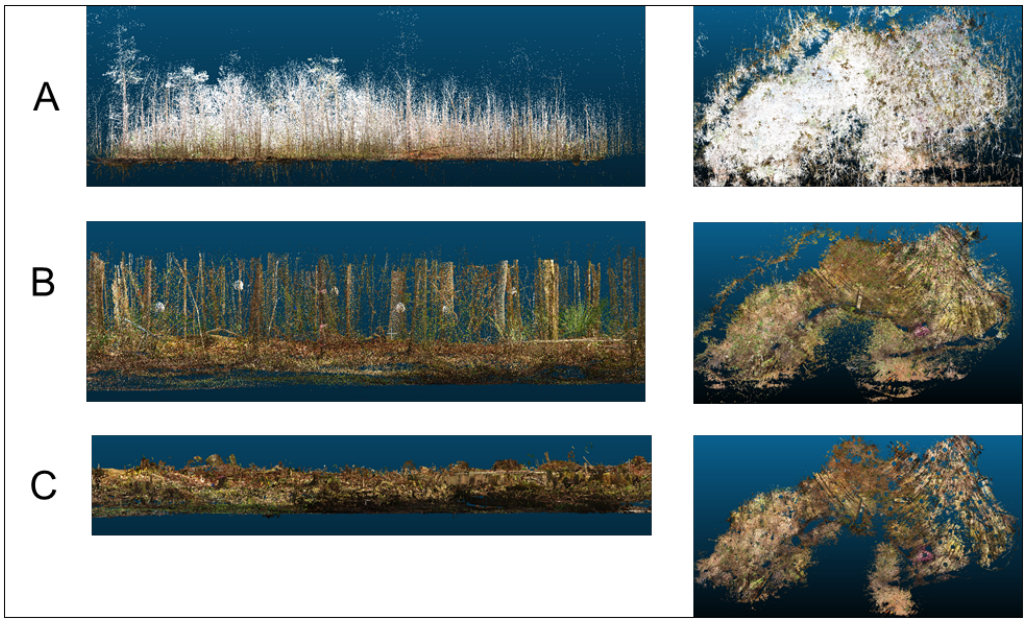

Figure 1.5: Side- and top-view of the TLS point cloud data obtained in a bottomland forested wetland site. [A] Raw TLS data is filtered and exported, [B] Point cloud clipped to 1 m, [C] 1 cm Surface Model.

Here are a few guidelines for conducting the terrestrial LiDAR based survey: 1) conducting reconnaissance of the study site before carrying out actual surveying. This will assist in deciding the minimum distance between the scan positions. The location of GCPs can also be decided during this time. 2) Establishing GCPs or fixed spherical targets and measuring them with RTK GPS. 3) The scan positions can be decided based on transects where each transect is separated by 10m and each scan position is separated by 10m in a forested landscape. In other landscapes this distance can be increased depending on occlusions. In a dense forest with understory and shrubs the scanner can be set at a high point cloud density of 20-40 million points. This will assist in automated registration of multiple overlapping scans. 4) The control targets or tie points should be evenly distributed with a minimum 3-5 spherical targets that should be common in adjacent scans. In forested ecosystems, the spherical targets should be increased from 5 to 8. 5) Before processing the point cloud, the minimum distance between the points can be kept at 1 cm to reduce the point density.

1.5 Assessing microtopography

Assessment of microtopography typically consists of two steps: delineation of microtopographic features and evaluation of delineated microtopographic features. In this section, we focus our discussion on these two steps for the assessment of microtopography.

1.5.1 Delineation of microtopographic features

Delineation of microtopographic features mainly includes three approaches: 1) threshold-based classification, 2) mechanistically based delineation, and 3) machine learning-based delineation.

1.5.1.1 Threshold-based classification of microtopographic features

The common way of extracting microtopographic information from field-based surveys is to use transects or plots in the study site and classify microtopographic features, such as hummocks and hollows based on the field experience or sparse measurements. With the availability of close-range remote sensing techniques, the microtopographic features can be delineated over a larger area based on different criteria. Graham et al. (3) identified three ways to characterize microtopography: 1) based on drivers associated with an ecological function such as using water table depth, 2) elevation distribution of the study plot and classifying hummocks and hollows based on a threshold, and 3) classifying microtopography based on an index, specifically hollow index, which is calculated using elevation, concavity, and slope.

Multiple researchers used elevation-based thresholds to categorize hollows and hummocks from a DEM generated from sUAS or LiDAR data. The threshold elevation is determined based on field characteristics, expert knowledge, and assumptions. Kalacska et al. (97) conducted a study on three tidal marshes in Canada using sUAS and aerial LiDAR and found the accuracy is comparable to RTK GPS with R^2 values of 0.99 and 0.83 for the two methods, respectively. In their study, the authors used

expert knowledge to define the height range of 5-31 cm above the median elevation to define hummocks while >5cm below the median height range were characterized as hollows. Knight et al. (40) analyzed microtopography along a transect in mangroves in Queensland, Australia. They used a 1m resolution DEM from LiDAR data and generated contours at an interval of 0.05m. Then the microtopography was analyzed along a transect where hummocks were identified as positive deviations that are >0.05 m above the local mean elevation and hollows as deviations that are <0.05 m below the mean elevation.

The categorization of microtopographic features is also guided by the aim of the study. Kelly et al. (81) differentiated hummocks and hollows based on vegetation types. The sites with Sphagnum sp. were classified as hollows while vascular vegetation sites were classified as hummocks. Griffin et al. (98) generated a LiDAR-derived DEM to analyze the impact of microtopography on mosquito habitats. Brubaker et al. (38) used a pit-filled DEM and then subtracted it from the original LiDAR-derived DEM to identify pit and mound topography within an oak/hickory forest in Pennsylvania, USA.

In addition to elevation, the slope has also been used extensively to categorize microtopographic features. Cici et al. (52) generated a DTM derived from LiDAR-based data and calculated slope within a 10m radius of each tree and then analyzed the impact of slope on tree height in a tropical forest in Sumatra. Moreover, the information on the intensity of LiDAR can also be used for the validation of classified features. Korpela et al. (99) used aerial LiDAR in a boreal bog in southern Finland to assess microtopography and analyzed the intensity of echoes that was the highest in hummocks and lowest in water and hollows. That study employed a grid size of 20 cm x 20 cm, hummock index, and depression index to measure the elevation with respect to local water level along with the echo intensity to classify microtopography. A coefficient of +1 or -1 was assigned based on high or low elevation respectively.

A value of +8 indicated a perfect peak while -8 corresponded to a depression. The LiDAR returns were analyzed concurrently with aerial imagery in red, green, and blue bands to classify different microtopographic features. The LiDAR/photogrammetry combination worked well in this open bog region as there was nominal occlusion by trees. This also shows that shortwave infrared LiDAR intensity varied with the microtopographic features and is a good indicator/predictor of the spatial distribution of hummocks, hollows, and lawns.

Anderson et al. (100) collected their data over a transect of 10 m at seven different sites, and the vegetation pattern was analyzed in the quadrats of 20 cm x 20 cm. RTK GPS was used to measure elevation along the transect at 50 cm intervals. The hollows and hummocks were identified based on the water level readings and RTK GPS readings. Baltensweiler et al. (66) derived a high-resolution DEM at different scales of 0.2 m, 0.5 m, 1.2 m, and 4 m to create a soil pH model and found 0.5 m model predicted the soil pH most accurately but (66) used a priori information to stratify the study area in depression and ridges. Zhang et al. (101) classified their coastal forested study region into tall and short vegetation and bare ground object.

1.5.1.2 Mechanistically-based delineation of microtopographic features

The DEM developed from close-range remote sensing techniques is highly precise and captures microtopographic features which are natural depressions and not spurious depressions. While delineating depressions such natural depressions should be preserved over artifacts. To identify natural depressions (102) proposed to combine the âDEM-unchangedâ (original DEM) strategy and the "DEM-revising" (filled DEM) strategy based on the study area and data characteristics. Recently (103) proposed a level-set method that is based on graph theory to delineate nested depressions and a priority-flood algorithm (104) to identify depressions. In a low-relief complex topography, these methods can be useful as they can delineate nested depressions (Figure 1.6) and can provide insights into the hydrological connectivity of depressions.

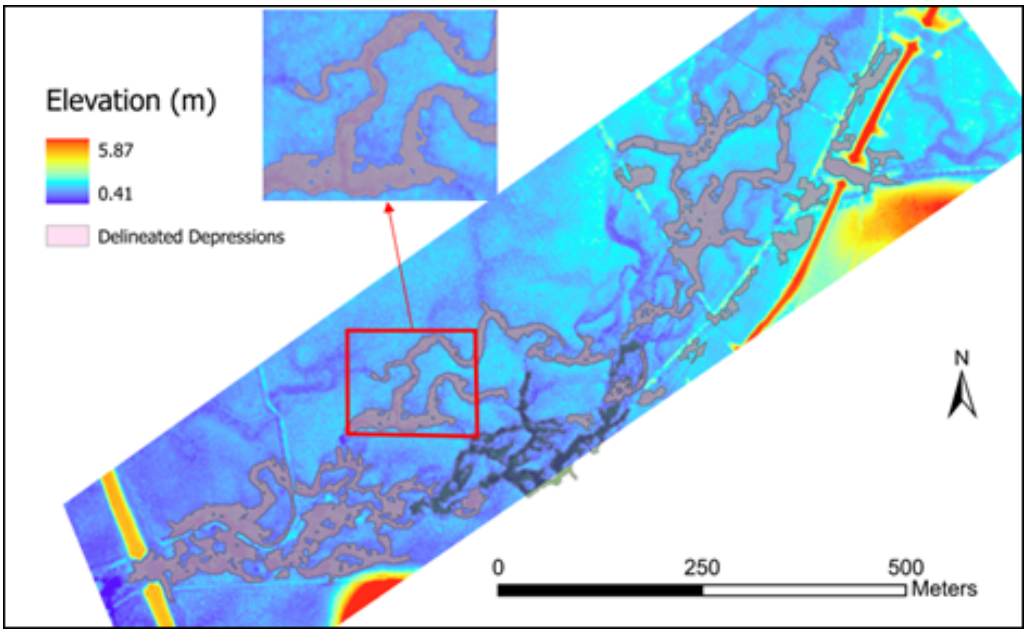

Figure 1.6: Depression delineation using priority-flood algorithm and level-set method based on aerial LiDAR-derived DEM of $1m^2$ resolution in a low relief tidal wetland at Huger Creek area in Santee Experimental Forest South Carolina. The depressions are delineated based on the size of a minimum $1m^2$ area and depth of 0.50 m.

Another method of delineating hollows is utilizing a localized contour tree approach to identify individual hollows. Wu and Lane (105; 106) delineated wetland hollows in the prairie pothole region of North America and represented them in the form of contours. A power function curve fitted to the storage area-to-volume relationship provided an area-to-volume model for estimating the storage volume of wetland hollows in the watershed. Most of the hollows in the DEM represented areas that are either inundated continuously or inundated seasonally. Chu et al. (107) proposed a puddle-to-puddle (P2P) modeling framework based on identifying depressions and their hierarchical relationships. The method simulates the surface inundation by filling, spilling, and merging the cells based on the hydrological connectivity and finally delineating the depressions. To delineate hummocks (26) used the watershed delineation approach by inverting the elevation values in the surface model and finding edges of the watershed that actually represents hummock edges. The delineated microtopographic features then can be analyzed for physical characteristics such as area,

volume, and depth/height.

1.5.1.3 Machine learning-based delineation of microtopographic features

A variety of machine learning algorithms have been used for image processing operations. This machine-learning approach can be applied to the extraction of microtopographic features. Moreover, microtopographic field data can be combined with high-resolution DEM/DSM derived from high-resolution satellite images or LiDAR data. Falco et al. (49) investigated the covariability of field soil resistivity tomography data, vegetation data, and terrain attributes utilizing aerial LiDAR-based DEM and Worldview-2 high-resolution RGB satellite images. Abolt et al. (108) and Witharana et al. (109) used convolution neural networks (CNN), a deep learning approach (110), to extract polygons of various sizes and geometry from aerial LiDAR-based DEM of tundra landscape. Another popular machine learning technique is Random Forest which is based on the use of decision trees and ensemble learning for classification and regression. Multiple researchers have shown that microtopography impacts the location and extent of the plant communities (51; 62). Huang et al. (111) mapped thermokarst landforms automatically using the DeepLab algorithm (based on CNN) using high-resolution SfM-based images over a large area of 6 km ^{2}. In addition to delineation, machine learning approaches are also used for sensitivity analysis of microtopography classification (26).

Threshold based classification only considers the elevation based threshold which makes it easy to categorize microtopographic features. The threshold can be determined based on field observation and elevation data/ DEM which can provide more accurate delineation of the features. Mechanistically-based algorithms not only considers elevation but also slope, flow path and flow direction of each grid cell. The accuracy of this delineation is highly dependent on the DEM grid size and accuracy as the terrain attributes are derived from DEM. These results should further be validated by sUAS orthomosaics or high resolution satellite images or field data.

Machine learning is best for automated delineation of microtopographic features over a large area. Other than terrain attributes, we can also include other characteristics of terrain such as vegetation type to delineate the microtopographic features. Although preparing a training data set can be time consuming , it can provide useful information over a watershed scale once the machine learning algorithms are trained.

1.5.2 Evaluation of microtopographic features

The physical characteristics of microtopographic features such as surface area, volume, and depth of hollows, also referred to as morphometric data can be derived from LiDAR data and calculated using several methods. Stovall et al. (26) quantified fine-scale microtopography and delineated hummocks estimating the height, area, volume, and perimeter of individual hummock features. Both Stovall et al. (26) and Lovitt et al. (80) used a moving window average as an elevation threshold to classify microtopography. Brooks and Hayashi (112) used morphometric data and maximum depth (dmax) to measure vernal pools' maximum volume (Vmax), maximum area (Amax), and a p-coefficient to represent the shape of the basin as shown in equation (1).

$$V_{max} = (A_{max} d_{max})/(1 + 2/p) \tag{1.1}$$

where p <1 represents a convex basin and p >1 corresponds to a concave basin.

A similar approach was used by Gamble and Mitsch (113) for the calculation of wetland area (Amax), depth (dmax), and volume (Vmax) for depressional wetlands as shown in equation (2).

$$V_{max} = (0.3219 A_{max} d_{max}) \tag{1.2}$$

The morphometric data for Figure 1.6 is shown in Figure 1.7

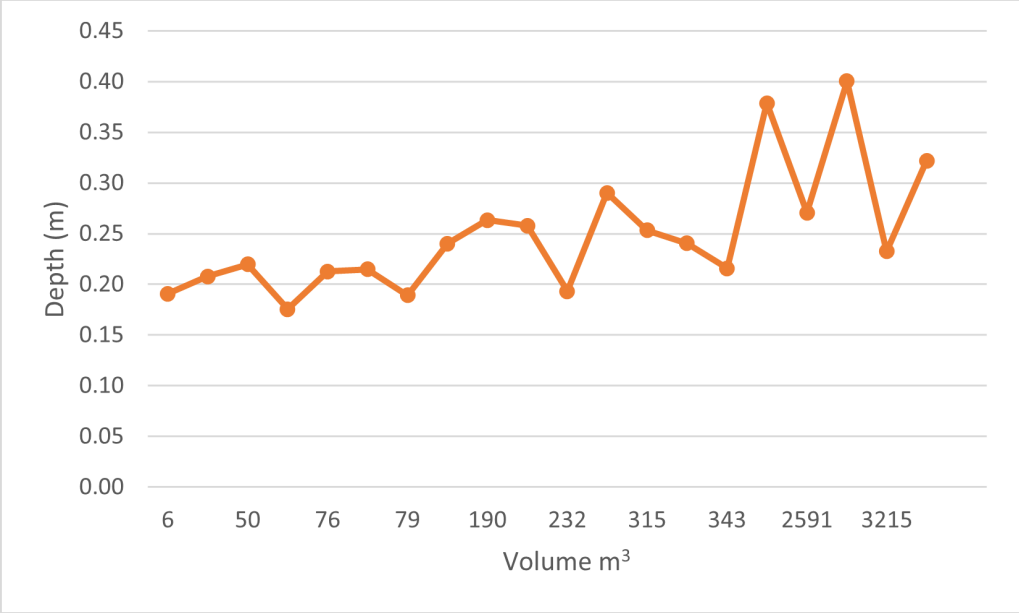

Figure 1.7: The graph shows the morphometric data of the delineated hollows shown in Figure 1.6 - volume in cubic meters and depth in meters for each of the delineated hollows.

Once microtopographic features are classified and delineated, these features (e.g., hollows or hummocks) are spatial categorical variables that can be further analyzed with landscape metrics (63). Landscape metrics include, but are not limited to, connectivity, microtopographic features' shape, size, area, perimeter, diversity, and fragmentation (microtopographic features are represented as landscape patches-spatial categorical variables). These metrics can provide important insights into the microtopography studies which can assist researchers to assess its impact on ecological, hydrological, and biogeochemical processes in terms of the composition and configuration of microtopographic patches. Here we show an example of a low-relief wetland area which is categorized based on elevation and water level and analyzed the landscape metrics for the microtopographic features. Figure 1.8 shows the tidal wetland landscape classified into microtopographic features hollows, hollow fringe, and hummocks using an elevation threshold approach. The data was collected using terrestrial LiDAR. This method clearly delineated the tidal channel present in the study area.

This channel becomes inundated during high tides but remains exposed to air during the low tides. The corresponding landscape metrics are shown in Table 1.3.

There are more than 50 landscape metrics that have been reported so far in the literature (114). These metrics are designed at patch (e.g., individual hollow patches), class (e.g., hollow or non-hollow), or landscape levels and can be used to quantify spatial features of microtopographic patches at different levels. For instance, the Aggregation index describes how different microtopographic features are spatially associated with one another. The clumpiness index indicates how microtopographic features are aggregated or dispersed. The higher value indicates a more clumped distribution of features while lower values show dispersed distribution. The contiguity index provides information on how microtopographic features are connected. The tidal channel at the study site was characterized by a higher contiguity index compared to hollow fringe and hummocks. Perimeter to area ratio indicates the shape complexity of the features and sensitivity to the feature size. The above indices show that the microtopographic features are more aggregated and clumped in the tidal bottomland forest (Figure 1.8 and Table 1.3).

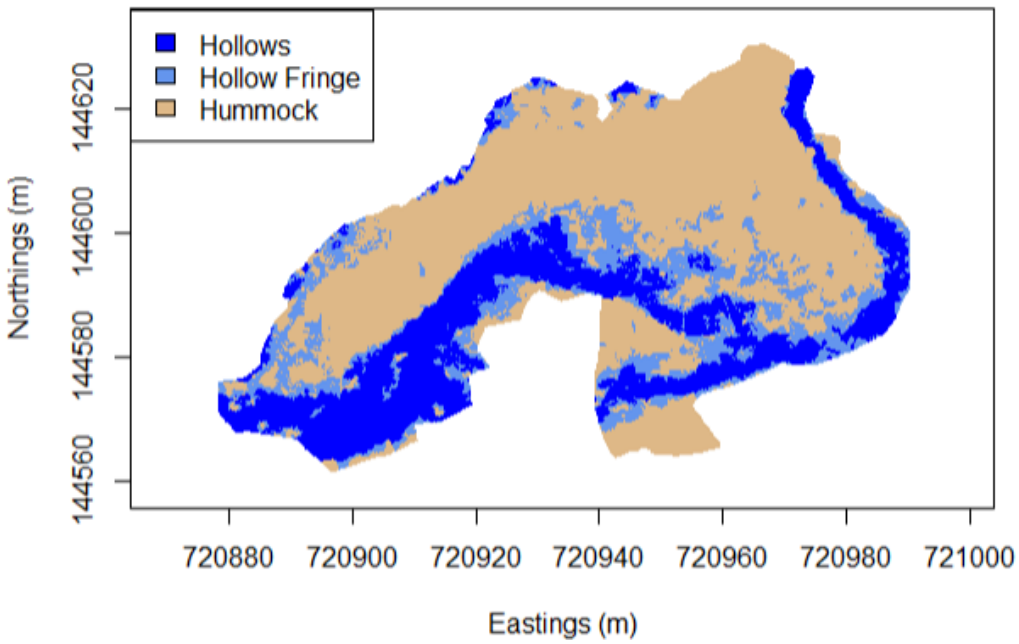

Figure 1.8: Landscape categorization based on elevation threshold: microtopographic features - hollows (< 0.65 m), hollows fringe (0.65 to 0.80 m) and hummocks (> 0.80 m) based on terrestrial LiDAR DEM with grid cell size 0.25 m X 0.25m in a low relief tidal wetland at Huger Creek area in Santee Experimental Forest, South Carolina.

Table 1.3: Landscape metrics (mean values) calculated for a tidal bottomland forest (Figure 1.8) (114).

Landscape metrics	Hollows	Fringe (m)	Hummocks
Aggregation Index	0.93	0.75	0.95
Clumpiness Index	0.91	0.70	0.90
Contiguity Index	0.42	0.26	0.22
Mean perimeter area ratio	8.62	11.37	12.01
Percentage of landscape	25.27	17.90	56.53
Mean shape index	1.25	0.97	0.65

1.5.3 Accuracy Assessment

The classification of microtopographic features can be validated by producer accuracy (PU), user accuracy (UA), and overall accuracy (OA), which have been well

studied in the literature of remote sensing (115). The computation of kappa estimates is another popular approach to validate the results. The overall accuracy is usually expressed in percent by taking a summation of correctly classified values and dividing by the total number of values. Producer accuracy, as the name suggests is from the viewpoint of a map producer, it is the calculated number of correctly classified values in a class divided by the total number of values in that class (column total). User accuracy is calculated as the total number of correct classifications for a particular class divided by the row total. The Kappa coefficient ranges from -1 to +1 where a negative value indicates classification is significantly worse than random (by chance) and a value close to 1 shows that classification is significantly better than random. When conducting a study at multiple DEM resolutions it is worth reporting results of multiple accuracy metrics (instead of single metric) for performed classifications as each metric has its own power (see (116))

1.6 Discussion

Small elevation changes in the natural ecosystems can have a significant effect on ecosystem processes such as biogeochemical reactions. The spatial heterogeneity of different processes requires analysis of microtopography, spatially and temporally at an appropriate scale. For instance, we often observe a wide range of GHG emissions measured within a type of ecosystem, for example, coastal wetlands (117). One of the possible reasons for these variations is a strong association of GHG emissions with wetland microtopography, which is not incorporated in most biogeochemical models. As suggested by Shi et al. (118), modification of the existing models by incorporating microtopography to assess C exchange results in improved prediction of C emissions.

To represent the microtopography of any study region requires the collection of a huge amount of data which enables researchers to delineate microtopographic features of interest such as hummocks, mounds, and hollows or pits for further analysis. The collection of data can be challenging particularly in forested areas due to their vegetation coverage that is often dense. The vegetation obscures the ground and therefore the data collection process should be well planned. It may require multiple flights or scans to cover a relatively small study area. sUAS and LiDAR-based technology is most suitable in forested wetlands for microtopographic studies while these technologies along with traditional aerial LiDAR and high-resolution satellite images can also be used in areas with limited vegetative cover.

In forested or vegetated regions LiDAR-based data acquisition is most suitable. For microtopographic studies, data should be collected when vegetation is senesced to ensure minimum occlusion. LiDAR scanner should be set at high point cloud density (approximately 10 to 20 million pulses per scan) and data acquisition should be carried out with multiple overlaps with scan distance not more than 15m. With aerial LiDAR data the point density is impacted by the flight altitude and speed of the aircraft. LiDAR based on sUAS are most suitable for forested regions as the flight

operation can be conducted at a lower altitude and speed can be controlled as low as 5 m/s.

As of now microtopography is only analyzed or studied as a static spatial phenomenon. It is our understanding that microtopographic features should be analyzed temporally as the spatial heterogeneity varies not only with location but also along the temporal dimension. The ecological, hydrological, or biogeochemical processes exert an impact on the microtopography by erosion or deposition. The temporal element can highlight the impact of such processes on microtopography and vice versa. This can provide useful insights into wetland and forest management. For example, it will also be interesting to see the spatiotemporal impact of saltwater intrusion on microtopography. Our current use of microtopographic representation is mainly limited to the creation of a single static DEM. It has an implicit assumption that microtopography is static and not changing but we need to ask if is that true. This becomes a more relevant question when we say microtopography is not only influenced by elevation but also by other terrain attributes. We also need to investigate how to present and integrate the temporal information of terrain attributes into the microtopographic models if we are to adequately investigate dynamics in microtopography.

Another issue involved with the use of high-resolution microtopographic data is the registration of scans or image alignment in forested environments. The absence of artificial objects makes it challenging to stitch together a large number of scans or images. More spherical targets and GCPs are needed in the case of terrestrial LiDAR scans and sUAS image data collection to ensure successful registration/alignment. Although data can be collected most times of the year in open wetlands, limited time is available for the data collection in forested or vegetated areas and data collection must be planned during the dormant season to reduce the occlusion from vegetation. Direct georeferencing methods can be useful in mapping as they do not require establishing GCPs. Padro et al. (119) compared different direct georeferencing methods

and an indirect georeferencing method and found onboard raw GNSS yielded a positional accuracy in excess of one meter with a vertical accuracy in the range of 4m or higher. However, the post-processed kinematic (PPK) single-frequency carrier-phase without in situ ground support and with ground support were of decimetric and centimetric accuracies. The results were improved further with GCP yielding centimetric accuracy. This shows that other than the GPS method of georeferencing, PPK based direct georeferencing method can be utilized for forest and wetland microtopographic studies. In this method, the nearest pseudo reference station (PRS) receives differential corrections which further corrects the onboard GNSS position.

1.6.1 Microtopography with Data Fusion

Data fusion of different data outputs can provide more insights into natural ecosystems as it combines the information from several sensor sources and can provide a more holistic view of a study system. The methodology of data fusion approaches to delineate high-resolution topography can provide direction to adopt ideal ways to represent surface microtopography. Data fusion is not restricted to merging information from different platforms and sensors but also different spatial and temporal scale matching. A reference frame can be defined to which data from different sources and time periods can be transformed. In the future, we propose remote sensing-based microtopography studies which consist of multi-source data integration in the natural ecosystem modeling and an explicit examination of the impact of scale. The collection of field data with explicit topographic information can be used for calibration and validation of the datasets. In addition, data fusion techniques which require combining two or more sensor output data can be useful in analyzing microtopography. There are studies that utilized data fusion techniques which include point cloud data of terrestrial LiDAR and sonar data to map the geomorphology and topography of the hydraulic structures to the study of scours (73). These studies can be extended to the field of microtopography mapping to generate a more holistic view of wetland

and forest systems.

High-resolution satellite data is a relatively new data source for microtopographic studies. Beginning with study areas without canopy cover and then progressing towards more forested study regions. The high-resolution satellite images can provide useful tools to assess GHG emissions, or explore biogeochemistry in relation to microtopography in no/sparsely vegetated regions, although this needs more research. Satellite data used in combination with sUAS or LiDAR data can provide useful information with respect to the impact of microtopography on ecosystem parameters. There are multiple low-orbiting small satellites that can capture images at high spatial, temporal, and spectral resolutions. The list of satellites that provide submeter resolution panchromatic images today are 1) WorldView-1 (50cm), WorldView-2 (50cm), WorldView-3 (30cm), GeoEye (50cm), Pleiades-1A (50 cm), Pleiades-1B (50cm), Pleiades-Neo (30cm), SuperView-1 (50cm), KOMPSAT-3 (70cm), IKONOS (80cm), SkySat (72 cm to 86 cm panchromatic and 1.00m multispectral). Also combining these high-resolution satellite images can provide a context to a study region and its importance.

These high-resolution images can assist in precision agriculture applications, forest canopy estimation, and urban planning. These data sources are currently not being used for assessing microtopography in forested regions, likely because the ground is obscured by the overstory and understory vegetation. The synthetic aperture radar (SAR) which uses an active data collection process means that its sensor produces its own energy and can provide high spatial resolution data compared to other satellite data. As of now, SAR is most suitable for topographic mapping due to its high penetration but its applicability to study microtopography in natural ecosystems is still a matter of research. In the last five years, researchers are actively working on developing algorithms to create high-resolution DEM from SAR data. For example, (120) proposed dual frequency and dual baseline (DFDB) configuration in airborne

SAR interferometry (InSAR) and a baseline calibration algorithm to create a high-resolution DEM in tidal flats. In their proof of concept, the authors claimed a high vertical accuracy in the sub-meter range. Another study, (121) developed a model for measuring topographic changes in tidal flats and relied on minimizing the errors due to height and interferometric phase deviation. In the InSAR methodology, the quality of the interferogram is based on master and slave images which means high coherence is important to ensure the accuracy in DEM. The study area examined by both studies is without the canopy cover. Nonetheless, satellite data can be combined with close-range remote sensing technologies to provide greater insights over a large aerial extent.

1.6.2 Utilizing advanced techniques

New LiDAR technologies such as Geiger mode, single photon, and FLASH splits the single laser pulse into multiple pulses. This results in a greater number of returns and therefore a denser point cloud with more information. Such systems can penetrate through a dense forest canopy and detect the microtopography in a forested area although the laser penetration or the number of returns from the ground decreases with increasing tree canopy or ground vegetation cover. These LiDAR systems are more sensitive than earlier LiDAR scanners and are able to detect weak return signals. The lighter weight of these technologies also makes them ideal for flying at lower altitudes. In addition, aerial LiDAR data are regularly spaced and not very prone to shadowing effects in contrast to aerial photogrammetric techniques.

Moreover, the availability of LiDAR sensors in different wavelengths enables us to choose the sensor based on the research question. Researchers (122; 123; 124) have conducted studies to identify wavelength appropriate for vegetation/species classification. The typical wavelengths associated with aerial topographic LiDAR are 1064nm, 1550nm, and 905nm, and bathymetric LiDAR are green-532nm and infrared (1064 or 1550 nm) (125). Bathymetric LiDAR are composed of green and infrared beams.

The green beam can propagate in water and assist us in finding useful information on bathymetry while infrared beams are reflected by the water providing the water surface elevation.

1.6.3 Microtopography with bathymetry

The technologies used for bathymetric surveys include echosounders, total station/RTK GPS, unmanned surface vessels (USV), UAS, airborne LiDAR Bathymetry (ALB), and Green-wavelength terrestrial laser scanning (GWTLS). Satellite-derived bathymetric data is of medium resolution and may not be appropriate for the micro-topographic studies often operating at small spatial scales. The inundated portion of a wetland or lacustrine margins can also be mapped using bathymetric LiDAR or SfM surveys. For example, coastal zone mapping imaging LiDAR (CZMIL) can not only map the above water topography but the green laser can also penetrate water to some depth and produce high-resolution bathymetric data. Shallow water where boats can not be launched or the streams/rivers or regions which are inaccessible to boats with traditional sonar equipment can be surveyed using RTK GPS or total station. Technologies such as CZMIL and GWTLS have been used for nearshore bathymetry under clear atmospheric and water conditions where the water depth is less than 1m providing high-resolution microtopography (126). The laser-based bathymetric measurements are corrected by applying refraction correction which requires specification of water surface level and refractive index. The refractive index is 1.335 for green lasers passing from air to clear water. The submerged point clouds are corrected for refraction while the ground points maintain their original coordinates.

Other than LiDAR surveys, echosounders are the conventional surveying technique used for high-resolution microtopography. It is important to control the speed of the surveying vessel to ensure high point density. The echosounders are generally equipped with a GPS system that provides the coordinates of the measuring point. Unlike LiDAR systems, the echosounders are not restricted by the depth of the water

and can survey rivers and streams. The microtopography of deeper river bed deformation or in other words, scour or deposition can be measured using echosounders (127).

1.6.4 Acceleration of Microtopographic Data Analytics

High-resolution microtopographic data collected via close-range remote sensing techniques are often in large volume i.e., big data (128). The use of these high-resolution data comes with its own challenges when we manage, process, analyze and visualize them (e.g., registration and aligning point cloud data, performing different statistical analyses on point cloud data, and processing high-resolution images and mosaics). The processing and analytics of large-volume microtopographic data are often computationally demanding, which can be overcome by using high-performance and parallel computing approaches to leverage cyberinfrastructure-enabled computing resources (129; 130).

The processing and analysis of large microtopographic data can be split into smaller computing tasks that can be allocated to multiple computing elements for acceleration. For example, Barnes et al.(131) developed a parallel priority-flood algorithm for depression filling of large DEM data. A large DEM data was decomposed into individual tiles on which depression-filling operations were applied. Barnes (131) tested the parallel depression filling algorithm on a series of DEM datasets and significant speed up was obtained (only 287 minutes were needed when using 48 CPUs for parallel processing of the SRTM DEM dataset, compared to 223 hours for sequential time using 1 CPU). Zheng et al. (130) implemented a parallel spatial interpolation approach that relies on 2D spatial domain decomposition for the processing of DEM from LiDAR data. As a result, the overall computing time was reduced from over 17 hours down to within 1 hour by using 18 CPUs. High-performance and parallel computing as a key capability of advanced cyberinfrastructure have a variety of applications, and it has great potential in accelerating microtopographic data processing and analytics.

1.7 Conclusion

In this article we provide a systematic data-driven framework to guide the study of microtopography using close-range remote sensing. Our framework focuses on four components: terrain attributes, spatial resolution, data acquisition, and assessment of microtopography. Terrain attributes based on elevation (e.g., slope, aspect, curvature, TWI, TPI, flow path, and flow accumulation) dominate the choice of quantitative measures for microtopography. Further, landscape metrics can also be used for quantification once microtopography is classified or delineated as, for example, hummocks or hollows (spatial categorical variable). With respect to spatial resolution, a high-resolution DEM (often at the sub-meter level) is needed to adequately account for microtopographic characteristics as microtopography-driven phenomena often operate at a small spatial scale. On one hand, we need to make sure the spatial resolution to be used is finer than the operational scale of microtopography. On the other hand, the use of very fine spatial resolutions for microtopographic data will lead to a big data challenge due to the high volume of data to be handled.

Alternative close-range remote sensing techniques (sUAS, aerial LiDAR, and terrestrial LiDAR) have their own advantages and limitations in terms of time, labor, and accuracy. It is important to take into account these aspects together with terrain attributes and spatial resolutions for efficacious microtopographic data acquisition. Remote sensing techniques especially through ALS, TLS, and sUAS can produce DEMs of high resolution and can provide fine-scale measurements of microtopography in natural ecosystems. The combination of one or more techniques of aerial LiDAR, terrestrial LiDAR, sUAS, and high-resolution satellite images is the way forward to characterize the microtopography in complex environments including forests, coastal wetlands, and forested wetlands. Combining remote sensing techniques with field measurements which include but are not limited to water level data, soil moisture, soil pH, trace gas emissions, and RTK GPS data for location accuracy can provide a

robust tool for predicting and assessing the ecosystem functions influenced by the microtopography. There is also a need for increasing the availability of microtopographic data through increased sharing of datasets on platforms like OpenTopography and accelerating microtopographic data processing and analytics via cyberinfrastructure-enabled high-performance computing capabilities. New field-scale measurements of biogeochemical and hydrologic processes that are explicitly linked to topographic metadata are required to further realize the potential of these new technologies and algorithms. The higher 3D point cloud density generated from close range remote sensing leads to greater accuracy of DEM with lower RMSE (e.g., less than 0.5 m). Our review makes it clear that heterogeneity in topography of the natural ecosystem influences the biogeochemical and hydrologic processes, which should be included in the ecosystem models when microtopography plays an inevitable role. We also emphasize the need to model microtopographic features better to investigate their impact on ecosystem processes by including field based observations into the models (i.e., model calibration and validation).

The assessment of microtopography typically includes the delineation and evaluation of microtopographic features. There are three delineation approaches including threshold-, mechanistically-, and machine learning-based. While the first two approaches have been extensively used in the literature of microtopographic studies, machine learning and deep learning algorithms hold great potential in the automated delineation of microtopographic features and application in large study regions. More machine learning-based studies are highly expected in the near foreseeable future as deep learning-driven artificial intelligence has been increasingly driving the data-intensive studies such as microtopographic data analytics in this study.

Overall the framework discussed in this article may improve our understanding of microtopography by using close-range remote sensing as a quantitative approach. In future studies, we will focus on specific applications or case studies of microtopography-

driven geospatial phenomena, which will provide more detailed exploration and comparison of close-range remote sensing techniques with respect to their capabilities for empowering microtopography studies. Further, we will explore the power of machine learning-based approaches in the analytics of sophisticated microtopographic data (e.g., automated delineation and recognition of microtopographic features) as well as the utility of high-performance computing in accelerating these analytics that is often computationally considerable.

1.8 References

[1] T. Shukla, W. Tang, C. C. Trettin, G. Chen, S. Chen, and C. Allan, "Quantifying microtopography in natural ecosystems using close-range remote sensing.," *Remote Sens*, vol. 15, no. 9, p. 2387, 2023.

[2] J. L. Bubier, T. R. Moore, and N. T. Roulet, "Methane emissions from wetlands in the midboreal region of northern ontario, canada," *Ecology*, vol. 74, pp. 2240–2254, Dec. 1993.

[3] J. D. Graham, N. F. Glenn, L. P. Spaete, and P. J. Hanson, "Characterizing peatland microtopography using gradient and Microform-Based approaches," *Ecosystems*, vol. 23, no. 7, pp. 1–17, 2020.

[4] M. E. McClain, E. W. Boyer, C. L. Dent, S. E. Gergel, N. B. Grimm, P. M. Groffman, S. C. Hart, J. W. Harvey, C. A. Johnston, E. Mayorga, W. H. McDowell, and G. Pinay, "Biogeochemical hot spots and hot moments at the interface of terrestrial and aquatic ecosystems," *Ecosystems*, vol. 6, no. 4, pp. 301–312, 2003.

[5] P. F. Sullivan, S. J. T. Arens, R. A. Chimner, and J. M. Welker, "Temperature and microtopography interact to control carbon cycling in a high arctic fen," *Ecosystems*, vol. 11, pp. 61–76, Feb. 2008.

[6] G. L. Chmura, S. C. Anisfeld, D. R. Cahoon, and J. C. Lynch, "Global carbon sequestration in tidal, saline wetland soils," *Global Biogeochem. Cycles*, vol. 17, Dec. 2003.

[7] T. R. Moore, A. De Young, J. L. Bubier, E. R. Humphreys, P. M. Lafleur, and N. T. Roulet, "A Multi-Year record of methane flux at the mer bleue bog, southern canada," *Ecosystems*, vol. 14, p. 646, Apr. 2011.

[8] M. Helbig, L. E. Chasmer, N. Kljun, W. L. Quinton, C. C. Treat, and O. Sonnentag, "The positive net radiative greenhouse gas forcing of increasing methane emissions from a thawing boreal forest-wetland landscape," *Glob. Chang. Biol.*, vol. 23, pp. 2413–2427, June 2017.

[9] G. J. Whiting and J. P. Chanton, "Greenhouse carbon balance of wetlands: methane emission versus carbon sequestration," *Tellus B Chem. Phys. Meteorol.*, vol. 53, pp. 521–528, Nov. 2001.

[10] Z. Zhang, N. E. Zimmermann, A. Stenke, X. Li, E. L. Hodson, G. Zhu, C. Huang, and B. Poulter, "Emerging role of wetland methane emissions in driving 21st century climate change," *Proc. Natl. Acad. Sci. U. S. A.*, vol. 114, pp. 9647–9652, Sept. 2017.

[11] A. Bullock and M. Acreman, "The role of wetlands in the hydrological cycle," *Hydrol. Earth Syst. Sci.*, vol. 7, pp. 358–389, June 2003.

[12] C. R. Lane, S. G. Leibowitz, B. C. Autrey, S. D. LeDuc, and L. C. Alexander, "Hydrological, physical, and chemical functions and connectivity of non-floodplain wetlands to downstream waters: A review," *J. Am. Water Resour. Assoc.*, vol. 54, pp. 346–371, Mar. 2018.

[13] J. Courtwright and S. E. G. Findlay, "Effects of microtopography on hydrology, physicochemistry, and vegetation in a tidal swamp of the Hudson River," *Wetlands*, vol. 31, pp. 239–249, Apr. 2011.

[14] S. Frei, G. Lischeid, and J. H. Fleckenstein, "Effects of micro-topography on surface–subsurface exchange and runoff generation in a virtual riparian wetland—a modeling study," *Adv. Water Resour.*, vol. 33, no. 11, pp. 1388–1401, 2010.

[15] A. R. Korol and G. B. Noe, "Patterns of denitrification potential in tidal freshwater forested wetlands," *Estuaries Coasts*, vol. 43, pp. 329–346, Mar. 2020.

[16] G. Miao, A. Noormets, J.-C. Domec, M. Fuentes, C. C. Trettin, G. Sun, S. G. McNulty, and J. S. King, "Hydrology and microtopography control carbon dynamics in wetlands: Implications in partitioning ecosystem respiration in a coastal plain forested wetland," *Agric. For. Meteorol.*, vol. 247, pp. 343–355, Dec. 2017.

[17] Trettin, Czwartacki, Allan, and others, "Linking freshwater tidal hydrology to carbon cycling in bottomland hardwood wetlands," *In: Stringer, Christina E.; Krauss, Ken W.; Latimer, James S., eds Headwaters to estuaries: advances in watershed science and management-Proceedings of the Fifth Interagency Conference on Research in the Watersheds. March 2-5, 2015, North Charleston, South Carolina. e-General Technical Report SRS-211. Asheville, NC: US Department of Agriculture Forest Service, Southern Research Station. 2016, 302 p.*, 2016.

[18] M. B. Eppinga, P. C. de Ruiter, M. J. Wassen, and M. Rietkerk, "Nutrients and hydrology indicate the driving mechanisms of peatland surface patterning," *Am. Nat.*, vol. 173, pp. 803–818, June 2009.

[19] S. Frei, K. H. Knorr, S. Peiffer, and J. H. Fleckenstein, "Surface microtopography causes hot spots of biogeochemical activity in wetland systems: A virtual modeling experiment," *J. Geophys. Res.*, vol. 117, Dec. 2012.

[20] N. Yamashita, S. Ishizuka, S. Hashimoto, S. Ugawa, K. Nanko, Y. Osone, J. Iwahashi, Y. Sakai, M. Inatomi, A. Kawanishi, K. Morisada, N. Tanaka, S. Aizawa, A. Imaya, M. Takahashi, S. Kaneko, S. Miura, and K. Hirai, "National-scale 3D

mapping of soil organic carbon in a japanese forest considering microtopography and tephra deposition," *Geoderma*, vol. 406, p. 115534, Jan. 2022.

[21] L. F. Huenneke and R. R. Sharitz, "Microsite abundance and distribution of woody seedlings in a south carolina Cypress-Tupelo swamp," *Am. Midl. Nat.*, vol. 115, no. 2, pp. 328–335, 1986.

[22] J. H. Titus, "Microtopography and woody plant regeneration in a hardwood floodplain swamp in florida," *Bull. Torrey Bot. Club*, vol. 117, no. 4, pp. 429–437, 1990.

[23] B. P. Bledsoe and T. H. Shear, "Vegetation along hydrologic and edaphic gradients in a North Carolina coastal plain creek bottom and implications for restoration," *Wetlands*, vol. 20, no. 1, pp. 126–147, 2000.

[24] K. Moser, C. Ahn, and G. Noe, "Characterization of microtopography and its influence on vegetation patterns in created wetlands," *Wetlands*, vol. 27, pp. 1081–1097, Dec. 2007.

[25] J. S. Diamond, J. M. Epstein, M. J. Cohen, D. L. McLaughlin, Y. Hsueh, R. F. Keim, and J. A. Duberstein, "A little relief: Ecological functions and autogenesis of wetland microtopography," *Wiley Interdisciplinary Reviews: Water*, vol. 8, no. 1, p. e1493, 2021.

[26] A. E. L. Stovall, J. S. Diamond, R. A. Slesak, D. L. McLaughlin, and H. Shugart, "Quantifying wetland microtopography with terrestrial laser scanning," *Remote Sens. Environ.*, vol. 232, p. 111271, 2019.

[27] A. Baltensweiler, G. B. M. Heuvelink, M. Hanewinkel, and L. Walthert, "Microtopography shapes soil pH in flysch regions across Switzerland," *Geoderma*, vol. 380, p. 114663, Dec. 2020.

[28] J. S. Diamond, D. L. McLaughlin, R. A. Slesak, and A. Stovall, "Pattern and structure of microtopography implies autogenic origins in forested wetlands," *Hydrol. Earth Syst. Sci.*, vol. 23, pp. 5069–5088, Dec. 2019.

[29] M. Strack, J. M. Waddington, L. Rochefort, and E.-S. Tuittila, "Response of vegetation and net ecosystem carbon dioxide exchange at different peatland microforms following water table drawdown," *J. Geophys. Res.*, vol. 111, June 2006.

[30] X. Xie, A. Li, J. Tian, C. Wu, and H. Jin, "A fine spatial resolution estimation scheme for large-scale gross primary productivity (GPP) in mountain ecosystems by integrating an eco-hydrological model with the combination of linear and non-linear downscaling processes," *J. Hydrol.*, vol. 616, p. 128833, Jan. 2023.

[31] S. K. Nouwakpo, M. A. Weltz, K. C. McGwire, J. C. Williams, A.-H. Osama, and C. H. M. Green, "Insight into sediment transport processes on saline rangeland hillslopes using three-dimensional soil microtopography changes," *Earth Surface Processes and Landforms*, vol. 42, no. 4, pp. 681–696, 2017.

[32] C. J. Williams, F. B. Pierson, P. R. Robichaud, O. Z. Al-Hamdan, J. Boll, and E. K. Strand, "Structural and functional connectivity as a driver of hillslope erosion following disturbance," *Int. J. Wildland Fire*, vol. 25, no. 3, p. 306, 2016.

[33] J. S. Diamond, D. L. Mclaughlin, R. A. Slesak, and A. Stovall, "Microtopography is a fundamental organizing structure of vegetation and soil chemistry in black ash wetlands," *Biogeosciences*, vol. 17, no. 4, pp. 901–915, 2020.

[34] J. D. Graham, D. M. Ricciuto, N. F. Glenn, and P. J. Hanson, "Incorporating

microtopography in a land surface model and quantifying the effect on the carbon cycle," *J. Adv. Model. Earth Syst.*, vol. 14, Feb. 2022.

[35] M. Kalacska, J. P. Arroyo-Mora, and O. Lucanus, "Comparing UAS LiDAR and Structure-from-Motion photogrammetry for peatland mapping and virtual reality (VR) visualization," *Drones*, vol. 5, p. 36, May 2021.

[36] P. A. Moore, M. C. Lukenbach, D. K. Thompson, N. Kettridge, G. Granath, and J. M. Waddington, "Assessing the peatland hummock–hollow classification framework using high-resolution elevation models: implications for appropriate complexity ecosystem modeling," *Biogeosciences*, vol. 16, no. 18, pp. 3491–3506, 2019.

[37] C. E. Johnson, J. J. Ruiz-Méndez, and G. B. Lawrence, "Forest soil chemistry and terrain attributes in a catskills watershed," *Soil Sci. Soc. Am. J.*, vol. 64, pp. 1804–1814, Sept. 2000.

[38] K. M. Brubaker, W. L. Myers, P. J. Drohan, D. A. Miller, and E. W. Boyer, "The use of LiDAR terrain data in characterizing surface roughness and micro-topography," *Applied and Environmental Soil Science*, vol. 2013, Apr. 2013.

[39] J. J. Mercer and C. J. Westbrook, "Ultrahigh–resolution mapping of peatland microform using groundâbased structure from motion with multiview stereo," *J. Geophys. Res. Biogeosci.*, vol. 121, pp. 2901–2916, Nov. 2016.

[40] J. M. Knight, P. E. R. Dale, J. Spencer, and L. Griffin, "Exploring LiDAR data for mapping the micro-topography and tidal hydro-dynamics of mangrove systems: An example from southeast Queensland, Australia," *Estuar. Coast. Shelf Sci.*, vol. 85, no. 4, pp. 593–600, 2009.

[41] E. Rodríguez-Caballero, Y. Cantón, S. Chamizo, R. Lázaro, and A. Escudero, "Soil loss and runoff in semiarid ecosystems: A complex interaction between

biological soil crusts, micro-topography, and hydrological drivers," *Ecosystems*, vol. 16, pp. 529–546, June 2013.

[42] Z. S. Brecheisen and D. D. Richter, "Gully-erosion estimation and terrain reconstruction using analyses of microtopographic roughness and LiDAR," *Catena*, vol. 202, p. 105264, July 2021.

[43] M. B. Siewert, J. Hanisch, N. Weiss, P. Kuhry, T. C. Maximov, and G. Hugelius, "Comparing carbon storage of siberian tundra and taiga permafrost ecosystems at very high spatial resolution," *J. Geophys. Res. Biogeosci.*, vol. 120, pp. 1973–1994, Oct. 2015.

[44] M. W. Smith and J. Warburton, "Microtopography of bare peat: a conceptual model and objective classification from high-resolution topographic survey data," *Earth Surf. Processes Landforms*, vol. 43, pp. 1557–1574, June 2018.

[45] S. J. Davidson, M. J. Santos, V. L. Sloan, K. Reuss-Schmidt, G. K. Phoenix, W. C. Oechel, and D. Zona, "Upscaling CH_4 fluxes using High-Resolution imagery in arctic tundra ecosystems," *Remote Sensing*, vol. 9, p. 1227, Nov. 2017.

[46] G. Bisht, W. J. Riley, H. M. Wainwright, B. Dafflon, F. Yuan, and V. E. Romanovsky, "Impacts of microtopographic snow redistribution and lateral subsurface processes on hydrologic and thermal states in an arctic polygonal ground ecosystem: a case study using ELM-3D v1.0," *Geoscientific Model Development*, vol. 11, no. 1, pp. 61–76, 2018.

[47] A. Jan, E. T. Coon, J. D. Graham, and S. L. Painter, "A subgrid approach for modeling microtopography effects on overland flow," *Water Resources Research*, vol. 54, no. 9, pp. 6153–6167, 2018.

[48] C. J. Abolt and M. H. Young, "High-resolution mapping of spatial heterogeneity

in ice wedge polygon geomorphology near Prudhoe Bay, Alaska," *Sci Data*, vol. 7, p. 87, Mar. 2020.

[49] N. Falco, H. Wainwright, B. Dafflon, E. Léger, J. Peterson, H. Steltzer, C. Wilmer, J. C. Rowland, K. H. Williams, and S. S. Hubbard, "Investigating microtopographic and soil controls on a mountainous meadow plant community using high–resolution remote sensing and surface geophysical data," *J. Geophys. Res. Biogeosci.*, vol. 124, pp. 1618–1636, June 2019.

[50] J. V. Solórzano, J. A. Gallardo-Cruz, C. Peralta-Carreta, R. Martínez-Camilo, and A. F.-M. de Oca, "Plant community composition patterns in relation to microtopography and distance to water bodies in a tropical forested wetland," *Aquat. Bot.*, vol. 167, p. 103295, 2020.

[51] C. Alexander, B. Deák, and H. Heilmeier, "Micro-topography driven vegetation patterns in open mosaic landscapes," *Ecol. Indic.*, vol. 60, pp. 906–920, Jan. 2016.

[52] A. Cici, A. H. Korstjens, and R. A. Hill, "Influence of micro-topography and crown characteristics on tree height estimations in tropical forests based on LiDAR canopy height models," *Int. J. Appl. Earth Obs. Geoinf.*, vol. 65, pp. 105–113, Mar. 2018.

[53] A. Harris and A. J. Baird, "Microtopographic drivers of vegetation patterning in blanket peatlands recovering from erosion," *Ecosystems*, vol. 22, no. 5, pp. 1035–1054, 2019.

[54] J. Devadoss, N. Falco, B. Dafflon, Y. Wu, M. Franklin, A. Hermes, E.-L. S. Hinckley, and H. Wainwright, "Remote Sensing-Informed zonation for understanding snow, plant and soil moisture dynamics within a mountain ecosystem," *Remote Sensing*, vol. 12, p. 2733, Aug. 2020.

[55] R. C. Leong, D. A. Friess, B. Crase, W. K. Lee, and E. L. Webb, "High-resolution pattern of mangrove species distribution is controlled by surface elevation," *Estuar. Coast. Shelf Sci.*, vol. 202, pp. 185–192, Mar. 2018.

[56] H. M. Wainwright, R. Oktem, B. Dafflon, S. Dengel, J. B. Curtis, M. S. Torn, J. Cherry, and S. S. Hubbard, "High-Resolution Spatio-Temporal estimation of net ecosystem exchange in ice-wedge polygon tundra using in situ sensors and remote sensing data," *Land*, vol. 10, p. 722, July 2021.

[57] S. Yelenik, E. Rose, S. Cordell, M. Victoria, and J. R. Kellner, "The role of microtopography and resident species in post-disturbance recovery of arid habitats in Hawai'i," *Ecol. Appl.*, vol. 32, p. e2690, Dec. 2022.

[58] A. F. Parker, P. R. Owens, Z. Libohova, X. B. Wu, L. P. Wilding, and S. R. Archer, "Use of terrain attributes as a tool to explore the interaction of vertic soils and surface hydrology in south Texas playa wetland systems," *J. Arid Environ.*, vol. 74, pp. 1487–1493, Nov. 2010.

[59] C.-F. Lee, W.-K. Huang, Y.-L. Chang, S.-Y. Chi, and W.-C. Liao, "Regional landslide susceptibility assessment using multi-stage remote sensing data along the coastal range highway in northeastern Taiwan," *Geomorphology*, vol. 300, pp. 113–127, Jan. 2018.

[60] M. Azarafza, M. Azarafza, H. Akgün, P. M. Atkinson, and R. Derakhshani, "Deep learning-based landslide susceptibility mapping," *Sci. Rep.*, vol. 11, p. 24112, Dec. 2021.

[61] K. Pawłuszek, A. Borkowski, and P. Tarolli, "Towards the optimal pixel size of dem for automatic mapping of landslide areas," *ISPRS - Int. Arch. Photogramm. Remote Sens. Spat. Inf. Sci.*, vol. XLII-1/W1, pp. 83–90, May 2017.

[62] R. Martínez Prentice, M. Villoslada Peciña, R. D. Ward, T. F. Bergamo, C. B. Joyce, and K. Sepp, "Machine learning classification and accuracy assessment from High-Resolution images of coastal wetlands," *Remote Sensing*, vol. 13, p. 3669, Sept. 2021.

[63] M. G. Turner, "Landscape ecology: What is the state of the science?," *Annu. Rev. Ecol. Evol. Syst.*, vol. 36, pp. 319–344, Dec. 2005.

[64] L. Bian, "Multiscale nature of spatial data in scaling up environmental models," *Scale in Remote Sensing and GIS*, pp. 13–26, 2023.

[65] N. S.-N. Lam and D. A. Quattrochi, "On the issues of scale, resolution, and fractal analysis in the mapping sciences," *Prof. Geogr.*, vol. 44, pp. 88–98, Feb. 1992.

[66] A. Baltensweiler, L. Walthert, C. Ginzler, F. Sutter, R. S. Purves, and M. Hanewinkel, "Terrestrial laser scanning improves digital elevation models and topsoil ph modelling in regions with complex topography and dense vegetation," *Environmental Modelling & Software*, vol. 95, pp. 13–21, Sept. 2017.

[67] N. Habtezion, M. Tahmasebi Nasab, and X. Chu, "How does DEM resolution affect microtopographic characteristics, hydrologic connectivity, and modelling of hydrologic processes?," *Hydrol. Process.*, vol. 30, pp. 4870–4892, Dec. 2016.

[68] J. B. Lindsay, "Whitebox GAT: A case study in geomorphometric analysis," *Comput. Geosci.*, vol. 95, pp. 75–84, Oct. 2016.

[69] K. J. Minick, A. M. Kelley, G. Miao, X. Li, A. Noormets, B. Mitra, and J. S. King, "Microtopography alters hydrology, phenol oxidase activity and nutrient availability in organic soils of a coastal freshwater forested wetland," *Wetlands*, vol. 39, pp. 263–273, Apr. 2019.

[70] Pérez-Ceballos, Echeverría-Ávila, A. Zaldivar-Jimenez, T. Zaldivar-Jimenez, and J. Herrera-Silveira, "Contribution of microtopography and hydroperiod to the natural regeneration of *avicennia germinans* in a restored mangrove forest," *Ciencias marinas*, vol. 43, no. 1, pp. 55–67, 2017.

[71] M. Wang, Y. Han, Z. Xu, S. Wang, M. Jiang, and G. Wang, "Hummock-hollow microtopography affects soil enzyme activity by creating environmental heterogeneity in the sedge-dominated peatlands of the Changbai Mountains, China," *Ecological Indicators*, vol. 121, p. 107187, 2021.

[72] P. J. Hardin, V. Lulla, R. R. Jensen, and J. R. Jensen, "Small unmanned aerial systems (sUAS) for environmental remote sensing: challenges and opportunities revisited," *GISci. Remote Sens.*, vol. 56, pp. 309–322, Feb. 2019.

[73] W. Tang, S.-E. Chen, J. Diemer, C. Allan, T. Chen, Z. Slocum, T. Shukla, V. S. Chavan, N. S. Shanmugam, and University of North Carolina at Charlotte. Dept. of Geography and Earth Sciences, "DeepHyd: A deep learning-based artificial intelligence approach for the automated classification of hydraulic structures from LiDAR and sonar data," Tech. Rep. FHWA/NC/2019-03, Jan. 2022.

[74] M. E. Hodgson and P. Bresnahan, "Accuracy of airborne lidar-derived elevation: Empirical assessment and error budget," *Photogrammetric engineering and remote sensing*, vol. 70, no. 3, pp. 331–340, 2002.

[75] D. Pinton, A. Canestrelli, B. Wilkinson, P. Ifju, and A. Ortega, "Estimating ground elevation and vegetation characteristics in coastal salt marshes using UAV-Based LiDAR and digital aerial photogrammetry," *Remote Sensing*, vol. 13, p. 4506, Nov. 2021.

[76] B. Almquist, S. B. Jack, and M. G. Messina, "Variation of the treefall gap

regime in a bottomland hardwood forest: relationships with microtopography," *For. Ecol. Manage.*, vol. 157, pp. 155–163, Mar. 2002.

[77] P. Koponen, P. Nygren, D. Sabatier, A. Rousteau, and E. Saur, "Tree species diversity and forest structure in relation to microtopography in a tropical freshwater swamp forest in french guiana," *Plant Ecol.*, vol. 173, pp. 17–32, July 2004.

[78] C. M. Agraz Hernández, C. García Zaragoza, S. Iriarte-Vivar, F. J. Flores-Verdugo, and P. Moreno Casasola, "Forest structure, productivity and species phenology of mangroves in the La Mancha Lagoon in the atlantic coast of Mexico," *Wetlands Ecol. Manage.*, vol. 19, pp. 273–293, June 2011.

[79] A. Lucieer, D. Turner, D. H. King, and S. A. Robinson, "Using an unmanned aerial vehicle (UAV) to capture micro-topography of antarctic moss beds," *Int. J. Appl. Earth Obs. Geoinf.*, vol. 27, pp. 53–62, Apr. 2014.

[80] J. Lovitt, M. M. Rahman, S. Saraswati, G. J. McDermid, M. Strack, and B. Xu, "UAV remote sensing can reveal the effects of low-impact seismic lines on surface morphology, hydrology, and methane (CH_4) release in a boreal treed bog," *J. Geophys. Res. Biogeosci.*, vol. 123, pp. 1117–1129, Mar. 2018.

[81] J. Kelly, N. Kljun, L. Eklundh, L. Klemedtsson, B. Liljebladh, P.-O. Olsson, P. Weslien, and X. Xie, "Modelling and upscaling ecosystem respiration using thermal cameras and UAVs: Application to a peatland during and after a hot drought," *Agric. For. Meteorol.*, vol. 300, p. 108330, Apr. 2021.

[82] S. K. Nouwakpo, M. A. Weltz, and K. McGwire, "Assessing the performance of structure-from-motion photogrammetry and terrestrial LiDAR for reconstructing soil surface microtopography of naturally vegetated plots," *Earth Surf. Processes Landforms*, vol. 41, pp. 308–322, Mar. 2016.

[83] D. G. Lowe, "Distinctive image features from Scale-Invariant keypoints," *Int. J. Comput. Vis.*, vol. 60, pp. 91–110, Nov. 2004.

[84] T. Becker, L. Kutzbach, I. Forbrich, J. Schneider, D. Jager, B. Thees, and M. Wilmking, "Do we miss the hot spots? – the use of very high resolution aerial photographs to quantify carbon fluxes in peatlands," *Biogeosciences*, vol. 5, pp. 1387–1393, Oct. 2008.

[85] J. R. K. Lehmann, W. Münchberger, C. Knoth, C. Blodau, F. Nieberding, T. Prinz, V. A. Pancotto, and T. Kleinebecker, "High-Resolution classification of south patagonian peat bog microforms reveals potential gaps in Up-Scaled CH_4 fluxes by use of unmanned aerial system (UAS) and CIR imagery," *Remote Sensing*, vol. 8, p. 173, Feb. 2016.

[86] J. Jeziorska, "UAS for wetland mapping and hydrological modeling," *Remote Sensing*, vol. 11, p. 1997, Aug. 2019.

[87] C. Mallet and F. Bretar, "Full-waveform topographic lidar: State-of-the-art," *ISPRS J. Photogramm. Remote Sens.*, vol. 64, pp. 1–16, Jan. 2009.

[88] L. Chasmer, C. Hopkinson, J. Montgomery, and R. Petrone, "A physically based terrain morphology and vegetation structural classification for wetlands of the boreal plains, Alberta, Canada," *Can. J. Remote Sens.*, vol. 42, pp. 521–540, Sept. 2016.

[89] M. W. Lang, V. Kim, G. W. McCarty, X. Li, I.-Y. Yeo, C. Huang, and L. Du, "Improved detection of inundation below the forest canopy using normalized LiDAR intensity data," *Remote Sensing*, vol. 12, p. 707, Feb. 2020.

[90] R. D. Ward, N. G. Burnside, C. B. Joyce, and K. Sepp, "The use of medium point density LiDAR elevation data to determine plant community types in baltic coastal wetlands," *Ecol. Indic.*, vol. 33, pp. 96–104, Oct. 2013.

[91] T. Hilker, M. van Leeuwen, N. C. Coops, M. A. Wulder, G. J. Newnham, D. L. B. Jupp, and D. S. Culvenor, "Comparing canopy metrics derived from terrestrial and airborne laser scanning in a douglas-fir dominated forest stand," *Trees*, vol. 24, pp. 819–832, Oct. 2010.

[92] E. Rodríguez-Caballero, A. Afana, S. Chamizo, A. Solé-Benet, and Y. Canton, "A new adaptive method to filter terrestrial laser scanner point clouds using morphological filters and spectral information to conserve surface microtopography," *ISPRS J. Photogramm. Remote Sens.*, vol. 117, pp. 141–148, July 2016.

[93] T. R. Cianciolo, J. S. Diamond, D. L. McLaughlin, R. A. Slesak, A. W. D'Amato, and B. J. Palik, "Hydrologic variability in black ash wetlands: Implications for vulnerability to emerald ash borer," *Hydrol. Process.*, vol. 35, p. e14014, Apr. 2021.

[94] C. Liao, H. Li, G. Lv, J. Tian, and Y. Xu, "Effects of ecological restoration on soil properties of the aeolian sandy land around Lhasa, southern Tibetan Plateau," *Ecosphere*, vol. 11, p. e03009, Jan. 2020.

[95] R. B. Rusu and S. Cousins, "3D is here: Point cloud library (PCL)," in *2011 IEEE International Conference on Robotics and Automation*, pp. 1–4, May 2011.

[96] W. Zhang, J. Qi, P. Wan, H. Wang, D. Xie, X. Wang, and G. Yan, "An Easy-to-Use airborne LiDAR data filtering method based on cloth simulation," *Remote Sensing*, vol. 8, p. 501, June 2016.

[97] M. Kalacska, G. L. Chmura, O. Lucanus, D. Bérubé, and J. P. Arroyo-Mora, "Structure from motion will revolutionize analyses of tidal wetland landscapes," *Remote Sens. Environ.*, vol. 199, pp. 14–24, Sept. 2017.

[98] L. F. Griffin, J. M. Knight, and P. E. R. Dale, "Identifying mosquito habitat microtopography in an australian mangrove forest using LiDAR derived elevation data," *Wetlands*, vol. 30, pp. 929–937, Oct. 2010.

[99] I. Korpela, R. Haapanen, A. Korrensalo, E. S. Tuittila, and T. Vesala, "Fine-resolution mapping of microforms of a boreal bog using aerial images and waveform-recording LiDAR," *Mires and Peat*, vol. 26, no. 03, pp. 2–25, 2020.

[100] K. Anderson, J. Bennie, and A. Wetherelt, "Laser scanning of fine scale pattern along a hydrological gradient in a peatland ecosystem," *Landsc. Ecol.*, vol. 25, pp. 477–492, Mar. 2010.

[101] X. Zhang, X. Meng, C. Li, N. Shang, J. Wang, Y. Xu, T. Wu, and C. Mugnier, "Micro-Topography mapping through terrestrial LiDAR in densely vegetated coastal environments," *ISPRS International Journal of Geo-Information*, vol. 10, p. 665, Oct. 2021.

[102] Y.-J. Wang, Q. Cheng-Zhi, and Z. A-Xing, "Review on algorithms of dealing with depressions in grid dem," *Annals of GIS*, vol. 25, no. 2, pp. 83–97, 2019.

[103] Q. Wu, C. R. Lane, L. Wang, M. K. Vanderhoof, J. R. Christensen, and H. Liu, "Efficient delineation of nested depression hierarchy in digital elevation models for hydrological analysis using level-set method," *J Am Water Resour Assoc.*, vol. 55, pp. 354–368, June 2019.

[104] L. Wang and H. Liu, "An efficient method for identifying and filling surface depressions in digital elevation models for hydrologic analysis and modelling," *Int. J. Geogr. Inf. Sci.*, vol. 20, pp. 193–213, Feb. 2006.

[105] Q. Wu and C. R. Lane, "Delineation and quantification of wetland depressions in the prairie pothole region of North Dakota," *Wetlands*, vol. 36, pp. 215–227, Apr. 2016.

[106] Q. Wu and C. R. Lane, "Delineating wetland catchments and modeling hydrologic connectivity using lidar data and aerial imagery," *Hydrol. Earth Syst. Sci.*, vol. 21, no. 7, pp. 3579–3595, 2017.

[107] X. Chu, J. Yang, Y. Chi, and J. Zhang, "Dynamic puddle delineation and modeling of puddle-to-puddle filling-spilling-merging-splitting overland flow processes," *Water Resources Research*, vol. 49, no. 6, pp. 3825–3829, 2013.

[108] C. J. Abolt, M. H. Young, A. L. Atchley, and C. J. Wilson, "Brief communication: Rapid machine-learning-based extraction and measurement of ice wedge polygons in high-resolution digital elevation models," *The Cryosphere*, vol. 13, no. 1, pp. 237–245, 2019.

[109] C. Witharana, M. A. E. Bhuiyan, A. K. Liljedahl, M. Kanevskiy, H. E. Epstein, B. M. Jones, R. Daanen, C. G. Griffin, K. Kent, and M. K. Ward Jones, "Understanding the synergies of deep learning and data fusion of multispectral and panchromatic high resolution commercial satellite imagery for automated ice-wedge polygon detection," *ISPRS Journal of Photogrammetry and Remote Sensing*, vol. 170, pp. 174–191, 2020.

[110] Y. LeCun, Y. Bengio, and G. Hinton, "Deep learning," *Nature*, vol. 521, pp. 436–444, May 2015.

[111] L. Huang, L. Liu, L. Jiang, and T. Zhang, "Automatic mapping of thermokarst landforms from remote sensing images using deep learning: A case study in the northeastern tibetan plateau," *Remote Sensing*, vol. 10, p. 2067, Dec. 2018.

[112] R. T. Brooks and M. Hayashi, "Depth-area-volume and hydroperiod relationships of ephemeral (vernal) forest pools in southern New England," *Wetlands*, vol. 22, pp. 247–255, June 2002.

[113] D. L. Gamble and W. J. Mitsch, "Hydroperiods of created and natural vernal pools in central Ohio: A comparison of depth and duration of inundation," *Wetlands Ecol. Manage.*, vol. 17, pp. 385–395, Aug. 2009.

[114] M. H. K. Hesselbarth, M. Sciaini, K. A. With, K. Wiegand, and J. Nowosad, "landscapemetrics : an open–source R tool to calculate landscape metrics," *Ecography*, vol. 42, pp. 1648–1657, Oct. 2019.

[115] R. G. Congalton, "A review of assessing the accuracy of classifications of remotely sensed data," *Remote Sensing of Environment*, vol. 37, no. 1, pp. 35–46, 1991.

[116] C. Liu, P. Frazier, and L. Kumar, "Comparative assessment of the measures of thematic classification accuracy," *Remote Sens. Environ.*, vol. 107, pp. 606–616, Apr. 2007.

[117] Cavallaro, N.; Shrestha, G.; Birdsey, R.; Mayes, M.A.; Najjar, R.G.; Reed, S.C.; Romero-Lankao, P,; Zhu Z., "Second state of the carbon cycle report (SOCCR2): A sustained assessment report," tech. rep., 2018.

[118] X. Shi, P. E. Thornton, D. M. Ricciuto, P. J. Hanson, J. Mao, S. D. Sebestyen, N. A. Griffiths, and G. Bisht, "Representing northern peatland microtopography and hydrology within the community land model," *Biogeosciences*, vol. 12, no. 21, pp. 6463–6477, 2015.

[119] J.-C. Padró, F.-J. Muñoz, J. Planas, and X. Pons, "Comparison of four UAV georeferencing methods for environmental monitoring purposes focusing on the combined use with airborne and satellite remote sensing platforms," *International Journal of Applied Earth Observation and Geoinformation*, vol. 75, pp. 130–140, 2019.

[120] M. Pinheiro, A. Reigber, R. Scheiber, P. Prats-Iraola, and A. Moreira, "Generation of highly accurate DEMs over flat areas by means of Dual-Frequency and Dual-Baseline airborne SAR interferometry," *IEEE Trans. Geosci. Remote Sens.*, vol. 56, pp. 4361–4390, Aug. 2018.

[121] C. Choi and D.-J. Kim, "Optimum baseline of a Single-Pass In-SAR system to generate the best DEM in tidal flats," *IEEE Journal of Selected Topics in Applied Earth Observations and Remote Sensing*, vol. 11, pp. 919–929, Mar. 2018.

[122] B. C. Budei, B. St-Onge, C. Hopkinson, and F.-A. Audet, "Identifying the genus or species of individual trees using a three-wavelength airborne lidar system," *Remote Sens. Environ.*, vol. 204, pp. 632–647, Jan. 2018.

[123] C. Hopkinson, L. Chasmer, C. Gynan, C. Mahoney, and M. Sitar, "Multisensor and multispectral LiDAR characterization and classification of a forest environment," *Can. J. Remote Sens.*, vol. 42, pp. 501–520, Sept. 2016.

[124] X. Yu, J. Hyyppä, P. Litkey, H. Kaartinen, M. Vastaranta, and M. Holopainen, "Single-sensor solution to tree species classification using multispectral airborne laser scanning," *Remote Sens. (Basel)*, vol. 9, p. 108, Jan. 2017.

[125] X. Li, C. Liu, Z. Wang, X. Xie, D. Li, and L. Xu, "Airborne LiDAR: state-of-the-art of system design, technology and application," *Meas. Sci. Technol.*, vol. 32, p. 032002, Dec. 2020.

[126] T. Panagou, E. Oikonomou, T. Hasiotis, and A. F. Velegrakis, "Shallow water bathymetry derived from green wavelength terrestrial laser scanner," *Mar. Geod.*, vol. 43, pp. 472–492, Sept. 2020.

[127] X. Guo, X. Yan, S. Zheng, H. Wang, and P. Yin, "Characteristics of high-resolution subaqueous micro-topography in the Jinshan deep trough and its im-

plications for riverbed deformation, Hangzhou Bay, China," *Estuarine, Coastal and Shelf Science*, vol. 250, p. 107147, 2021.

[128] J. Manyika, M. Chui, B. Brown, J. Bughin, R. Dobbs, C. Roxburgh, A. Hung Byers, and Others, *Big data: The next frontier for innovation, competition, and productivity.* McKinsey Global Institute, 2011.

[129] W. Tang and W. Shaowen, *High Performance Computing for Geospatial Applications.* Springer International Publishing, 2020.

[130] M. Zheng, W. Tang, Y. Lan, X. Zhao, M. Jia, C. Allan, and C. Trettin, "Parallel generation of very high resolution digital elevation models: High-Performance computing for big spatial data analysis," *Big Data in Engineering Applications*, pp. 21–39, 2018.

[131] R. Barnes, "Parallel Priority-Flood depression filling for trillion cell digital elevation models on desktops or clusters," *Comput. Geosci.*, vol. 96, pp. 56–68, Nov. 2016.

CHAPTER 2: Microtopography of low-relief coastal forested wetlands using LiDAR

2.1 Introduction

Microtopography, which is the small-scale variation of less than a meter in elevation, is common to low-relief coastal forested wetlands but rarely quantified (1). The spatial heterogeneity of the microtopographic features influences ecological functions such as carbon cycling (2), species distribution (3), hydrological functions (4), and soil processes (5). The importance of microtopography can be understood by the fact that microtopography is often added to the created wetlands to increase habitat diversity (6) and enhance biogeochemical cycling (7). Increasing urbanization and climate change have encouraged scientists to improve their understanding of microtopography and its impact on ecological functions in coastal wetland systems, particularly as related to carbon budgets (8). Sallenger et al. (9) showed that the rate of sea level rise is not spatially homogeneous with the increasing rate on the North American Atlantic coast. This makes freshwater tidal wetlands on the east coast especially vulnerable to seawater intrusion and an increase in hydroperiodicity. To understand the wetland structure and ecological functions in CFW systems it is essential to be able to quantify microtopography and understand the spatial pattern of microtopographic features which impacts the hydrological processes and biogeochemical cycling.

The microtopography of CFW is characterized by hollows and hummocks. Hollows are the low points that can become inundated during high tides and during periods of precipitation while hummocks are high points often exposed to air during regular tidal cycles. In low-relief coastal wetlands, the hummocks and hollows are often differentiated by only a few centimeters which require either labor-intensive manual surveying with a total station or Real Time Kinematic (RTK) Global Positioning Sys-

tem (GPS) systems or close-range remote sensing techniques to capture these small variations. Ground surveying is often based on establishing representative transects but it is questionable whether the transect-based approach can adequately represent the microtopographic features in a low-relief wetland, particularly over larger areas. In contrast, close-range remote sensing techniques such as small unmanned aerial systems (sUAS) and LiDAR can map the wetlands effectively and quantify microtopographic features precisely (10; 11; 12)

The mapping of microtopographic features depends on the optimal resolution of the digital elevation model (DEM). If a DEM is too coarse then the small microtopographic features may be missed due to the generalization of the terrain. However, a very high-resolution DEM may be more appropriate to delineate microtopographic features of sub-meter size. It is all the more significant when it comes to low-relief tidal forests topography where surface water and groundwater flow directions are largely determined by microtopographic features. The optimal DEM resolution, therefore, is required to achieve microtopographic accuracy and efficient data processing.

Close-range remote sensing technologies allow the generation of dense point cloud densities of three-dimensional topography and sub-meter resolution DEMs with high horizontal and vertical accuracy over a large area. However, a high-resolution DEM brings its own challenges in terms of data processing, data analysis, and data storage. Therefore, an optimal DEM resolution for modeling microtopography in complex natural ecosystems is needed to delineate microtopographic features efficiently. A few studies have characterized peatland microtopography using a terrestrial LiDAR (10; 12) and sUAS (13) by creating a high-resolution DEM of less than 1 m. Stovall et al. (12) used the elevation and slope to delineate hummocks by inverting the DEM. Moore et al. (13) used structure from motion (SfM) photogrammetry to generate their DEM and Gaussian mixed models to characterize hollows and hummocks while Graham et al. (10) classified microtopography using three methods: 1) using water

table depth data, 2) relative elevation, and 3) using elevation, concavity, and slope.

The characterization of microtopography is important to understand the hydrological, biogeochemical, and ecological functions of wetlands. The accurate characterization of microtopography in low-relief tidally influenced wetlands is needed to better estimate the impact of tidal fluctuations on carbon dynamics. Recently multiple studies ((14; 15; 16; 17) have performed comparative analyses of aerial and terrestrial LiDAR data and found mixed results. However, only a few studies to date compared aerial and terrestrial LiDAR focussing on microtopography-based studies. Therefore the objectives of this study are to 1) characterize and assess the microtopography of low-relief tidal forested wetlands using aerial and terrestrial LiDAR, and 2) to identify an optimal elevation threshold for widely available aerial LiDAR data to characterize microtopography in CFWs. For the first objective we focussed on (i) using aerial and terrestrial LiDAR data for the same study site and assessed the accuracy of the respective DEMs with respect to RTK GPS measurements, and (ii) characterized microtopography using the priority flood algorithm (18; 19). To achieve our second objective we proposed a new method of combining mean water level elevation and an optimum percentile elevation threshold to characterize microtopography. To accomplish these objectives we used terrestrial and aerial LiDAR point cloud data from tidal forested wetlands to derive high-resolution DEMs of the study site. We also provided a new user-friendly approach for terrestrial LiDAR microtopographic data acquisition and processing which will encourage its use in forested ecosystem studies.

2.2 Study Area

Our study site is a tidal freshwater forested wetland of Huger Creek watershed located in Santee Experimental Forest, within the Francis Marion National Forest, in South Carolina (Figures 2.1 and 2.2). Huger Creek is a fourth-order stream formed by the confluence of Nicholson Creek and Turkey Creek which later joins the east branch of Cooper River and eventually discharges into the Charleston harbor estuary. The study site consists of bottomland hardwood mixed deciduous forests with the study site experiencing an average 1.5 m daily tidal fluctuation (20). The data acquisition using terrestrial LiDAR was carried out in the second week of February 2022 during the leaf-off season to minimize occlusion. Photo Science Inc. acquired and processed the aerial LiDAR data in February 2007 with an average of 1-meter point spacing or better. This data can be accessed through http://cybergis.charlotte.edu/santee/views/data-landresource/lidar-data-table.php

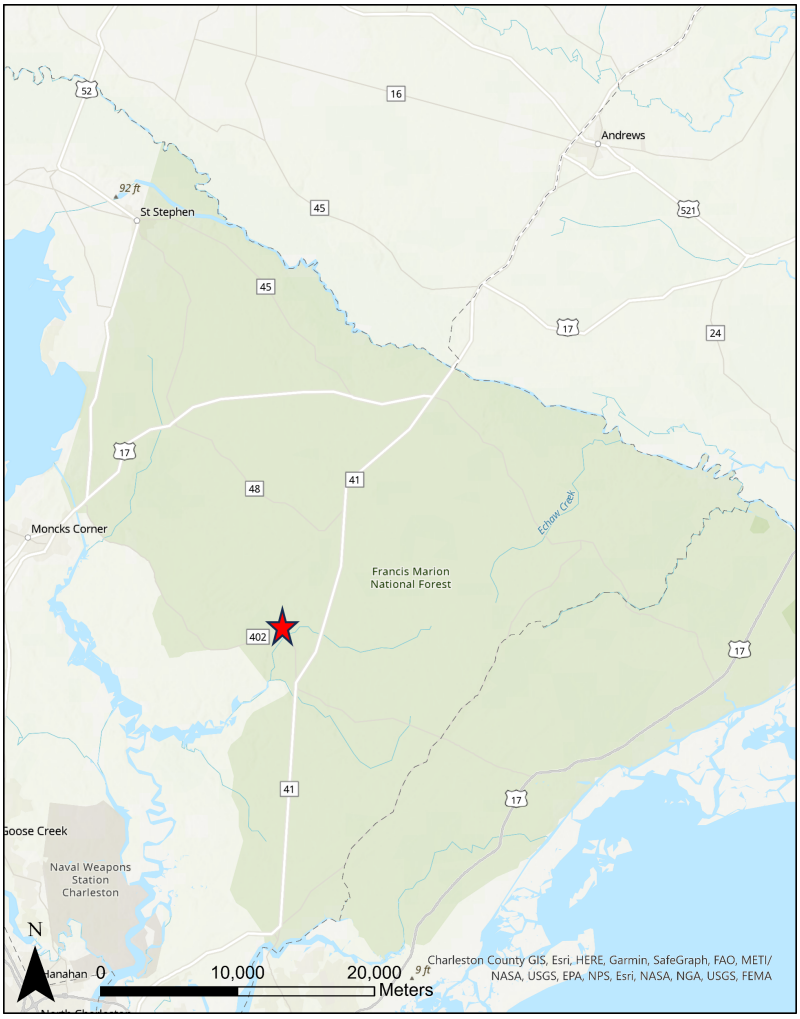

Figure 2.1: Tidal freshwater forested low-relief wetland located at Huger Creek in Santee Experimental Forest, SC USA.

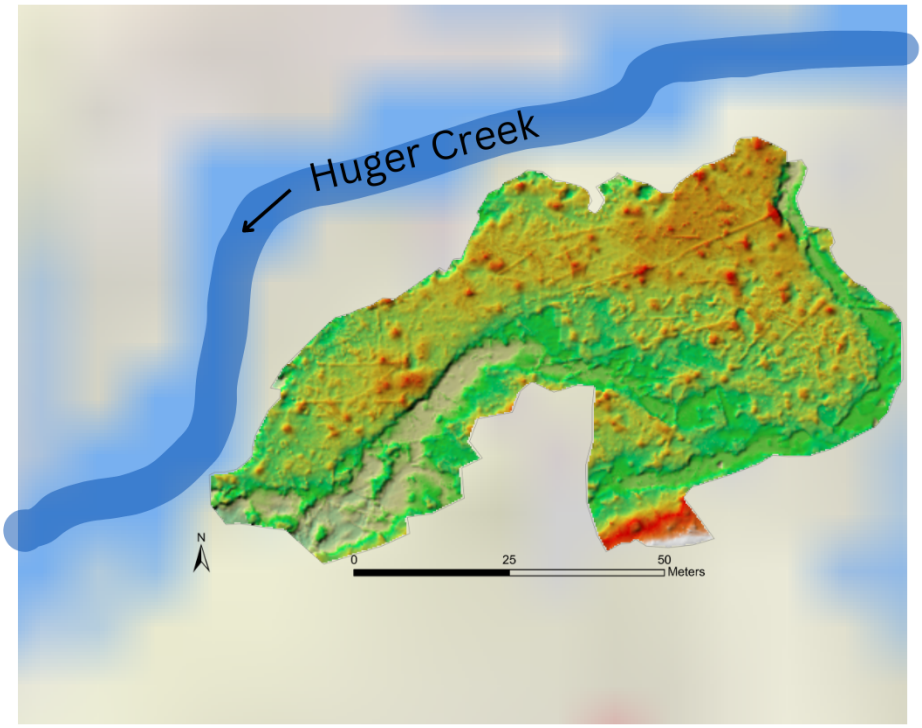

Figure 2.2: Shaded relief of the study site located at tidal freshwater Huger Creek

2.3 Method

We first evaluated how much of the study area needed to be scanned to compare the microtopographic variation in aerial and terrestrial LiDAR-based DEMs. We also selected a transect along the floodplain and measured surface elevation with RTK GPS. As per our review of previous studies (Table 2.1), we selected a plot size of 4330 m^2. Our study plot is fairly large compared to most of the previous studies summarized in Table 2.1. We selected a study area based on three factors: (i) undisturbed location or unmanaged forest location such that the aerial LiDAR (2007 data) and terrestrial LiDAR data (2022 data) can be compared; (ii) the availability of water-level data for multiple years recorded at 15-minute intervals; and (iii) to cover an area which includes a series of hollows which become inundated during regular diurnal tidal cycles and exposed to air during daily low tides.

Table 2.1: Microtopography study area considered by different studies using terrestrial LiDAR.

Study	Location	Plot Area (m^2)	Wetland/Forest Type	Reference
Vegetation pattern	Solway Plain, Cumbria, UK	700	Peatland bog	(21)
Vegetation pattern	Louisiana, USA	9,500	Restored wetland	(22)
Topsoil pH modeling	Alptal, Switzerland	20,000	Long-term Forest	(23)
Microtopography-hummocks characteristics	Northern Minnesota, USA	900	Forested Wetland	(24)
Microtopography- hummocks characterization	Northern Minnesota, USA	700 to 1200	Black ash wetlands	(12)
Microtopography characterization	Minnesota, USA	65	Spruce and Peatland Forest	(10)
Microtopography of alluvial fan	Tibet, China	10,000	Spruce and peatland forest	(25)

Tree biomass, soil chemistry	Minnesota, USA	700 to 1200	Black ash wetlands	(3)
Hydrologic variability	Minnesota, USA	300	Black ash wetlands	(26)
Microtopography and Carbon cycle	Marcell Experimental Forest, MN, USA	12	Ombrotrophic peat bog	(2)

2.3.1 Terrestrial LiDAR Acquisition

Terrestrial LiDAR data were collected utilizing a Faro Focus S 350 laser scanner with a monodyne laser of wavelength 1550 nm. This LiDAR device has a range of 0.6 m to 350 m depending on the terrain/study region with a ranging error of ±1mm and angular accuracy of 19 arcsec. The instrument is equipped with GPS, compass, height sensor, and dual-axis compensator. The data was collected in February 2022 during the leaf-off season when the forest floor is less obscured by overground vegetation allowing the microtopographical features to be observed. In addition, the hollows scan was performed during low tide to capture hollows that are open to the air and not inundated. For data collection, we chose a site in a low-relief tidal forested wetland with an average ground elevation of 1 m ASL. Previous researchers (23; 27) found that increasing the scan distance reduces the density of the ground point cloud. To ensure high ground point densities we maintained 10m of the distance between scan locations (see Figure 2.3). To scan the study site topography and avoid occlusion, we collected 108 overlapping scans at different locations. The terrestrial LiDAR point cloud was registered utilizing spherical reference targets used as tie points to stitch the scans together. To facilitate scan registration, we placed 5 to 8 spheres (targets) of 0.097 m radius in each plot. The scan position was selected so that at least four common targets were visible in two adjacent scans. Once the two scans were completed, we relocated two spheres to the next plot location while six remained in their original location. Faro SCENE software was used to coregister the individual scans utilizing the spherical targets.

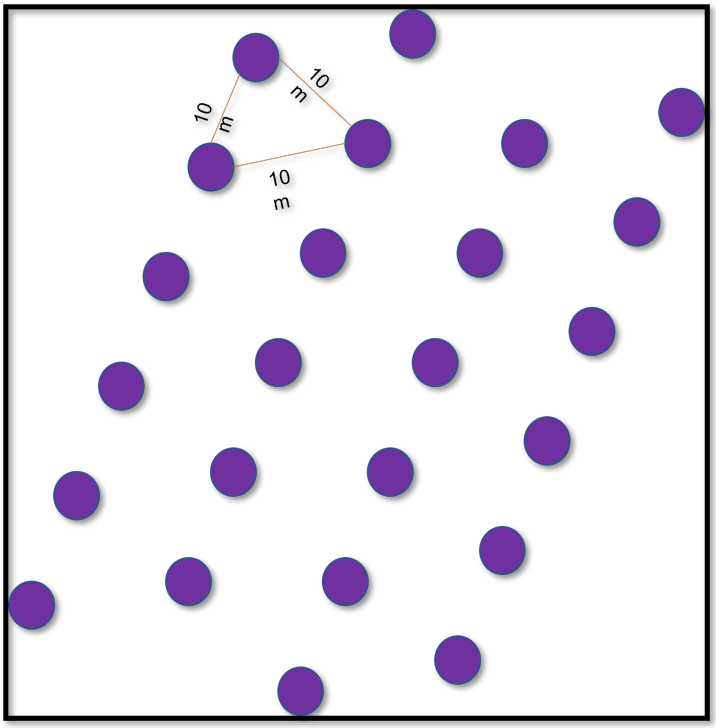

Figure 2.3: Scan configuration of forested wetlands using terrestrial LiDAR. The distance between each scan is 10m to ensure overlapping scans.

We also placed five Ground Control Points (GCPs) in four cardinals and one at the center of the plot for subsequent georeferencing. These GCPs were squared targets of dimension 0.372 m^2 placed directly on the ground. We made sure that these GCPs were visible in multiple scans. The center of the GCP was surveyed using a Trimble R12 RTK GPS with a precision of ± 5 mm.

2.3.2 Model Development

All LiDAR point clouds were processed with CloudCompare software and visualized using the R statistical programming language (packages: raster, rgdal, and sp) and ArcGIS Pro. We used a cloth simulation filter (CSF) (28) to extract ground points from the terrestrial LiDAR data. This technique simulates a cloth being placed over an upside-down terrain with the final shape of the cloth being the digital terrain model (DTM). The algorithm analyzed the cloth nodes and corresponding LiDAR

ground points to determine the ground points and non-ground points. A grid of 0.05 X 0.05 m was placed over the resultant point cloud and within each cell, the lowest height value was selected. The detailed framework is as shown in Figure 2.4).

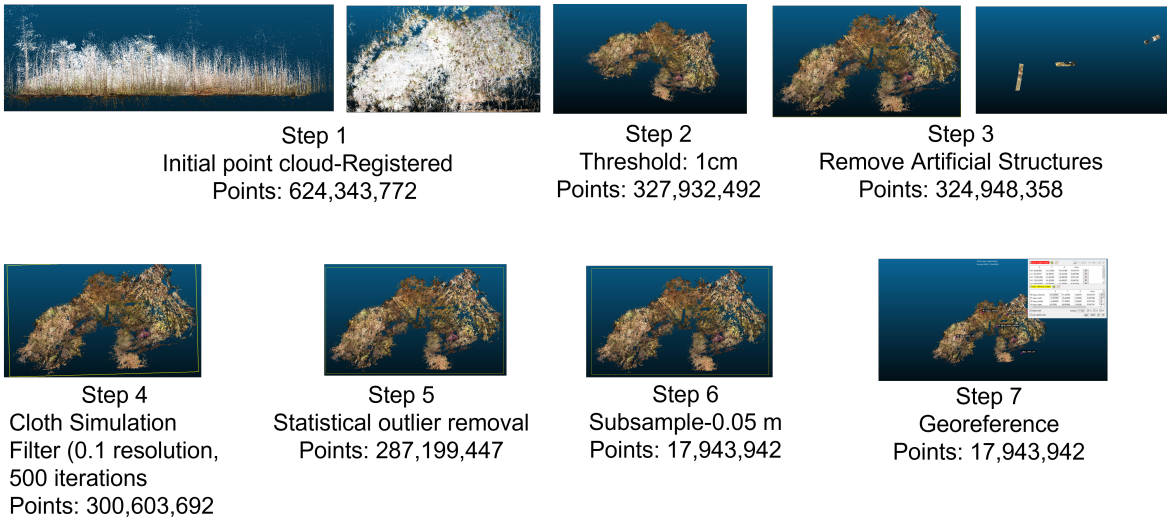

Figure 2.4: Ground points extracted from terrestrial LiDAR data using cloth simulation filters in CloudCompare.

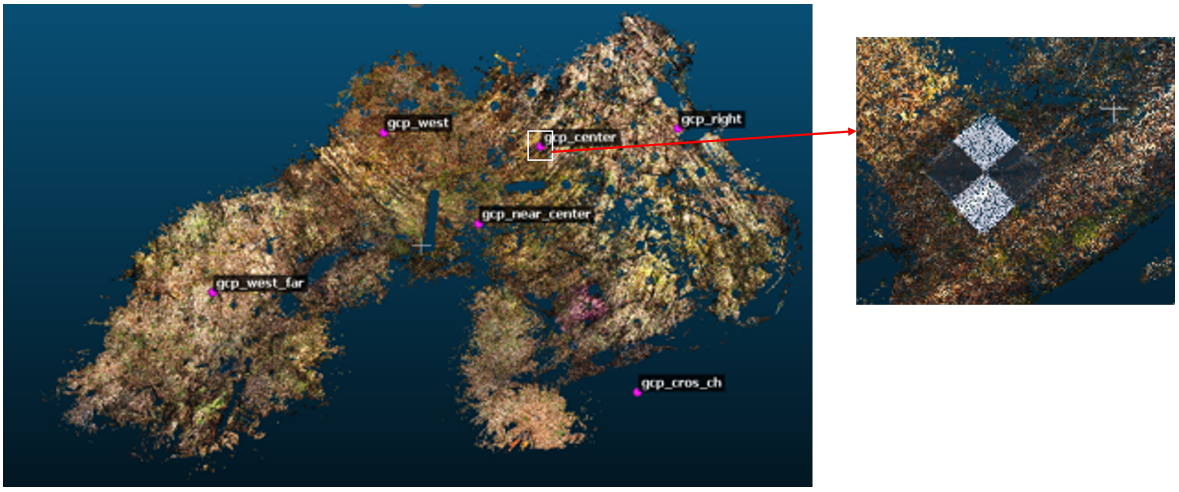

Figure 2.5: Georeferencing the resultant point cloud using 0.61 m X 0.61 m GCP (visible in inset) measured using RTK GPS

We utilized a new method to georeference the resultant point cloud. The point cloud was georeferenced using GCPs visible in the point cloud by carefully selecting

the center point of GCPs (see Figure 2.5. The elevation at the center of the GCP was measured using RTK GPS. The local coordinate system of the point cloud was then transformed to the GCPs coordinate system with the resulting georeferencing returning a Root Mean Square Error (rmse) of 0.0448 m. The georeferenced point cloud was then subsampled and then exported for further analysis. We selected an inverse distance weighted (IDW) method to generate a DEM from the aerial LiDAR and terrestrial LiDAR data. This method is most commonly used to generate DEM from LiDAR data and is considered to perform well (29). The IDW interpolation was carried out using ArcGIS Pro with a power of 2 and variable search radius of 12 points and a cell size of 0.25m for the terrestrial LiDAR and 1m for the aerial LiDAR. The ground points filtered from terrestrial LiDAR and bare ground points of the aerial LiDAR data were used for the interpolation and for generating the final DEM.

2.3.3 Water Level Measurements

The riparian water table elevations at the study site were measured using a Druc pressure transducer logged on a Cambell Scientific datalogger on a 15-minute time-step from 2019-2022. The highest and lowest water table each day for A) hollow, B) fringe, and C) hummock is shown in Figure 2.6.

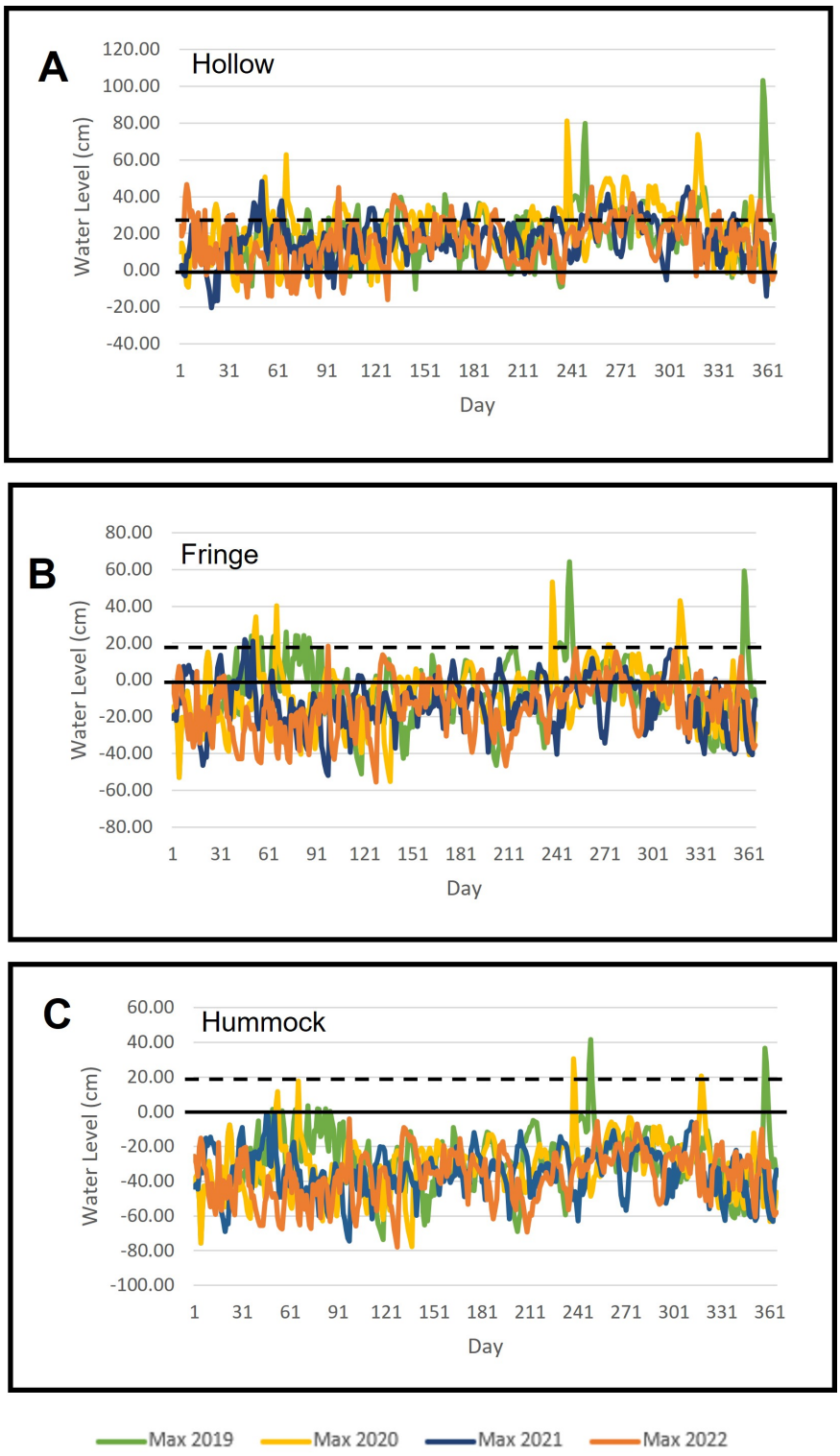

Figure 2.6: Maximum water level fluctuations from 2019-2022 in hollow, fringe, and hummock. The line at 0.00 indicates the ground surface level based on terrestrial LiDAR data while the dashed line is the ground surface level based on aerial LiDAR data.

2.3.4 Microtopography Classification

A common practice in the development of a DEM for the purpose of hydrological modeling is to remove surface depressions. These surface depressions are treated as spurious or artifacts (30). With close-range remote sensing where a DEM is often developed at 1 m or higher resolutions, small surface depressions can be delineated without treating them as artifacts. The most widely used algorithm, the priority flood algorithm (31) is a depression-filling algorithm. In this method, all the sinks in the DEM are filled and then the original DEM is subtracted from the filled DEM which results in a sink DEM. We can then estimate the size, volume, and depth of the sinks. Based on the data acquisition method and accuracy of the DEM, a threshold can be set to eliminate artifacts/spurious depressions and retain microtopographic features. Another method used to delineate microtopography is based on the water level. The elevation below the mean of the all-yearly median water level is classified as a hollow and above the elevation as a hummock (10).

$$M_{TLS} = \begin{cases} \text{Hollow}, & \text{if } z_{tls} \leq z_{wtls} \\ \text{Fringe}, & \text{if } z_{tls} > z_{wtls} \text{ and } z_{tls} \leq z_{50tls} \\ \text{Hummock}, & \text{if } z_{tls} > z_{50tls} \end{cases}$$

where M_{TLS} is characterized microtopography based on TLS-data, z_{tls} is point elevation and z_{wtls} is the four-year (2019-2022) maximum median water level. z_{50tls} is the elevation at 50th percentile in terrestrial LiDAR based DEM.

To delineate the microtopography derived from aerial LiDAR-based data, an elevation threshold was used, where any point above the threshold is classified as hummock and below were classified as hollow. Explicitly:

$$M_{ALS} = \begin{cases} \text{Hollow}, & \text{if } z_{als} \leq z_{29als} \\ \text{Fringe}, & \text{if } z_{als} > z_{29als} \text{ and } z_{als} \leq z_{50als} \\ \text{Hummock}, & \text{if } z_{als} > z_{50als} \end{cases}$$

where M_{ALS} is characterized microtopography based on aerial LiDAR data, z_{als} is the point elevation and z_{29als} is the elevation threshold which is found as 29th percentile. z_{50als} is the elevation at 50th percentile in aerial LiDAR based DEM.

2.4 Experimental Results

We conducted an experiment to evaluate aerial and terrestrial LiDAR data acquisition techniques for microtopographic feature delineation, focussing on CFW hollows. The terrestrial LiDAR data was collected on February 9, 2022, while aerial LiDAR data was collected on February 24, 2007. The terrestrial LiDAR initial point cloud consists of 624,343,772 points which were reduced to 287,199,447 points after applying a noise filter, statistical outlier removal filter, and cloth simulation filter (CSF). This point cloud was further subsampled such that the minimum space between points became 0.01 m. The remaining 17,943,942 points were georeferenced using four GCPs with an accuracy of 0.0448 m. The final georeferenced point cloud was then exported to create a DEM. The aerial LiDAR data was provided by USDA Forest Service, Santee Experimental Forest in XYZ ASCII format and can be accessed at http://cybergis.charlotte.edu/santee/views/data-landresource/lidar-data-table.php

2.4.1 Elevation Variation

The bare ground points were utilized to generate a fine-resolution DEM of the study area. The refined LiDAR-derived DEMs were produced with 0.25 m point density for terrestrial LiDAR-based data with an elevation range of 0.1 m to 2.6 m and 1 m point density for the aerial LiDAR-based data with an elevation range of 0.41 m to 2.5 m (See Figure 2.7)

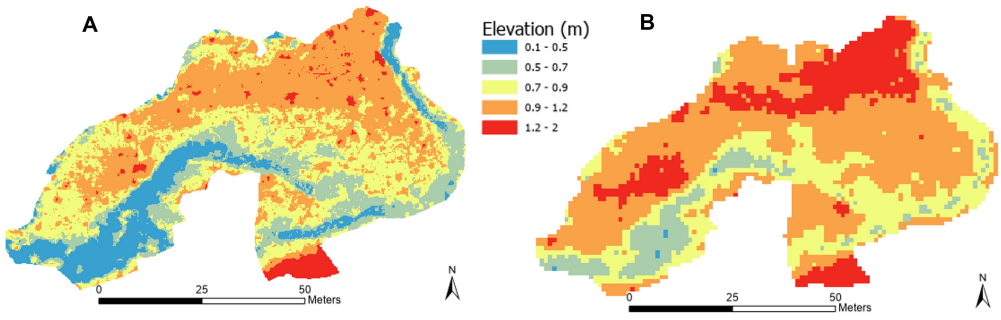

Figure 2.7: A) Terrestrial LiDAR-based DEM with a 0.25 m resolution B) Aerial LiDAR-based DEM with a 1 m resolution.

To evaluate the vertical accuracy of DEM, 26 points were measured with Trimble R-10 RTK GPS, and corresponding aerial LiDAR and terrestrial LiDAR DEM values were extracted. The RMSE value for aerial LiDAR DEM (1 m resolution) and terrestrial LiDAR DEM (0.25 m resolution) was 0.222 m and 0.107 m, respectively. To compare the elevations measured by terrestrial LiDAR and aerial LiDAR data along the transect of the flood plain a paired t-test was conducted which gave $p<0.01$ meaning the terrestrial LiDAR-based elevations are significantly different from the aerial LiDAR-based elevations.

2.4.2 Hollow Delineation

2.4.2.1 Priority Flood Algorithm

In the priority flood algorithm, the edge cells of the DEM are arranged in a priority queue where greater priority is assigned to lower elevations. To delineate microtopographic depressions in the study areas we set two parameters, which include a minimum depression size, and a minimum depression depth. For terrestrial LiDAR data, the depressions were delineated with criteria of a depression size of 0.25 m and a minimum depression depth of 0.1m while for aerial LiDAR DEM, a depression size of 1m and a depression depth of 0.1m was considered. These parameters were selected based on the fact that microtopographic features can be $1m^2$ or less and in low-relief topography, the hollows and hummock elevation only vary by a few 10's centimeters. The hollow delineation using the priority flood algorithm resulted in 75 and 13 depressions in terrestrial and aerial LiDAR data, respectively (Figure 2.8). From our field experience and knowledge, we know a series of hollows at the south end of the study area. We expected a continuous series of hollows rather than a discrete delineation.

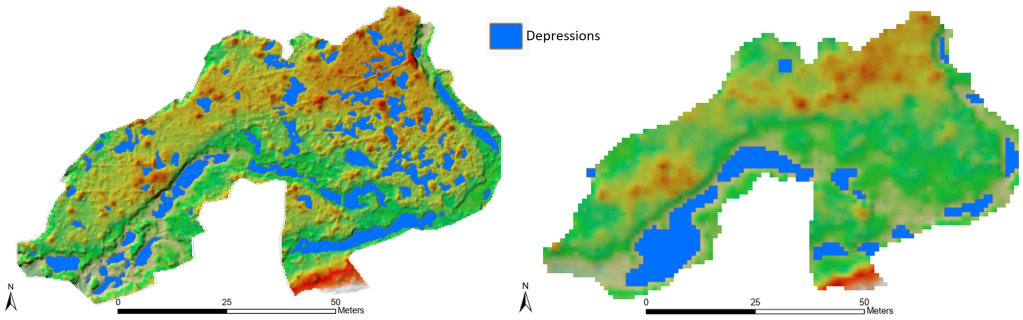

Figure 2.8: Depression delineation A) terrestrial LiDAR data of 0.25 m resolution and B) aerial LiDAR data of 1m resolution. The depressions are shown above the shaded relief.

The terrestrial LiDAR we used for data acquisition has a wavelength of 1550 nm, which is near-infrared. It failed to capture an adequate density of the point cloud in hollows elevation as the wavelength was absorbed rather than reflected at the study site. Even though terrestrial LiDAR-based data has delineated a significant number of hollows, the continuity of the tidal channel can not be seen due to a lack of adequate data and limitations of the instrument used. On the other hand, for the aerial LiDAR-based data, we suspected that owing to the "edge effect" all the hollows were not delineated. The priority flood algorithm delineates depressions based on the flow network and depression size. The model's boundary may have impacted the result of the algorithm as it excludes the network structure and events happening beyond the boundary. To validate it, we increased the boundary and included an area within the floodplain which resulted in the successful delineation of a series of hollows at the study site using the aerial LiDAR data (see Figure 2.9).

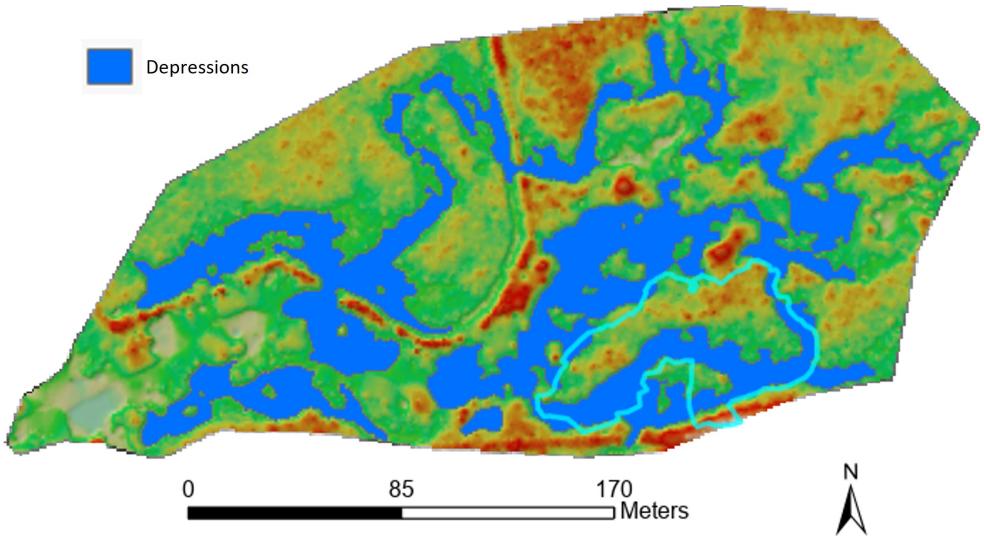

Figure 2.9: Depression delineation using the priority flood algorithm based on aerial LiDAR data with a minimum sink size of 1 m^2 and minimum sink depth of 0.5 m. The blue line shows the boundary of the study site.

2.4.2.2 Combining water level and elevation threshold

The daily mean maximum water level from 2019-2022 was selected as a threshold to characterize microtopography. The mean daily maximum water level is calculated as 0.68 m. The terrestrial LiDAR data shows that the landscape below 0.68 m A.S.L. is hollow. We found that the 29th percentile of elevation values are characterized as hollows as they were below 0.68 m. We then used the 29th percentile as the threshold to delineate depressions in the aerial LiDAR-based data. The corresponding 29th percentile of elevation in the aerial LiDAR data was found to be 0.87 m. This method has accurately delineated the series of hollows (see Figure 2.11), which becomes a temporary channel during high tide and is exposed to air during low tide.

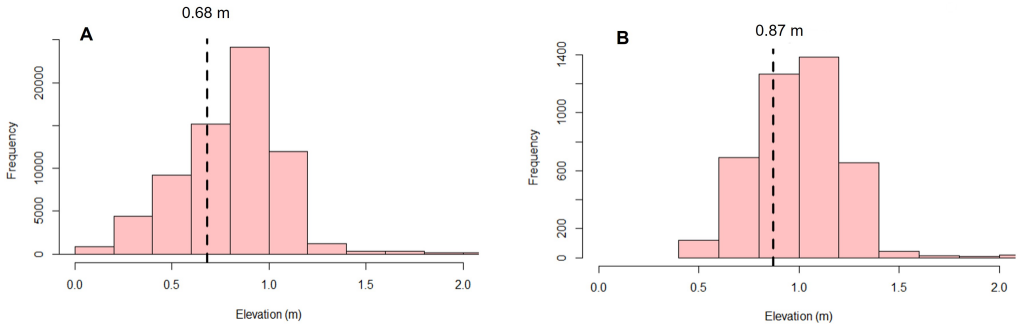

Figure 2.10: Elevation distribution of LiDAR-based DEM where the vertical line shows the threshold elevation. A) Elevation distribution of terrestrial LiDAR-based DEM of 0.25 m resolution. Vertical lines show the threshold of 0.68 m, which is selected based on the maximum mean water level. B) Elevation distribution of aerial LiDAR-based DEM of 1.00 m resolution. Vertical lines show the threshold of 0.87 m, the 29th percentile of the elevation values.

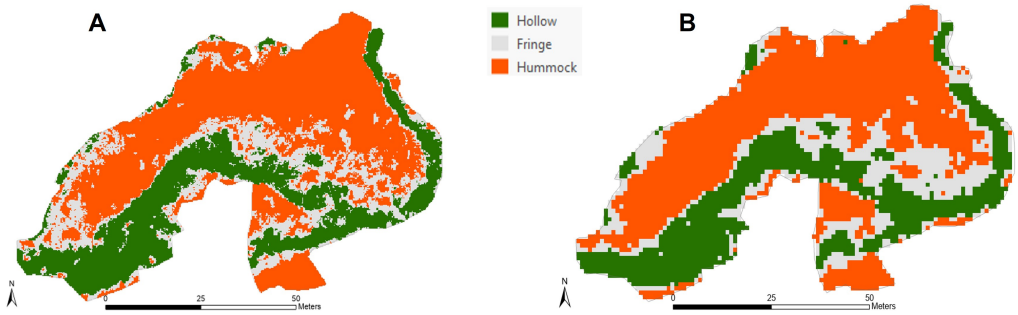

Figure 2.11: Microtopography classification based on the mean daily water level and elevation threshold. A) Microtopography classification in terrestrial LiDAR-based DEM with hollow, fringe, and hummock covering an area of 28.7%, 21.7%, and 49.6% respectively. B) Microtopography classification in aerial LiDAR-based DEM with hollow, fringe, and hummock covering an area of 30.6%, 18.4%, and 51.0% respectively.

Our method has successfully refined the delineation of hollows for the study site using aerial LiDAR data by utilizing an elevation threshold and the record of water level elevation for the site. We further scaled our results over a larger area which included a larger area of the Huger Ck.flood plain of 50,000 m^2. We utilized the same methodology and identified the 29th percentile of the elevation in the region which came out as 0.903 m. We used this elevation threshold to characterize microtopography over a larger area as shown in Figure 2.12.

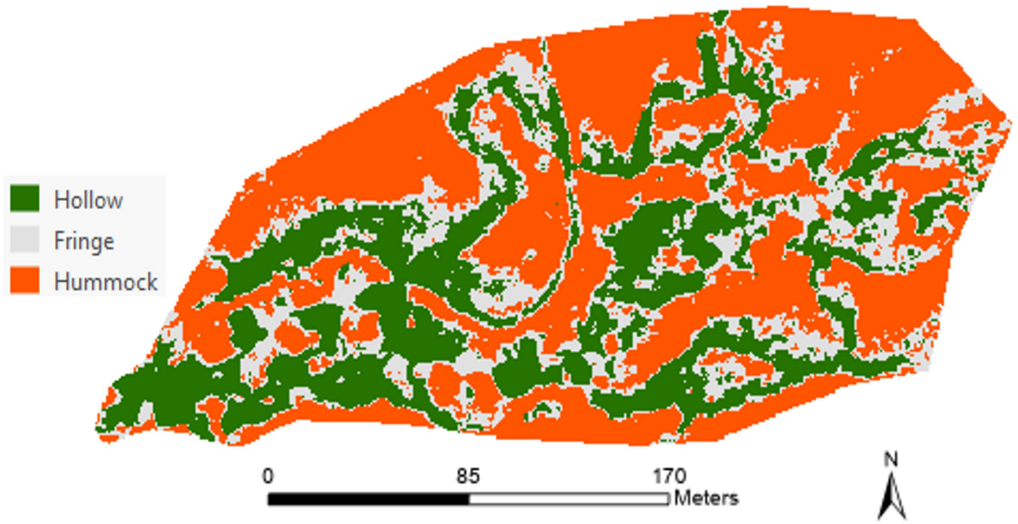

Figure 2.12: Microtopography delineation over a larger scale using an elevation threshold. Hollows are delineated at the 29th percentile of the elevation distribution covering 39% of the total area.

By combining the historical water level data in conjunction with a subset of more detailed terrestrial LiDAR data we found more accurate results as compared to applying the widely used priority flood algorithms and airborne LiDAR alone in the delineation of CFW hollows. The reason is elevation thresholding is independent of the flow network. Therefore, there is no edge effect, which results in the delineation of hollows at the edges, which the former algorithm misses.

2.5 Discussion

Our study site shows a unimodal elevation distribution similar to that of (Graham et al., 2020) and resembles a normal distribution. However, our plot size was more extensive than that examined by (Graham et al., 2020; Moore et al., 2019a). Here we provide a unique method of combining water level data and elevation threshold to characterize microtopography in the CFW environment. In this method, the terrestrial LiDAR data is used as a reference. The optimal threshold value of elevation is identified based on the mean daily maximum water level. Then the corresponding percentile of elevation is used as a threshold for aerial LiDAR data. Our results show how terrestrial LiDAR data derived from a small area can be combined with water level data and then scaled to a larger area utilizing coarser resolution aerial LiDAR data to delineate wetland hollows. Our method utilizes labor-intensive field data such as terrestrial LiDAR survey data from a relatively small area and coarse-resolution aerial LiDAR data to accurately characterize wetland microtopography over relatively large areas.

In addition, multiple overlapping scans ensured the coverage of the study area with evenly distributed point clouds ensuring the quality of DEM. The CSF filter was also found to distinguish ground points from non-ground points in the forested wetland effectively. Our method of placing GCPs on the ground and ensuring they are visible in some scans also worked well regarding georeferencing. The accuracy that of both TLS and ALS DEM is high, even in this complex, low-relief forested topography. For 0.25 m resolution, our accuracy of 0.107 m was comparable with (23) reported RMSE of 0.12 to 0.14 m for the TLS DEM. We also agree with Baltensweiler et al. and Stovall et al.(23; 12) that it is necessary to collect multiple overlapping scans to ensure high accuracy of the resulting DEM.

2.6 Conclusion

Close-range remote sensing techniques such as terrestrial and aerial LiDAR can be used to characterize the microtopography of complex low-relief forested wetland terrains. Even though the accuracy of terrestrial LiDAR-derived DEM is high, the data collection process can be time-consuming, requiring multiple overlapping scans to cover the study site. Our results revealed that by combining mean daily maximum water levels and elevation threshold, we can sufficiently delineate the hollows utilizing more widely available lower point density aerial LiDAR data. Microtopography is vital to wetlands' ecological, biogeochemical, and hydrological functions. To understand different ecosystem functions, it is important to accurately characterize the distribution and extent of different microtopographic features. Here we proposed a method of utilizing high-resolution terrestrial LiDAR and water-level data to identify a threshold for coarser-resolution aerial LiDAR data. Our method provides a robust tool to characterize microtopography in low-relief tidal forested wetlands. This reduces the need to collect labor-intensive terrestrial LiDAR data over a large area, which can be problematic over large portions of the year due to vegetation. With our method, an aerial LiDAR DEM of 1 m resolution is appropriate for microtopographic mapping in this low-relief CFW environment. In addition, bathymetric LiDAR or terrestrial LiDAR with a green light is more suitable for mapping the depressions-dominated landscape which tends to be saturated during high tides or high water conditions.

2.7 References

[1] S. Karstens, G. Jurasinski, S. Glatzel, and U. Buczko, "Dynamics of surface elevation and microtopography in different zones of a coastal phragmites wetland," *Ecol. Eng.*, vol. 94, pp. 152–163, Sept. 2016.

[2] J. D. Graham, D. M. Ricciuto, N. F. Glenn, and P. J. Hanson, "Incorporating microtopography in a land surface model and quantifying the effect on the carbon cycle," *J. Adv. Model. Earth Syst.*, vol. 14, Feb. 2022.

[3] J. S. Diamond, D. L. Mclaughlin, R. A. Slesak, and A. Stovall, "Microtopography is a fundamental organizing structure of vegetation and soil chemistry in black ash wetlands," *Biogeosciences*, vol. 17, no. 4, pp. 901–915, 2020.

[4] C. R. Lane, S. G. Leibowitz, B. C. Autrey, S. D. LeDuc, and L. C. Alexander, "Hydrological, physical, and chemical functions and connectivity of non-floodplain wetlands to downstream waters: A review," *J. Am. Water Resour. Assoc.*, vol. 54, pp. 346–371, Mar. 2018.

[5] E. Rodríguez-Caballero, Y. Cantón, S. Chamizo, R. Lázaro, and A. Escudero, "Soil loss and runoff in semiarid ecosystems: A complex interaction between biological soil crusts, micro-topography, and hydrological drivers," *Ecosystems*, vol. 16, pp. 529–546, June 2013.

[6] E. T. Ott, J. M. Galbraith, W. L. Daniels, and W. M. Aust, "Effects of amendments and microtopography on created tidal freshwater wetland soil morphology and carbon," *Soil Sci. Soc. Am. J.*, vol. 84, pp. 638–652, Mar. 2020.

[7] K. L. Wolf, C. Ahn, and G. B. Noe, "Microtopography enhances nitrogen cycling and removal in created mitigation wetlands," *Ecol. Eng.*, vol. 37, pp. 1398–1406, Sept. 2011.

[8] K. J. Minick, B. Mitra, X. Li, M. Fischer, M. Aguilos, P. Prajapati, A. Noormets, and J. S. King, "Wetland microtopography alters response of potential net CO_2 and CH_4 production to temperature and moisture: Evidence from a laboratory experiment," *Geoderma*, vol. 402, p. 115367, Nov. 2021.

[9] A. H. Sallenger, K. S. Doran, and P. A. Howd, "Hotspot of accelerated sea-level rise on the atlantic coast of north america," *Nat. Clim. Chang.*, vol. 2, pp. 884–888, June 2012.

[10] J. D. Graham, N. F. Glenn, L. P. Spaete, and P. J. Hanson, "Characterizing peatland microtopography using gradient and Microform-Based approaches," *Ecosystems*, pp. 1–17, 2020.

[11] M. Kalacska, J. P. Arroyo-Mora, and O. Lucanus, "Comparing UAS LiDAR and Structure-from-Motion photogrammetry for peatland mapping and virtual reality (VR) visualization," *Drones*, vol. 5, p. 36, May 2021.

[12] A. E. L. Stovall, J. S. Diamond, R. A. Slesak, D. L. McLaughlin, and H. Shugart, "Quantifying wetland microtopography with terrestrial laser scanning," *Remote Sens. Environ.*, vol. 232, p. 111271, 2019.

[13] P. A. Moore, M. C. Lukenbach, D. K. Thompson, N. Kettridge, G. Granath, and J. M. Waddington, "Assessing the peatland hummock–hollow classification framework using high-resolution elevation models: implications for appropriate complexity ecosystem modeling," *Biogeosciences*, vol. 16, pp. 3491–3506, Sept. 2019.

[14] W. R. Currier, J. Pflug, G. Mazzotti, T. Jonas, J. S. Deems, K. J. Bormann, T. H. Painter, C. A. Hiemstra, A. Gelvin, Z. Uhlmann, L. Spaete, N. F. Glenn, and J. D. Lundquist, "Comparing aerial lidar observations with terrestrial lidar

and snowâprobe transects from NASA's 2017 SnowEx campaign," *Water Resour. Res.*, vol. 55, pp. 6285–6294, July 2019.

[15] M. Khanal, M. Hasan, N. Sterbentz, R. Johnson, and J. Weatherly, "Accuracy comparison of aerial lidar, Mobile-Terrestrial lidar, and UAV photogrammetric capture data elevations over different terrain types," *Infrastructures*, vol. 5, p. 65, July 2020.

[16] E. LaRue, F. Wagner, S. Fei, J. Atkins, R. Fahey, C. Gough, and B. Hardiman, "Compatibility of aerial and terrestrial LiDAR for quantifying forest structural diversity," 2020.

[17] J. Murgoitio, R. Shrestha, N. Glenn, and L. Spaete, "Airborne LiDAR and terrestrial laser scanning derived vegetation obstruction factors for visibility models," *Trans. GIS*, vol. 18, pp. 147–160, Feb. 2014.

[18] R. Barnes, "Parallel Priority-Flood depression filling for trillion cell digital elevation models on desktops or clusters," *Comput. Geosci.*, vol. 96, pp. 56–68, Nov. 2016.

[19] Q. Wu, C. R. Lane, L. Wang, M. K. Vanderhoof, J. R. Christensen, and H. Liu, "Efficient delineation of nested depression hierarchy in digital elevation models for hydrological analysis using level-set method," *J Am Water Resour Assoc.*, vol. 55, pp. 354–368, June 2019.

[20] Trettin, Czwartacki, Allan, and others, "Linking freshwater tidal hydrology to carbon cycling in bottomland hardwood wetlands," *In: Stringer, Christina E.; Krauss, Ken W.; Latimer, James S., eds Headwaters to estuaries: advances in watershed science and management-Proceedings of the Fifth Interagency Conference on Research in the Watersheds. March 2-5, 2015, North Charleston, South*

Carolina. e-General Technical Report SRS-211. Asheville, NC: US Department of Agriculture Forest Service, Southern Research Station., p. 302, 2016.

[21] K. Anderson, J. Bennie, and A. Wetherelt, "Laser scanning of fine scale pattern along a hydrological gradient in a peatland ecosystem," *Landsc. Ecol.*, vol. 25, pp. 477–492, Mar. 2010.

[22] X. Zhang, X. Meng, C. Li, N. Shang, J. Wang, Y. Xu, T. Wu, and C. Mugnier, "Micro-Topography mapping through terrestrial LiDAR in densely vegetated coastal environments," *ISPRS International Journal of Geo-Information*, vol. 10, p. 665, Oct. 2021.

[23] A. Baltensweiler, L. Walthert, C. Ginzler, F. Sutter, R. S. Purves, and M. Hanewinkel, "Terrestrial laser scanning improves digital elevation models and topsoil pH modelling in regions with complex topography and dense vegetation," *Environmental Modelling & Software*, vol. 95, pp. 13–21, Sept. 2017.

[24] J. S. Diamond, D. L. McLaughlin, R. A. Slesak, and A. Stovall, "Pattern and structure of microtopography implies autogenic origins in forested wetlands," *Hydrol. Earth Syst. Sci.*, vol. 23, pp. 5069–5088, Dec. 2019.

[25] C. Liao, H. Li, G. Lv, J. Tian, and Y. Xu, "Effects of ecological restoration on soil properties of the aeolian sandy land around Lhasa, southern Tibetan Plateau," *Ecosphere*, vol. 11, Jan. 2020.

[26] T. R. Cianciolo, J. S. Diamond, D. L. McLaughlin, R. A. Slesak, A. W. D'Amato, and B. J. Palik, "Hydrologic variability in black ash wetlands: Implications for vulnerability to emerald ash borer," *Hydrol. Process.*, vol. 35, Apr. 2021.

[27] E. Puttonen, T. Hakala, O. Nevalainen, S. Kaasalainen, A. Krooks, M. Karjalainen, and K. Anttila, "Artificial target detection with a hyperspectral LiDAR over 26-h measurement," *Organ. Ethic.*, vol. 54, p. 013105, Jan. 2015.

[28] W. Zhang, J. Qi, P. Wan, H. Wang, D. Xie, X. Wang, and G. Yan, "An Easy-to-Use airborne LiDAR data filtering method based on cloth simulation," *Remote Sensing*, vol. 8, p. 501, June 2016.

[29] M. Zheng, W. Tang, Y. Lan, X. Zhao, M. Jia, C. Allan, and C. Trettin, "Parallel generation of very high resolution digital elevation models: High-Performance computing for big spatial data analysis," in *Big Data in Engineering Applications* (S. S. Roy, P. Samui, R. Deo, and S. Ntalampiras, eds.), pp. 21–39, Singapore: Springer Singapore, 2018.

[30] Q. Wu and C. R. Lane, "Delineating wetland catchments and modeling hydrologic connectivity using lidar data and aerial imagery," *Hydrol. Earth Syst. Sci.*, vol. 21, no. 7, pp. 3579–3595, 2017.

[31] L. Wang and H. Liu, "An efficient method for identifying and filling surface depressions in digital elevation models for hydrologic analysis and modelling," *Int. J. Geogr. Inf. Sci.*, vol. 20, pp. 193–213, Feb. 2006.

CHAPTER 3: Quantifying the impact of LiDAR-based microtopography and tidal variations on greenhouse gas dynamics in freshwater coastal forested wetlands

3.1 Introduction

Wetlands are hotspots for biogeochemical transformations and biotic diversity in most ecosystems. They play a key role in the global carbon cycle with global methane (CH_4) emissions ranging from 127 to 227 Tg CH_4 per year. This is the highest global natural source of CH_4 to the atmosphere (1). These significant biogenic sources of methane emissions contribute up to 40% to 50% of global methane emissions (2). A study based on 21 wetlands from all over the world by Mitsch et al. (3) estimated that the world's wetlands sequestered 1280 Tg-C/yr of CO_2 from the atmosphere, and 448 Tg-C/yr is emitted as CH_4 emissions which indicates the world's wetland serves as net sinks with total carbon retention of 832 Tg-C/yr. Emphasizing the importance of coastal environments in the global C cycle (4) estimated a total flux of 94 Tg-C/yr in their study of sea-to-air fluxes of CO_2 in the world's estuaries. Cavallaro et al. (1) estimate the CO_2 outgassing from North American estuarine environments as 10 Tg C/year.

The tidal freshwater wetlands and marshes in the South Atlantic region have the highest wetland density of the entire east coast of the USA (5; 6). In South Carolina, historically tidal freshwater wetlands (TFW) were often diked and converted into rice fields, although efforts are now being made to convert them to their original conditions (7). Numerous researchers have pointed out that coastal wetlands face the combined issues of increasing urbanization and sea level rise (8; 9), leading to wetland loss due to changing habitat and saltwater intrusion. Saltwater intrusion can significantly alter wetland biogeochemical cycles. For instance, saltwater intrusion reduces den-

itrification and changes microbial community composition (10). Even though there are numerous biogeochemical studies on coastal wetlands, relatively few have examined tidal freshwater forested wetlands (TFFW), (11). In the US, TFFW is widely distributed over the southeastern coastal region and generally located in the upper intertidal reaches of coastal rivers and their tributaries. In TFFWs microtopography affects the surface inundation, water table depth, soil respiration, vegetation and microbial community compositions, and other biogeochemical processes. However, very little information is available on the influence of microtopography and its interaction with tidal hydrology on C gas fluxes in coastal forested wetlands. Quantification of C emissions and C sequestration with respect to microtopography will not only enhance our knowledge of the soil C pool associated with wetlands but also assist us in designing management strategies to prevent further wetland degradation and protect the ecosystem services provided by these coastal wetland systems.

The microtopography of wetlands has been found to significantly influence the spatial distribution of wetland CH_4 emissions, with significantly higher emissions occurring from hollows than hummocks (12; 13; 14). Based on hollows' drying and wetting cycle, the anaerobic soil volumetric fraction increases or decreases as driven by reduction-oxidation reactions. Li et al. (15) labeled this as an "anaerobic balloon" which swells or shrinks over time in response to hydrologic variability. Aerobic and anaerobic microsites exist simultaneously in close proximity in both wetland and forest soils. During high tides in coastal freshwater wetlands, the hollows are repeatedly inundated and become saturated creating a reducing environment and leading to anaerobic conditions favoring methylation. During low tides, hollows might only partially drain leaving hollow soils near saturation throughout the year. Whereas, saturated conditions in hollow soils in forested wetlands upstream of the tidal influence are determined by the frequency and magnitude of precipitation events balanced by evapotranspiration demands. This can result in hollow soils drying out and aerobic

soil conditions for extended periods, particularly during the growing season. Therefore, incorporating microtopography and its interaction with site-specific hydrologic conditions is critical in the accurate modeling of C gas flux measurements. However, in the low-relief coastal environment, this requires fine-scale measurements of the study site which becomes challenging when the study site is remote and forested. Remote sensing techniques combined with representative field measurements can provide a possible solution to this problem. Several recent studies have reported the use of remote sensing technologies to map the microtopography of wetlands (16; 17; 18). These have included Unmanned Aerial Systems (UAS) based on structure from motion (SfM) photogrammetry, airborne LiDAR, and terrestrial laser scanners (TLS).

This chapter aims to assess the sensitivity of C gas emissions to TFFW microtopography represented by Digital Elevation Models (DEMs) with different spatial resolutions and availability. Specifically, we develop DEMs of a TFFW from aerial and terrestrial LiDAR measurements and incorporate them into a spatially explicit and process-based biogeochemical model to quantify soil CH_4 and CO_2 fluxes in tidal wetlands. A second objective of the study is to examine the interaction between wetland microtopography and tidal hydrology and its importance in GHG production in coastal wetlands.

This study uses the recently developed biogeochemical model Tidal Freshwater Wetlands-Denitrification Decomposition (TFW-DNDC) (19) to estimate Greenhouse Gas (GHG) emissions in a low-relief tidally influenced wetland characterized by a complex microtopography. The TFW-DNDC model is a process-based model developed in cooperation with researchers at the USDA Center for Forested Wetlands Research, the U.S. Geological Survey Wetland and Aquatic Research Center, and the School of Forest Resources and Environmental Science, Michigan Technological University. The model can simulate GHG dynamics in TFFW ecosystems and is modified from the mangrove-based version of the DNDC model (mangrove carbon assessment tool

(MCAT) (20). MCAT-DNDC was developed by integrating Forest-DNDC (21) and Wetland-DNDC (22) to consider freshwater wetland biogeochemistry, water levels, vegetation, and soil characteristics. The model can simulate carbon dynamics in the mangroves in terms of climate change, natural or anthropogenic disturbances, and sea level rise. In addition to MCAT DNDC capabilities, the revised TFW-DNDC includes a salinity level feature in the model and can predict the impact of seawater intrusion. In addition, it also considers daily maximum and minimum water levels in the model which can more accurately depict the GHG dynamics in tidal regions.

Several researchers have used these DNDC models to simulate carbon sequestration and trace gas emissions in different types of forests. Shu et al. (23) analyzed soil GHG fluxes in a temperate forest, Changbai mountain pine forest in China, using an automatic multi-channel soil CO_2, CH_4, and N_2O flux observation system to measure GHG fluxes directly. They then used Forest-DNDC to simulate the continuous high-frequency soil GHG flux data. The study claimed that Forest-DNDC provided an unbiased estimate of the annual average soil CH_4 flux while underestimating average CO_2 and N_2O fluxes. Dai et al. (24) assessed C sequestration in a temperate forest in Idaho, US using Forest DNDC. Kurbatova et al. (25) conducted a sensitivity test using Forest-DNDC simulations by varying the water table and concluded that climate change could significantly affect the C balance in wetland forests and could convert them from sinks to a source of atmospheric CO_2 and considers salinity and tidal fluctuation in water level, in addition to soil, vegetation, and climate parameters. Wang et al. (19) developed TFW-DNDC to study the impact of salinity on plant productivity and soil carbon sequestration in TFFW. The study showed that increased salinity significantly reduced carbon sequestration under drought conditions. The TFW-DNDC model is spatially explicit and can utilize different digital elevation models with variable spatial resolutions to represent a site's microtopography. Five components drive the TFW-DNDC model: 1) climate factors, 2) soil parameters,

3) vegetation properties, 4) anthropogenic activities, and 5) hydrology. The TFW-DNDC model's structure used in our study is shown in Figure 3.1.

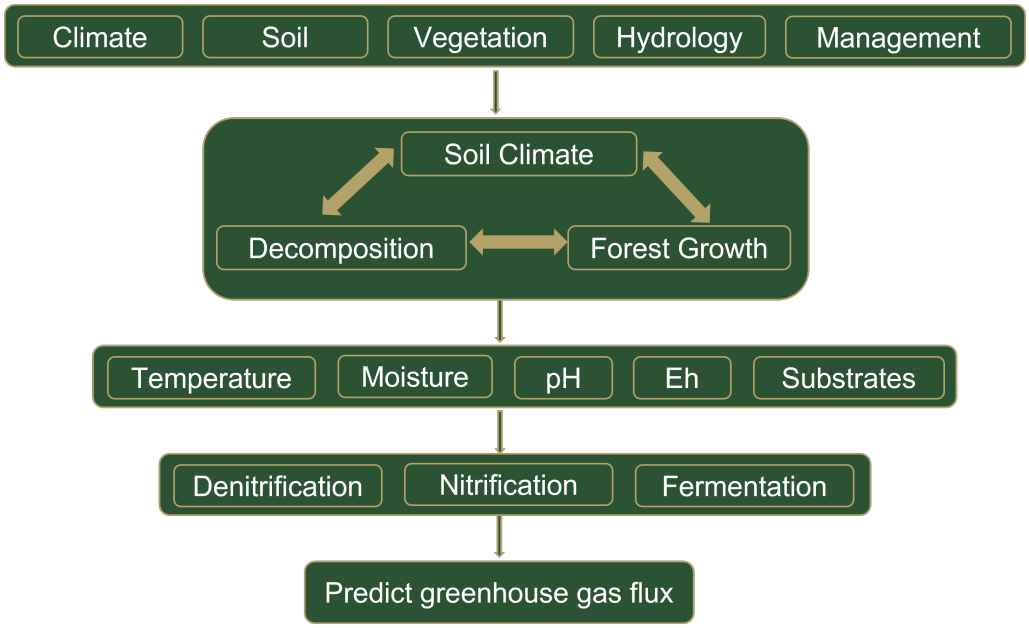

Figure 3.1: Structure of the TFW-DNDC Model

The site chosen for this study is located in the USFS Santee Experimental Forest (SEF), located in coastal S.C., USA. Previously, Dai et al. (26) analyzed spatial and temporal variations of GHGs at the watershed scale in the non-tidal areas of the SEF study area using the Forest-DNDC model and found a skewed distribution of CH_4 emissions that were heterogeneous in their spatial distribution with apparent hotspot of CH_4 emissions identified. This means that determining hotspot locations is paramount to estimating CH_4 fluxes using biogeochemical models. The same study modeled a normal distribution of CO_2 and N_2O fluxes for most years. However, the spatial distribution of N_2O fluxes became skewed during extremely wet years (e.g. 2003). Soil CO_2 flux was strongly related to soil temperature and soil moisture levels. Dai et al. (26) concluded that the watershed-scale model performed better than the field-scale model for characterizing annual CH_4 flux estimation. Also, annual CH_4 flux was positively correlated with annual precipitation while soil respiration

was substantially lower in wet years as compared to dry years. N_2O flux was more variable compared to CH_4 and CO_2 fluxes and the reason was attributed to large variations in precipitation which induced substantial variations in the inter-annual water table. In addition to water table N_2O flux is also impacted by plant N uptake and precipitation. The authors noticed that the spatial differences in the CH_4 flux was substantial on a year-to-year basis (2.5 to 7.4 MgC/ha/yr) and influenced by the water table in the watershed. In addition, wetlands were the source for CH_4 as compared to uplands with over 90% of total watershed flux originating from wetlands. As far as microtopography is concerned the authors observed that CH_4 flux was greatest where the topography was flat or depressional. Other than these locations the CH_4 flux was either zero or negative. We extend earlier field and modeling studies at the SEF through our examination of a TFFW which was not examined in(26) study.

3.2 Materials and Methods

3.2.1 Study Site

The study site is located in Santee Experimental Forest, 55 km Northwest of Charleston, South Carolina. Huger Creek is a tidal tributary of the East Branch of the Cooper River. The study site is as shown in Figure 3.2

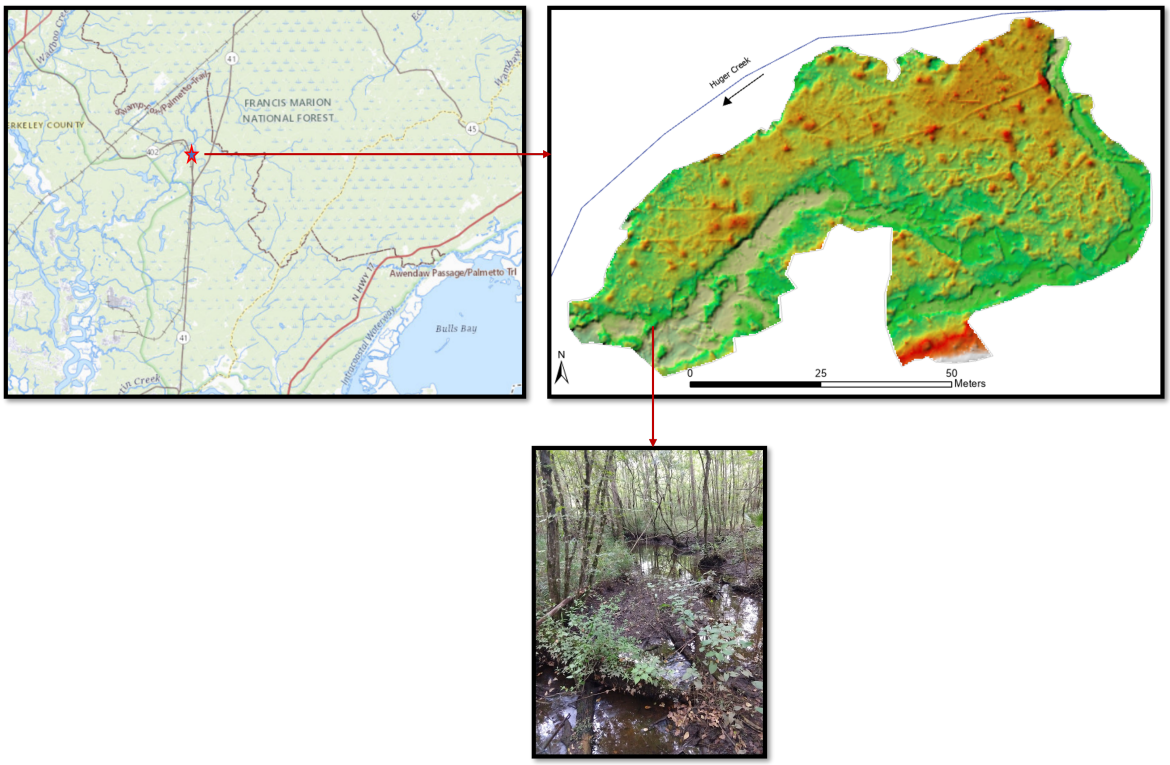

Figure 3.2: Study site at Francis Marion National Forest located at Huger Creek in Santee Experimental Forest SC USA.

The average daily tidal fluctuation at the study site is approximately 1.2m. The annual average temperature is 18.9°C and the mean annual precipitation (2019-2022) is 1,392 mm. The elevation ranges from 0.4 to 1.5 m above mean sea level (27). The soil in the floodplain is dominated by the Megget series and is characterized as deep, nearly level, and clayey (28). The soil has a low hydraulic conductivity and high water retention capacity. However, hollows in the study site are underlain with a saturated

sandy subsoil that extends to at least a meter in depth. The forest cover type consists of bottomland hardwoods which include ironwood, sweetgum, swamp dogwood, laurel oak, American elm, swamp chestnut oak, green ash, water tupelo, and Carolina ash (29). PVC groundwater wells were installed in a hollow and hummock within the riparian zone, and water table position was measured with either a Globalwater or a Druc pressure transducer logged on a 15-minute time step from January 2019 through December 2022.

3.2.2 Microtopography Classification

We collected terrestrial LiDAR data from the undisturbed study site and used available aerial LiDAR data to develop the site microtopographic model. The terrestrial LiDAR data was collected using FARO 350S Scanner, which utilizes a 1500 nm laser to produce a 3D point cloud. A total of 108 overlapping scans were taken and registered and stitched using FARO SCENE to produce a single-point cloud of the study area (Figure 3.3). The study area was scanned in February 2022 during senesced vegetation to minimize occlusion. An area of 4250 m^2 was scanned consisting of hollows, hummocks, and fringe microtopography The area was selected in a way to include the transect across the flood plain from the edge of the Huger Creek to the edge of the upland.

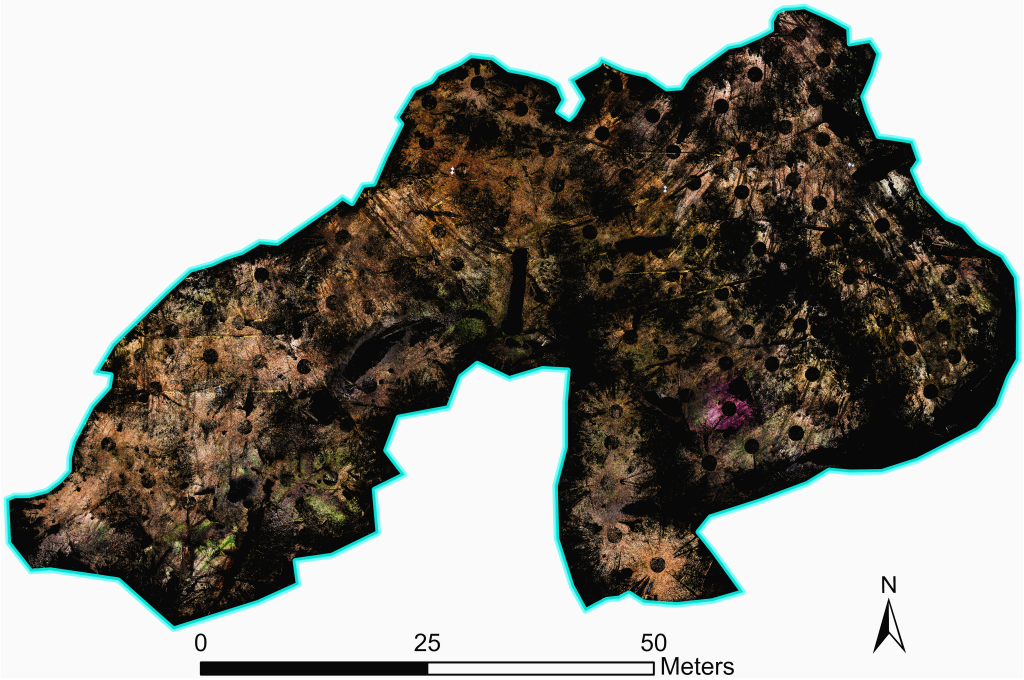

Figure 3.3: Terrestrial LiDAR-based ground point cloud of the study site. The ground points are extracted using the cloth simulation filter. A total of 108 overlapping scans were taken for the study site. The scan position is visible as black circles.

Aerial LiDAR data was collected and processed in February 2007 by Photo Science Inc and the data is owned by the Center of Forested Wetlands Research, USDA Forest Service, USA. The data can be accessed from "http://cybergis.charlotte.edu/santee/views/data-landresource/lidar-data-table.php". Two DEMs with a 1m and 0.25m resolution were created based on aerial and terrestrial LiDAR data, respectively. The microtopography was characterized by three categories: hollows (low elevation features), hummocks (high elevation features), and fringe (intermediate elevation features). Multiple studies have used water level elevation either to define microtopography or its importance in defining microtopography. Researchers such as (17), considered the 50th percentile as a threshold to characterize hollows and hummocks. We chose the mean of yearly median water levels from 2019-2022 as a threshold to categorize hollows in the terrestrial LiDAR-based DEM aligning with (16). The threshold elevation was found to be 29th percentile in elevation values for the terres-

trial LiDAR-based DEM and the same percentile was utilized to define the elevation threshold in available aerial LiDAR data. In other words, any feature up to the 29th percentile was considered as hollow. Features between the 29th and 50th percentile are considered as fringe and above the 50th percentile as hummocks (see Table 3.1) aligning with (17). Table 3.1 shows the details of the elevation distribution in both terrestrial and aerial LiDAR-based data.

Table 3.1: Microtopographic classification

Data Type	Elevation range	Hollows (29th percentile as threshold elevation)	Fringe (29th to 50th percentile)	Hummocks Above 50th percentile
TLS	0.42 to 1.2 m	0.68 m	0.68 to 1.00 m	above 1.00 m
ALS	0.49 to 2.0 m	0.87 m	0.87 to 1.20 m	above 1.20 m

The density of elevation of terrestrial and aerial LiDAR DEMs is shown in Figure 3.4.

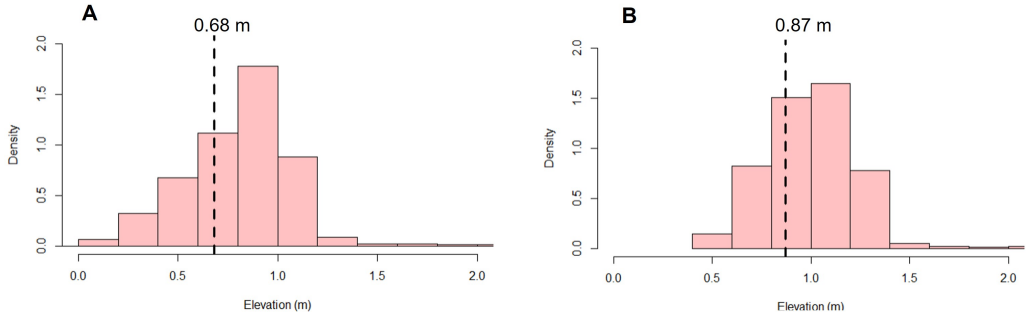

Figure 3.4: Elevation density distribution of terrestrial LiDAR-based DEM of 0.25m resolution and aerial LiDAR-based DEM of 1m resolution. A) Vertical lines show the threshold of 0.68 m which is selected based on the maximum mean water level. B) The vertical line shows the threshold of 0.87 m which is the 29th percentile of the elevation values.

3.2.3 Greenhouse Gas Modeling

We created input tables required by the TFW-DNDC model for soil, vegetation, climate data, water levels, elevation, and salinity for each of the microtopographic features. The input parameters consist of 1) soil characteristics such as the number of profile layers, pH, bulk density, clay fraction, field capacity, wilting point, and stone fraction 2) vegetation characteristics such as leaf mass, root mass, C and N stored, photosynthesis, root and wood respiration, water use efficient, growth rate, vegetation type, and age, 3) climate data which includes maximum and minimum daily temperature and daily mean precipitation, 4) daily maximum and daily minimum water levels from 2019-2022, and 5) elevation and salinity of microtopographic features. The soil layers are divided into two layers with an upper layer consisting of organic matter while a second layer is a mineral soil layer. The hummock organic layer is underlain by silty clay soils that have a low hydraulic conductivity of 0.007 cm/min and high water capacity while the hollows mineral layer is a sandy loam that is well drained with hydraulic conductivity of 1.056 cm/min. The water table depth data was measured from groundwater wells with logged pressure transducers at both the tidal and non-tidal study sites from 2019 to 2022 (see Figure 3.5). The average monthly water level is shown in Table 3.2. The model is validated with measured CH_4 and CO_2 data for 2019-2022 (Allan unpublished data) and measurements from previous studies (30) and (26). We conducted model runs utilizing both the 0.25 m and the 1m DEMs to assess the importance of the resolution of the DEM in this low-relief wetland terrain. A separate run was performed using the 0.25m resolution DEM but utilizing the water table record from the nearby non-tidal Turkey Creek watershed, a tributary of Huger Ck. That site has the same soil and vegetation cover as the tidal site but is upstream of the tidal influence.

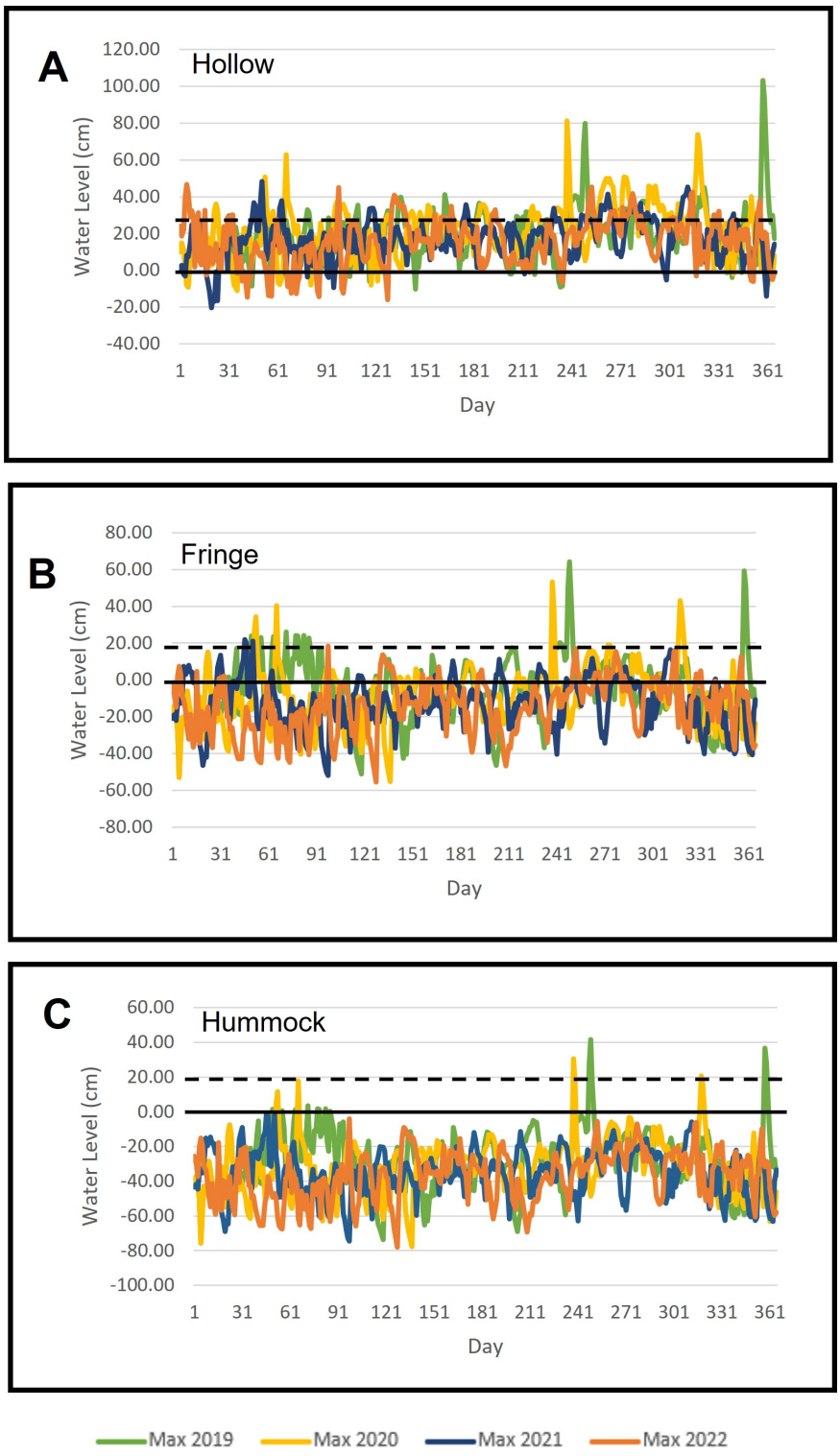

Figure 3.5: Hydrological regime of A) hollows, B) fringe, and C) hummocks at the tidal Huger Creek site from 2019 to 2022 using terrestrial LiDAR-based elevation. The figure shows the daily maximum water levels at each microtopographic feature. Here 0.00 represents the ground surface; positive values indicate the water level above the ground elevation while negative values denote the water level below the ground surface. The dashed line shows the ground surface in respect of aerial LiDAR data.

Table 3.2: Average monthly water levels (cm) in relation to the ground surface for hollows, fringe, and hummocks using terrestrial LiDAR-based 0.25 m resolution.

Water level data												
	Hollows				Fringe				Hummocks			
Month	2019	2020	2021	2022	2019	2020	2021	2022	2019	2020	2021	2022
Jan	2.6	2.7	-0.8	4.4	-25.5	-25.2	-23.5	-25.6	-47.7	-47.7	-46.5	-48.3
Feb	4.3	5.5	7.6	-4.2	-19.0	-20.5	-18.0	-32.9	-41.9	-43.0	-40.2	-55.3
Mar	3.4	5.1	2.0	-3.5	-14.6	-22.2	-26.8	-31.9	-37.3	-44.4	-49.4	-54.2
Apr	3.0	6.1	3.5	1.2	-25.5	-22.5	-29.2	-26.6	-47.6	-45.4	-51.8	-49.1
May	5.6	5.6	2.8	3.4	-24.7	-25.4	-25.5	-24.4	-47.4	-48.3	-48.1	-47.0
Jun	6.6	8.6	3.6	4.5	-20.2	-17.7	-21.6	-20.9	-42.9	-40.2	-43.9	-43.8
Jul	3.7	7.4	3.6	-1.4	-19.9	-20.7	-23.4	-29.6	-42.9	-42.9	-45.8	-51.4
Aug	3.8	12.6	4.4	0.9	-16.9	-13.9	-23.2	-25.8	-39.5	-36.7	-45.8	-48.8
Sep	11.8	13.7	9.2	10.7	-7.3	-14.7	-19.0	-15.1	-29.8	-37.8	-41.9	-38.1
Oct	9.2	16.1	8.8	7.7	-12.0	-12.4	-17.5	-16.4	-33.8	-34.2	-40.1	-38.7
Nov	10.9	14.4	8.2	5.8	-18.8	-15.2	-20.8	-18.7	-41.3	-37.9	-42.8	-41.1
Dec	11.0	1.1	2.8	2.1	-16.5	-28.9	-27.4	-22.1	-39.4	-51.1	-50.1	-44.7

3.3 Results

3.3.1 Microtopography Classification

The bare ground points from both the aerial LiDAR dataset and the terrestrial LiDAR scans were utilized to generate fine-resolution DEMs of the study area. The DEM generated from aerial LiDAR data (1m resolution) and terrestrial LiDAR Data (0.25 m resolution) is shown in Figure 3.6. The point cloud density of aerial LiDAR data is 1point/m^2 or better while the average point cloud density for terrestrial LiDAR data is 4000 pts/m^2.

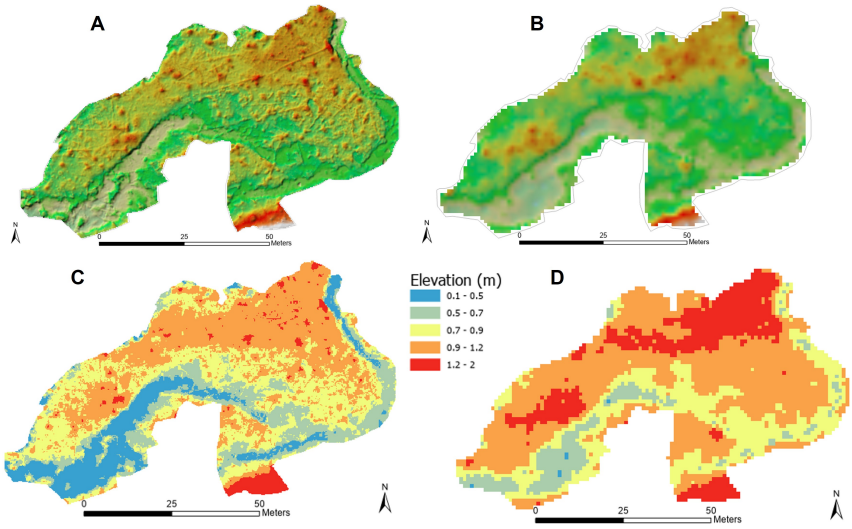

Figure 3.6: A) Shaded relief of terrestrial LiDAR-based DEM, B) shaded relief of aerial LiDAR-based DEM, C) terrestrial LiDAR-based DEM of 0.25 m resolution, and D) aerial LiDAR-based DEM of 1.00 m resolution.

A visual inspection of Figures 3.6 reveals the more pixilated nature of the coarser aerial LiDAR coverage which fails to represent many of the fine-scale microtopographic features in this low-relief terrain. The microtopographic features are delineated by combining water level data and terrestrial LiDAR elevation data as explained above. In terrestrial LiDAR data DEM hollows, fringe and hummocks occupy 28.7%, 21.6%, and 49.7% of the study area, respectively. The corresponding coverages of these same features in the aerial LiDAR data are 30.6%, 18.4%, and 51.0%, respec-

tively. The use of the coarser aerial LiDAR coverage equates to a +6.6%, -14.8% and +2.6% difference in the aerial coverage of the hollows, fringe, and hummocks in comparison to the higher resolution terrestrial LiDAR DEM (see Figure 3.7)

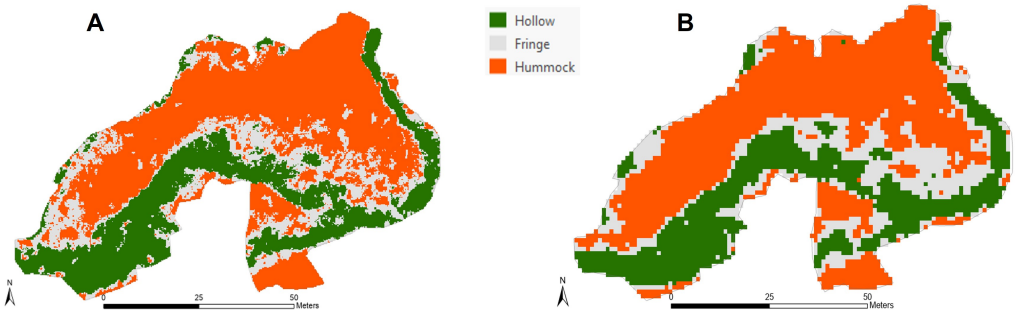

Figure 3.7: Microtopography classification based on the mean daily water level. A) Terrestrial LiDAR-based classification of microtopography B) Aerial LiDAR-based classification of microtopography in hollows, fringe, and hummocks

3.3.2 TFW-DNDC GHG Emission Model Results

The TFW-DNDC simulated CH_4 and CO_2 annual fluxes utilizing the terrestrial LiDAR DEM and the aerial LiDAR DEM for the individual landscape units are shown in Table 3.3 and Table 3.4, respectively. The same data are graphically presented in Figures 3.8 and 3.9. The annual aerially weighted composite fluxes for the study site are presented in Table 3.5.

Table 3.3: Terrestrial and aerial LiDAR data based annual CH_4 (kg C/ha/yr) emissions in Huger Creek study site.

Microtopographic feature	2019	2020	2021	2022	Mean
$Hollow_{terrestrial}$	243.7	233.9	218.4	284.3	245.1
$Fringe_{terrestrial}$	3.0	-10.1	-10.0	-10.5	-6.9
$Hummock_{terrestrial}$	-10.1	-10.1	-9.7	-10.1	-10.0
$Hollow_{aerial}$	134.7	182.1	69.5	99.5	121.5
$Fringe_{aerial}$	-10.2	-10.2	-9.8	-10.2	-10.1
$Hummock_{aerial}$	-9.9	-9.8	-9.4	-9.7	-9.7

Table 3.4: Terrestrial and aerial LiDAR data based annual soil CO_2 (Mg C/ha/yr) emissions in Huger Creek study site.

Microtopographic feature	2019	2020	2021	2022	Mean
$Hollow_{terrestrial}$	0.6	0.1	0.1	0.5	0.3
$Fringe_{terrestrial}$	2.6	2.3	2.3	2.6	2.5
$Hummock_{terrestrial}$	4.0	3.5	3.4	3.6	3.6
$Hollow_{aerial}$	1.8	0.7	0.7	0.6	0.9
$Fringe_{aerial}$	3.6	3.1	3.0	3.3	3.2
$Hummock_{aerial}$	5.4	4.5	4.3	4.5	4.7

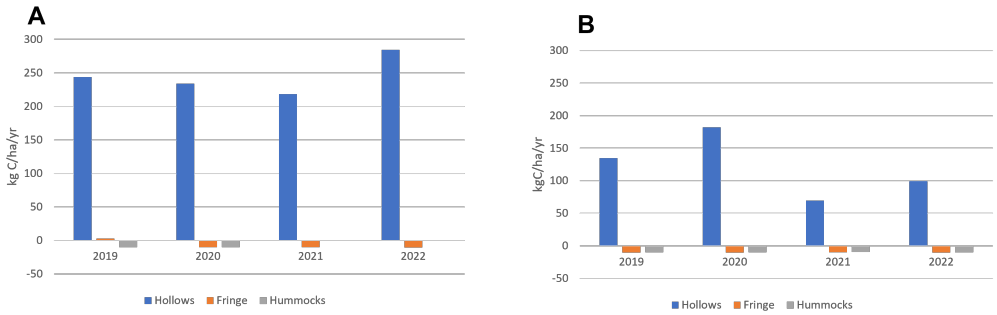

Figure 3.8: A) Simulated CH_4 emissions using terrestrial LiDAR-based data. B) Simulated CH_4 emissions using aerial LiDAR-based data

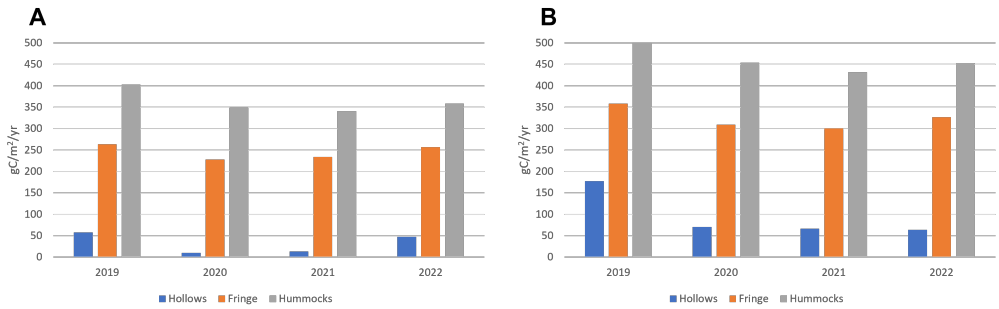

Figure 3.9: A) Simulated CO_2 emissions using terrestrial LiDAR-based data. B) Simulated CO_2 emissions using aerial LiDAR-based data

Similar to Dai et al. (26) results using the Forest DNDC model, positive CH_4 emissions were confined to areas classified as hollows with areas classified as fringe and hummocks consistently displaying net consumption. Modeled unit area CO_2 emissions for hummocks were higher than fringe which was higher than hollows for both DEM simulations. The simulations produced are significantly different unit area annual fluxes of both CH_4 and CO_2 despite each landscape unit being subject to the same water table fluctuations, precipitation inputs, and air temperatures. All other model parameters were consistent between model runs and years. This indicates that the spatial distribution and absolute elevation range selected to represent the different landscape units significantly impact the unit area fluxes of both CO_2 and CH_4. Our results show that the use of the aerial LiDAR-based DEM underestimated the CH_4 flux in 2019 (-10.1%), 2020 (-18.7%), 2021 (-73.7%), and 2022 (-68.3%) in comparison to the emissions produced by the more refined terrestrial LIDAR DEM. Absolute unit area CH_4 emission differences between the two modeled outputs were smaller for fringe and hummocks with the aerial LiDAR-based runs over predicting the strength of the CH_4 sink for these microtopographies in 2019-2022. The influence of the higher elevation ranges selected for the aerial LiDAR features (Table 3.1, Figure 3) is readily apparent where modeled unit area CO_2 emissions for all three topographic features (hollow 94.5 $\pm$55.4, fringe (323.7 $\pm$25.4), hummocks (469.2 $\pm$47.0) over the

four year study period were significantly higher for the airborne LiDAR DEM run in comparison to those generated from the terrestrial LiDAR run (Table 3.4 and Figure 3.9).

The microtopography-weighted C gas emissions for the study site are presented in Table 3.5. The study site was a net source of CH_4 emissions in all four years that were modeled irrespective of the base DEM employed in the model run. The results illustrate the importance of microtopographiclly defined hotspots. In this case, hollows, occupying approximately 30% of the study area, in determining the net CH_4 flux to the atmosphere in this low-relief coastal wetland environment. CH_4 emissions generated with the aerial LiDAR DEM averaged 70% lower and were more variable, the coefficient of variation (c.v) 11.5% terrestrial LiDAR and c.v. 39.9% for the aerial LiDAR. Again, this presumably reflects the differences in elevation thresholds between the two DEMs. As per the unit area CO_2 fluxes for the different microtopographies (Table 3.4 and Figure 3.9) the microtopographically weighted CO_2 emissions are significantly higher for hollows (average 3 times) for the aerial LiDAR model results as compared to the terrestrial LiDAR results.

Table 3.5: Modeled microtopography-weighted C gas emissions for the study site using TFW-DNDC utilizing the terrestrial and aerial LiDAR-based DEMs.

Type	Emissions	2019	2020	2021	2022
TLS_{CH4}	CH_4(kg C/ha/yr)	65.6	59.9	55.8	74.3
ALS_{CH4}		34.2	48.7	14.7	23.6
Percent $difference_{CH4}$		-10.1	-18.7	-73.7	-68.3
TLS_{CO2}	Soil CO_2(Mg C/ha/yr)	2.7	2.3	2.2	2.5
ALS_{CO2}		3.9	3.1	3.0	3.1
Percent $difference_{CO2}$		+44.4	+37.0	+32.4	+25.8

The modeled Carbon gas flux generally falls within the range reported from field-based CO_2 and CH_4 measurements previously collected from the SEF ((26; 30)), (see Table 3.6, giving some confidence to the TFW DNDC model results.

Table 3.6: Carbon emissions with respect to previous studies of Dai et al (26), Renaud (30) and Allan unpublished data

Microtopography	Carbon Flux	Renaud (30)(Values from adjacent study site in the same watershed)	Dai et al. (26) (Simulated values from adjacent non-tidal watershed)	Allan Unpublished data (Values from our tidal study site)	Simulated flux (Tidal)	Simulated flux (Non-Tidal)
Hollows	CH_4 (kg C/ha/yr)	-26.6 to 503.0	10.5 to 170.9	0 to 536.1	218.4 to 284.3	64.4 to 126.6
Fringe				-189.2 to 157.7	-10.5 to 3.0	-8.7 to 81.4
Hummocks					-10.1 to -9.7	-9.3 to -8.7
Hollows	CO_2 (Mg C/ha/yr)	Not available	2.5 to 7.4	0.8 to 6.1	0.1 to 0.6	0.3 1,78
Fringe				0.8 to 13.8	2.3 to 2.6	2.0 to 8.7
Hummocks					3.4 to 4.0	2.7 to 7.8

3.3.3 Influence of the tidally influenced water table regime

To examine the influence of the tidal hydrologic regime on GHG emissions, the Huger Ck. tidally influenced groundwater regime is substituted with the annual water table series of a tributary watershed, Turkey Creek which is upstream of the zone of tidal influence but has the same soil and vegetation cover. The annual water level fluctuations for each site and topographic feature are presented in Figure 3.10.

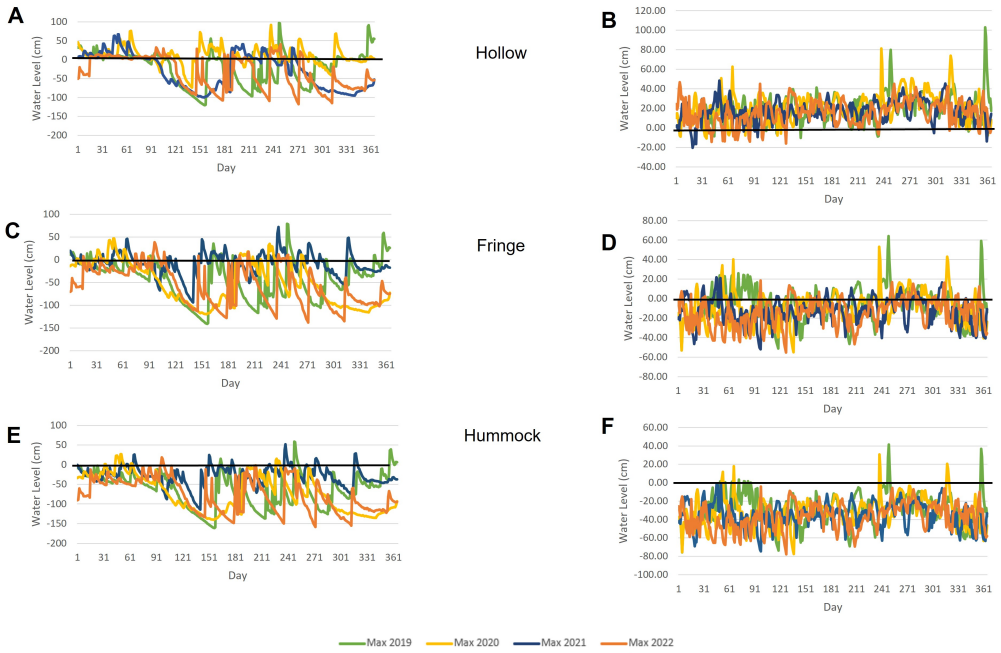

Figure 3.10: Precipitation/evapotranspiration and tidally driven water table regimes for the 2019-2022 study period. The solid black line indicates the ground level. A) Non-tidal water level at the hollows, B) Tidal water level at the hollows, C) Non-tidal water level at the fringe, D) Tidal water level at the fringe, E) Non-tidal water level at the hummocks, F) Tidal water level at the hummocks.

The carbon gas emissions modeled for each microtopography type over the four year study period using terrestrial LiDAR as the base DEM and the non-tidal and tidally influenced water levels are presented in Tables 3.7, Table 3.8, Figure 3.11 and Figure 3.12 The microtopographically weighted CH_4 and CO_2 annual fluxes for tidal and non-tidal hydrological regimes for the study site as a whole are shown in

Table 3.9.

Table 3.7: Tidal and non-tidal based annual CH_4 emissions (kg C/ha/yr) in Huger Creek study site.

Microtopographic feature	2019	2020	2021	2022	Mean
$Hollow_{tidal}$	243.7	233.9	218.4	284.3	245.1
$Fringe_{tidal}$	3.0	-10.1	-10.0	-10.5	-6.9
$Hummock_{tidal}$	-10.1	-10.1	-9.7	-10.1	-10.0
$Hollow_{non\text{-}tidal}$	113.7	126.6	64.4	77.9	95.6
$Fringe_{non\text{-}tidal}$	-8.3	81.4	64.3	-8.7	32.2
$Hummock_{non\text{-}tidal}$	-9.3	-9.2	-8.7	-9.0	-9.3

Table 3.8: Tidal and non-tidal based annual CO_2 emissions (Mg C/ha/yr) in Huger Creek study site.

Microtopographic feature	2019	2020	2021	2022	Mean
$Hollow_{tidal}$	0.6	0.1	0.1	0.5	0.3
$Fringe_{tidal}$	2.6	2.3	2.3	2.6	2.5
$Hummock_{tidal}$	4.0	3.5	3.4	3.6	3.6
$Hollow_{non\text{-}tidal}$	1.8	0.3	0.6	0.6	0.8
$Fringe_{non\text{-}tidal}$	7.1	2.0	8.7	6.2	6.0
$Hummock_{non\text{-}tidal}$	7.4	2.7	7.8	5.8	5.9

The substitution of the non-tidal water regime resulted in significantly different magnitude and spatial distribution of C gas emissions. Annual hollow CH_4 emissions declined by approximately 61% and the fringe became a net source for CH_4 in 2020 and 2021 as compared to the results for the tidal regime (Table 3.7, Figure 3.11). Annual CH_4 emissions also became significantly more variable under the non-tidal regime for the hollows (tidal c.v. 11.5% and non-tidal 30.6%) and fringe non-tidal c.v. 147.6% compared to negligible c.v. for tidal fringe. The magnitude and variability in the

CH_4 sink did not change significantly under the non-tidal water level regime. Under the non-tidal water table regime annual CO_2 emissions increased by 2.6x, 2.4x, and 1.6x for the hollow, fringe, and hummock microtopographies, respectively (Table 3.8, Figure 3.12). Annual CO_2 emissions also became more variable under the non-tidal regime for the hollows (tidal c.v. 74.2% and non-tidal 77.8%) and fringe (tidal c.v. 7.0% and non-tidal 47.8%) and hummock (tidal c.v. 7.5% and non-tidal 40.0%).

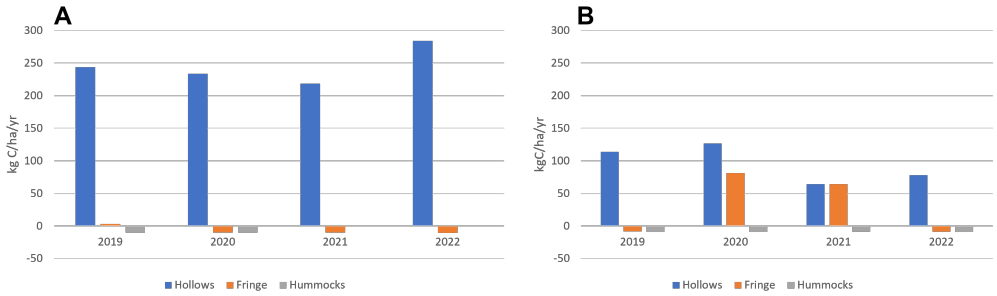

Figure 3.11: A) Simulated CH_4 emissions for tidal water levels. B) Simulated CH_4 emissions non-tidal water levels.

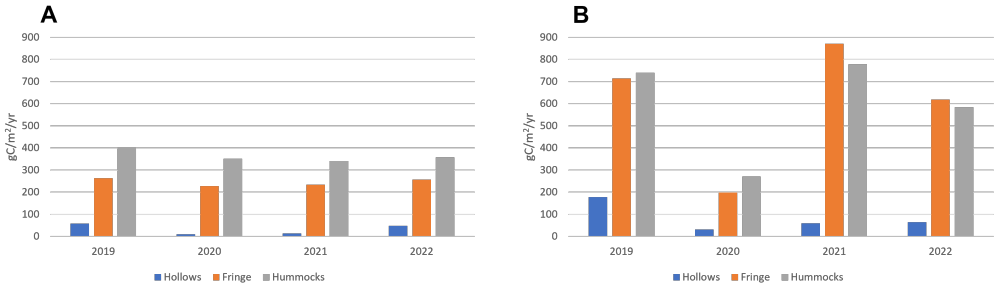

Figure 3.12: A) Simulated CO_2 emissions for tidal water levels. B) Simulated CO_2 emissions non-tidal water levels.

Table 3.9: Modeled microtopographically weighted carbon emissions under a tidal and non-tidal water table regieme for the study area.

Type	Emissions	2019	2020	2021	2022
$Tidal_{CH4}$	CH_4(kg C/ha/yr)	65.6	59.9	55.8	74.3
Non-$Tidal_{CH4}$		26.3	49.4	28.1	16.0
Percent $difference_{CH4}$		-60.0	-17.6	-49.7	-78.5
$Tidal_{CO2}$	Soil CO_2(Mg C/ha/yr)	2.7	2.3	2.2	2.5
Non-$Tidal_{CO2}$		5.7	1.9	5.9	4.4
Percent $difference_{CO2}$		+109.8	+17.7	+164.7	+79.2

The different hydrologic drivers had a clear impact on the modeled CO_2 and CH_4 emissions for the study site. The average CH_4 flux was reduced by an average of 70% and exhibited a much greater interannual variability, c.v 12.6% tidal regime, c.v. 46.8% non-tidal hydrologic regime. The substitution of a precipitation/evapotranspiration-driven hydrologic regimen had an even more significant impact on CO_2 emissions with modeled emissions exhibiting an average 1.8 times increase and the interannual variability also increasing, c.v 2.8% tidal regime, c.v. 4.2% non-tidal hydrologic regime.

3.4 Conclusion and Discussion

This study is one of the few studies that simulate GHG dynamics in a spatially explicit process-based model comparing microtopographic data obtained with terrestrial LiDAR and more widely available but coarser resolution aerial LiDAR. Due to the complexity of low-relief coastal wetlands, robust measurements of surface microtopography are required to quantify carbon stocks and fluxes. This study also quantifies the impact of microtopography and changing water levels on C gas dynamics. Similar to past studies in the SEF, our study indicates that hollows are the hotspots for CH_4 emissions Despite hollows representing only 30% of the study area, the magnitude of their emissions 70 to 284 kg/ha/yr is sufficient to turn the TFFW into a net source of CH_4, despite the majority of the TFFW surface acting as a net sink for CH_4. CO_2 emissions from hummocks were significantly higher than from hollow or fringe microtopographies and exhibited significant interannual variability (3.4 to 5.4 Mg C/ha/yr). These results show that the classification of low-relief wetland microtopography in combination with on-site measurements of the water level regime and vegetation and soil characteristics is vitally essential to assess carbon emissions accurately.

We found that the aerial LiDAR data tended to overestimate ground elevation in a densely forested wetland. In a low-relief topography where a few tens of centimeters differentiate hollows and hummocks, the overestimation of ground elevation can not only misclassify the microtopographic features but also leads to an underestimation of CH_4 flux (upto 74%) and overestimation of the CO_2 flux (upto 44%). Terrestrial LiDAR can provide accuracy in the microtopographic classification but unlike aerial LiDAR, data only covers a small area and requires a significant investment in labor and time. Our results show that combining on-site water level data and RTK GPS ground-truthed terrestrial LiDAR-based elevation data can successfully adjust the base elevation and classification of microtopographic features in aerial LiDAR data.

Our substitution of the more variable and drier non-tidal water table regime in the TFW DNDC model resulted in a significant impact on C gas emissions, with annual CH_4 emissions decreasing by an average of approximately 53% and CO_2 emissions increasing twofold over four-year study period. Prolonged periods of lower water tables (Figure 3.10) allow the diffusion of O_2 into hollow soils, significantly reducing annual CH_4 emissions, while less saturated conditions, particularly during the growing season, lead to substantially higher rates of soil respiration. The water table substitution model results give us some insight as to how GHG emissions may evolve in this low-relief bottomland wetland environment with rising sea levels as the freshwater tidal regime propagates further inland, reducing CO_2 emissions and increasing CH_4 emissions.

The C gas flux extrapolation based on these LiDAR-based DEM over larger areas, possibly at the watershed scale, may open new avenues for research and can provide insight as to how wetland microtopography interacts with precipitation/ET and tidally influenced hydrologic regimes and how these may change under rising sea levels to impact GHG emissions and carbon cycling in bottomland hardwood forests. High-resolution DEM data can assist in identifying the microtopography in the coastal region where low-relief topography and dense vegetation cover imposes a challenge in identifying hummocks and hollows. Our results show that TFW-DNDC on fine-scale topography can be assessed and accordingly, the impact of microtopography on GHG emissions can be better understood.

3.5 References

[1] N. Cavallaro, G. Shrestha, R. Birdsey, M. A. Mayes, R. G. Najjar, S. C. Reed, R.-L. P, and Z. Z., "Second state of the carbon cycle report (SOCCR2): A sustained assessment report," tech. rep., 2018.

[2] B. Zhang, H. Tian, C. Lu, G. Chen, S. Pan, C. Anderson, and B. Poulter, "Methane emissions from global wetlands: An assessment of the uncertainty associated with various wetland extent data sets," *Atmos. Environ.*, vol. 165, pp. 310–321, Sept. 2017.

[3] W. J. Mitsch, B. Bernal, A. M. Nahlik, Ü. Mander, L. Zhang, C. J. Anderson, S. E. Jørgensen, and H. Brix, "Wetlands, carbon, and climate change," *Landsc. Ecol.*, vol. 28, pp. 583–597, Apr. 2013.

[4] C.-T. A. Chen, T.-H. Huang, Y.-C. Chen, Y. Bai, X. He, and Y. Kang, "Air–sea exchanges of CO^2 in the world's coastal seas," *Biogeosciences*, vol. 10, pp. 6509–6544, Oct. 2013.

[5] T. E. Dahl, *Status and Trends of Wetlands in the Conterminous United States 1998 to 2004*. U.S. Department of the Interior, U.S. Fish and Wildlife Service, 2005.

[6] S. M. Stedman and T. E. Dahl, "Status and trends of wetlands in the coastal watersheds of the eastern united states, 1998 to 2004," tech. rep., National Oceanic and Atmospheric Administration, National Marine Fisheries Service and U.S. Department of the Interior, Fish and Wildlife Service.

[7] A. Barendregt and C. Swarth, "Tidal freshwater wetlands: Variation and changes," *Estuaries Coasts*, vol. 36, no. 3, pp. 445–456, 2013.

[8] C. B. Craft, "Tidal freshwater forest accretion does not keep pace with sea level rise," *Glob. Chang. Biol.*, vol. 18, pp. 3615–3623, Dec. 2012.

[9] S. C. Neubauer and C. B. Craft, "Global change and tidal freshwater wetlands: scenarios and impacts," *Tidal freshwater wetlands*, pp. 253–266, 2009.

[10] S. C. Neubauer, M. F. Piehler, A. R. Smyth, and R. B. Franklin, "Saltwater intrusion modifies microbial community structure and decreases denitrification in tidal freshwater marshes," *Ecosystems*, vol. 22, pp. 912–928, June 2019.

[11] K. W. Krauss, G. B. Noe, J. A. Duberstein, W. H. Conner, C. L. Stagg, N. Cormier, M. C. Jones, C. E. Bernhardt, B. Graeme Lockaby, A. S. From, T. W. Doyle, R. H. Day, S. H. Ensign, K. N. Pierfelice, C. R. Hupp, A. T. Chow, and J. L. Whitbeck, "The role of the upper tidal estuary in wetland blue carbon storage and flux," *Global Biogeochem. Cycles*, vol. 32, pp. 817–839, May 2018.

[12] J. Bubier, A. Costello, T. R. Moore, N. T. Roulet, and K. Savage, "Microtopography and methane flux in boreal peatlands, northern Ontario, Canada," *Can. J. Bot.*, vol. 71, pp. 1056–1063, Aug. 1993.

[13] T. R. Moore, A. De Young, J. L. Bubier, E. R. Humphreys, P. M. Lafleur, and N. T. Roulet, "A Multi-Year record of methane flux at the mer bleue bog, southern canada," *Ecosystems*, vol. 14, p. 646, Apr. 2011.

[14] T. R. Moore and R. Knowles, "The influence of water table levels on methane and carbon dioxide emissions from peatland soils," *Can. J. Soil Sci.*, vol. 69, pp. 33–38, Feb. 1989.

[15] C. Li, J. Cui, G. Sun, and C. Trettin, "Modeling impacts of management on carbon sequestration and trace gas emissions in forested wetland ecosystems," *Environ. Manage.*, vol. 33, July 2004.

[16] J. D. Graham, D. M. Ricciuto, N. F. Glenn, and P. J. Hanson, "Incorporating microtopography in a land surface model and quantifying the effect on the carbon cycle," *J. Adv. Model. Earth Syst.*, vol. 14, Feb. 2022.

[17] A. E. L. Stovall, J. S. Diamond, R. A. Slesak, D. L. McLaughlin, and H. Shugart, "Quantifying wetland microtopography with terrestrial laser scanning," *Remote Sens. Environ.*, vol. 232, p. 111271, 2019.

[18] M. Villoslada, L. Sipelgas, T. F. Bergamo, R. D. Ward, E. Reintam, A. Astover, T. Kumpula, and K. Sepp, "Multi-source remote sensing data reveals complex topsoil organic carbon dynamics in coastal wetlands," *Ecol. Indic.*, vol. 143, p. 109329, Oct. 2022.

[19] H. Wang, Z. Dai, C. C. Trettin, K. W. Krauss, G. B. Noe, A. J. Burton, C. L. Stagg, and E. J. Ward, "Modeling impacts of drought-induced salinity intrusion on carbon dynamics in tidal freshwater forested wetlands," *Ecol. Appl.*, vol. 32, p. e2700, Dec. 2022.

[20] Z. Dai, C. C. Trettin, S. Frolking, and R. A. Birdsey, "Mangrove carbon assessment tool: Model development and sensitivity analysis," *Estuar. Coast. Shelf Sci.*, vol. 208, pp. 23–35, Aug. 2018.

[21] C. Li, J. Aber, F. Stange, K. Butterbach-Bahl, and H. Papen, "A process-oriented model of N_2O and NO emissions from forest soils: 1. model development," *J. Geophys. Res.*, vol. 105, pp. 4369–4384, Feb. 2000.

[22] C. Li, C. Trettin, G. Sun, S. McNulty, and K. Butterbach-Bahl, "Modeling carbon and nitrogen biogeochemistry in forest ecosystems," *In: 3rd International Nitrogen Conference: 893-898*, 2005.

[23] Y. Shu, G. Chuying, H. Jiayin, Z. Leiming, D. Guanhua, W. Xuefa, and Y. Guirui, "Modelling soil greenhouse gas fluxes from a Broad-Leaved korean

pine forest in changbai mountain: Forest-DNDC model validation," *jore*, vol. 10, pp. 127–136, Apr. 2019.

[24] Z. Dai, R. A. Birdsey, and A. J. Dugan, "Estimated carbon sequestration in a temperate forest in idaho of USA," *Nat. Sci. (Irvine)*, vol. 09, pp. 421–436, Dec. 2017.

[25] J. Kurbatova, C. Li, A. Varlagin, X. Xiao, and N. Vygodskaya, "Modeling carbon dynamics in two adjacent spruce forests with different soil conditions in Russia," *Biogeosciences*, vol. 5, no. 4, pp. 969–980, 2008.

[26] Z. Dai, C. C. Trettin, C. Li, H. Li, G. Sun, and D. M. Amatya, "Effect of assessment scale on spatial and temporal variations in CH_4, CO_2, and N_2O fluxes in a forested wetland," *Water Air Soil Pollut.*, vol. 223, pp. 253–265, Jan. 2012.

[27] C. Trettin, B. J. Czwartacki, C. J. Allan, and D. M. Amatya, "Linking freshwater tidal hydrology to carbon cycling in bottomland hardwood wetlands," *In: Stringer, Christina E.;K.W. Krauss; J.S. Latimer, eds. 2016. Headwaters to estuaries: advances in watershed science and management -Proceedings of the Fifth Interagency Conference on Research in the Watersheds. March 2-5, 2015, North Charleston, South Carolina. e-General Technical Report SRS-211. Asheville, NC: U.S. Department of Agriculture Forest Service, Southern Research Station.*, 2016.

[28] B. M. Long, "Soil survey of berkeley county, South Carolina," 1980.

[29] B. J. Czwartacki, "Time and tide: understanding the water dynamics in a tidal freshwater forested wetland," Master's thesis, College of Charleston, 2013.

[30] L. Renaud, "Methane emissions from bottomland hardwood wetlands in francis marion national forest, SC," Master's thesis, College of Charleston, United States, 2008.

CHAPTER 4: Overall Conclusion

This research provides a systematic data-driven framework to guide the study of microtopography using close-range remote sensing. We recommend including terrain attributes derived from high-resolution DEM data (less than $1m^2$) for the microtopographic studies. Using fine-scale resolution data leads to big data challenges that can be handled by utilizing HPC and cloud computing resources. We also emphasize the need to model microtopographic features better to investigate their impact on ecosystem processes by including field-based observations in the models (i.e., model calibration and validation).

This research also provides a method to delineate microtopographic features in a low-relief forested terrain by combining mean daily maximum water levels and highly accurate elevations measured from terrestrial LiDAR and RTK GPS. An elevation threshold percentile was determined based on the mean daily maximum water level and used to characterize microtopographic features into hollows, fringe, and hummocks. The selected elevation percentiles were then used in a coarser resolution aerial LiDAR-based DEM to delineate microtopography over a comparatively more extensive area. This method reduces the need for labor-intensive field surveys over a large area.

We also discussed the role of microtopography in Carbon dynamics and displayed the importance of the characterization of microtopography. Our results indicate that even though hollows occupied 30% of the study area, they accounted for significant carbon emissions. These results show that classifying low-relief wetland microtopography in combination with on-site measurements of the water level regime and vegetation and soil characteristics is important to accurately assess carbon emissions.

In addition, hydro periodicity also impacted the emissions in the microtopographic features by increasing CH_4 emissions under saturated conditions and producing higher rates of respiration when microtopography is exposed to air in the growing season.

Another important highlight of this research is to highlight the importance of the water table position on GHG emissions. The water table substitution model results clearly indicated lower CH_4 emissions and higher soil respiration in non-tidal wetlands. This bolsters our belief that with rising sea levels as the freshwater tidal regime propagates further inland, reduced CO_2 emissions and increasing CH_4 emissions conditions may arise. The results also show that incorporating fine-scale microtopography into the spatially explicit TFW-DNDC model structure can identify the importance of hotspots in determining annual GHG emissions in low-relief coastal watersheds.

TFW-DNDC considers daily maximum and minimum water levels, as compared to other DNDC models that only consider one daily water level value but the model can further be improved by incorporating more dynamic water levels inherent in daily tidal cycles. In addition, the model can only be accessed by contacting the Center for Forest Watershed Research in USDA Forest Service. The accessibility can be improved by either making it open-source or providing a link to US Forest Service website, that way multiple researchers can be benefitted from the capabilities of the model. There is also a need for a user-friendly user manual that can provide a step-by-step guide to using the TFW DNDC model.